Dissertation

submitted to the
Combined Faculties for the Natural Sciences and for Mathematics
of the Ruperto-Carola University of Heidelberg, Germany
for the degree of
Doctor of Natural Sciences

Put forward by
Rabea Helene Link
born in Bietigheim-Bissingen
Oral examination: 26.10.2023

Modeling 3D Cell Shape in Structured Environments with the Cellular Potts Model

Referees: Prof. Dr. Ulrich Schwarz

Prof. Dr. Fred Hamprecht

In this work, we explore the 3D shape of cells and organoids in structured environments. Understanding the physical determinants of cell shape regulation in structured environments is vital as it plays a crucial role in essential biological processes, including migration, division and tissue development. The cellular Potts model (CPM) has emerged as a powerful computational framework for simulating cell behavior and morphodynamics in complex biological systems. Our research focuses on utilizing the CPM to model 3D single cells on 2D micropatterns and in 3D structured environments. We explicitly consider intracellular structures such as the nucleus and stress fibers and model their impact on cell shape. This allows us to predict morphology and trajectories during the single cell spreading process on micropatterns and demonstrates the effect of nucleus and stress fibers on these processes. Through systematic simulations and comparison with surface minimization approaches and experimental data, we demonstrate the ability of our model to accurately predict cell shapes under different spatial constraints. Additionally, we model the optic cup evagination in fish retina organoids with explicit representation of Matrigel at the surface of the organoid. The findings shed light on the mechanistic basis underlying the shape changes observed in multicellular systems.

In dieser Arbeit untersuchen wir die 3D-Form von Zellen und Organoiden in strukturierten Umgebungen. Das Verständnis der physikalischen Faktoren für die Regulierung der Zellform in strukturierten Umgebungen ist von grundlegender Bedeutung, da diese eine entscheidende Rolle bei wesentlichen biologischen Prozessen wie Migration, Teilung und Gewebeentwicklung spielt. Das CPM hat sich als leistungsfähiges Modell für die Simulation von Zellverhalten und Morphodynamik in komplexen biologischen Systemen erwiesen. Unsere Forschung konzentriert sich auf die Nutzung des CPM zur 3D Modellierung einzelner Zellen auf 2D-Mikropattern und in strukturierten 3D-Umgebungen. Wir berücksichtigen explizit intrazelluläre Strukturen wie den Zellkern und Stressfasern und modellieren deren Einfluss auf die Zellform. Auf diese Weise können wir die Morphologie und die Trajektorien während des Ausbreitungsprozesses einzelner Zellen auf Mikropattern vorhersagen und den Einfluss von Zellkern und Stressfasern auf diese Prozesse nachweisen. Durch systematische Simulationen und Vergleiche mit Modellen, die Oberflächenminimierung nutzen, zeigen wir im Vergleich mit experimentellen Daten, dass unser Modell in der Lage ist, Zellformen unter verschiedenen räumlichen Bedingungen genau vorherzusagen. Zusätzlich modellieren wir die Evagination von Retinazellen in Fischorganoiden mit expliziter Darstellung von Matrigel an der Oberfläche des Organoids. Die Ergebnisse bieten eine Erklärung auf Grundlage von Interaktionsenergien für die beobachtete Formveränderung des multizellulären Systems.

Contents

1 Introduction

Over the past two decades, the important role of mechanobiology in determining cell fate and behavior has been increasingly recognized [1–3]. The realization that not only biochemical cues, but also the local microenvironment and mechanical forces exerted on cells impact cell shape, function, decision making and even gene expression has revolutionized our understanding of cellular processes. Cell shape in particular is intricately regulated by the cell through a combination of extracellular and intracellular processes and can be easily observed, making it a subject of great interest and investigation [4].

Cell shape diversity is a remarkable characteristic observed across different cell types, and is often optimized for a specific function. Examples are neurons with extending dendrites and axons optimized for fast transfer of electrical impulses or red blood cells optimized to deliver oxygen when squeezing through thin blood vessels. Even within a single cell type, a wide array of shapes can be found [5]. Variations in cell morphology can have significant implications for division [6], differentiation [7], and tissue morphogenesis [8, 9]. Understanding the underlying mechanisms that govern cell shape is vital for unraveling the complexities of cellular functions and tissue organization.

To gain deeper insights into the intricate interplay of the molecular and biophysical processes responsible for force sensing and exertion and the consequential cell shape changes, numerous experiments have designed and conducted [10]. These experiments have led to valuable data on the cytoskeletal dynamics [11, 12], in particular actin force generation [13], and adhesion molecules [14, 15] that contribute to shaping cells. However, the sheer complexity of cellular systems often calls for the integration of experimental findings with computational modeling approaches to comprehend emergent properties arising from local interactions.

One such powerful modeling tool for the study of cell shape is the cellular Potts model (CPM) [16]. The CPM is a versatile computational framework that employs pseudo-energies and a modified Metropolis algorithm to simulate the evolution of a system towards a local minimum. It has proven to be particularly useful in capturing the collective behavior of cells [17, 18] and their interactions in tissues [19, 20]. By considering the influence of cell adhesion and mechanical forces, the CPM can

effectively recapitulate the dynamics and morphological changes observed in various cellular systems [21–24].

Modeling and predicting cell shape dynamics and comparison with experimental data deepens our understanding of the intricate processes governing cell shape. In this study, we explore the complexities of cell shape dynamics with the CPM. Through this approach, we uncover new insights into the adaptive and context-dependent nature of cell shape and its impact on cellular behavior, ultimately contributing to a deeper understanding of mechanobiology.

Outline

In **Chapter 2**, we describe the mechanobiology of cells, and focus on the intracellular structures that are important for cell morphology. We introduce the cytoskeleton, and focus specifically on the actin cortex and stress fibers. Additionally, we describe the effect of the nucleus and focal adhesions on cell shape. Then, we describe biological processes for which the cell shape is relevant, such as migration, differentiation and division.

In **Chapter 3**, we give an overview of experiments with cells in structured environments. We focus on structured environments in two and three dimensions and describe their effect on cell shape and behavior. We differentiate between single cell experiments and experiments with cell collectives, where we highlight the emerging properties due to cell-cell interactions. Lastly, we give an overview of organoid development in structured environment experiments, which is an exciting new research direction that enables investigations of mechanical input during morphogenesis in a controlled environment.

In **Chapter 4**, we outline how models have been used to describe and predict the previously described experimental results. We given an overview of the most successful 2D and 3D single cell models that predict cell shape and describe how these models can be modified for cell collectives and organoids. Then, we focus on the CPM, a lattice based modeling framework used to describe single cells and collectives. We describe the origin and mechanism of the CPM, as well as how to implement the intracellular structures in the Hamiltonian used to describe the biological system. Finally, we explain the CompuCell3D (CC3D) software architecture and custom plugins used in this work.

In **Chapter 5**, we detail our approach to model 3D cell shape on 2D micropatterned surfaces with the CPM. We discuss the influence of the nucleus on cell shape, predict trajectories of cells spreading on micropatterns and compare predicted

cell shapes during spreading to experimental results. Finally, we discuss advantages and challenges when including stress fibers in single cell CPM simulations by compartmentalizing the cell.

In **Chapter 6**, we model cell shape in 3D structured environments and compare the shapes we obtain experimentally, from surface minimization and with the CPM. To quantitatively compare shapes, we employ a spherical harmonics analysis and use this method to test a large parameter range in the CPM simulations as well as to quantify the influence of the nucleus on the cell shapes.

In **Chapter 7**, we model organoids in an extracellular matrix (ECM) protein environment with the CPM. We predict the influence of ECM proteins on the morphogenesis of retina organoids and reproduce the experimentally observed organoid shapes with optic vesicle regions on their surface for small organoids and a neuroepithelial layer at the surface for large organoids.

In **Chapter 8**, we summarize and discuss the main findings of this work and give an outlook to possible future directions.

2 Intracellular structures governing cell shape

The shape of animal cells is the result of active and passive intracellular and extracellular forces arising from actin polymerization, actomyosin contraction, cell adhesion, and material properties of the cell and its mechanical environment [4]. In this chapter, we give an overview of intracellular structures that are relevant for cell shape, which are depicted schematically in Fig. 2.1.

2.1 Introduction to cell mechanics

The cell membrane, a lipid bilayer with fluid-like properties, acts as the physical boundary of the cell, but does not contribute much to the mechanics of cells for most cell types [25].

Instead, the cytoskeleton, a remarkable and intricate network of protein filaments, is responsible for the structural integrity, shape and mechanical properties of eukaryotic cells. Acting as a dynamic scaffold, the cytoskeleton plays a crucial role in diverse cellular processes, including cell division, intracellular transport, cell signaling, and cell migration. Composed of three major types of filaments - actin microfilaments, intermediate filaments, and microtubules - the cytoskeleton provides the necessary framework for the organization and movement of cellular components, contributing to the overall functionality of the cell [11].

2.1.1 Actin microfilaments

Action microfilaments are the thinnest components of the cytoskeleton, consisting of two intertwined strands of actin protein subunits. These filaments are highly versatile and dynamic, actively participating in numerous cellular activities. They form the basis of contractile structures in muscle cells as well as in all other cell types. Additionally, actin plays a pivotal role in cell shape maintenance and support, facilitating cell movement and membrane protrusions like filopodia and lamellipodia during cell migration [13].

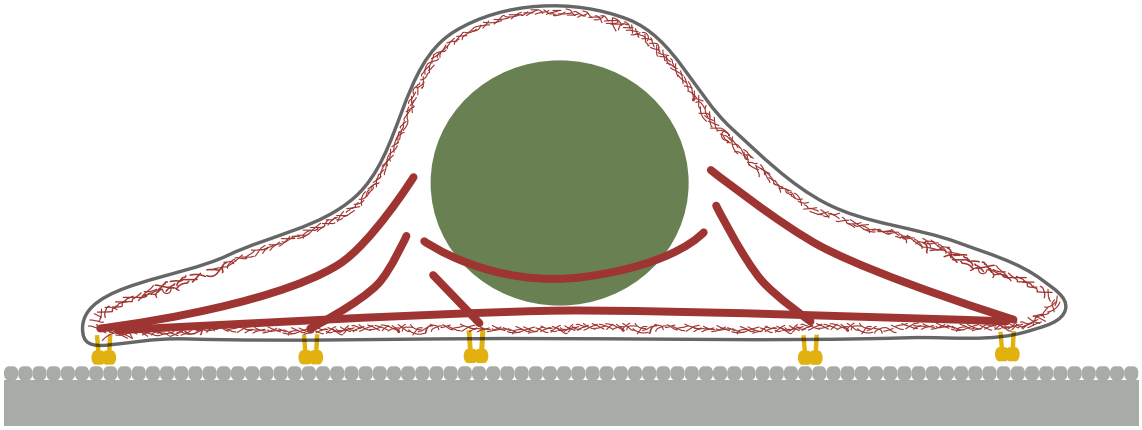

Figure 2.1: **Schematics of a single cell on an adhesive substrate**, not to scale. The substrate is coated with the ECM protein fibronectin (gray), which enables a connection between the cell and the substrate through focal adhesions (yellow). On the inner face of the cell plasma membrane (black) is the actin cortex (red), a 100-1000 nm thick layer of F-actin filaments, motor proteins and other actin binding proteins that give mechanical rigidity to the cell surface. Stress fibers (red, thick) are bundles of 10-30 actin filaments that can form at focal adhesions that are used by cells to sense forces in their local microenvironment. The nucleus (green) is a spherical or ovoid organelle that influences the shape of cells adhered to a substrate due to its high stiffness.

Most cell types have a thin layer of actin filaments located beneath the cell plasma membrane, see Fig. 2.1. This network is called actin cortex and serves as a critical determinant of cell shape [26]. It consists of filamentous actin and regulating proteins such as Arp2/3 as a nucleator and α-actinin and filamin as crosslinkers. Myosin-II motors assemble to minifilaments and contract the actin network. It provides mechanical support and helps maintain cell integrity by generating contractile forces and resisting external mechanical stresses [27, 28]. The actin cortex is mechanically rigid and at the same time plastic, due to the high turnover in the network. Research on the actin cortex has demonstrated its dynamic nature, with continuous remodeling on timescales of 10s of seconds. Rounded cells have an isotropic filament network, while the actin fibers in spread-out cells form anisotropic bundles. High network tensions lead to a local reduction of surface area. Tension gradients are an important mechanism for cell deformations and migration [29–31].

The mechanical properties of the cortex depend on both the myosin motor activity and the architecture of the actin network. The cortex is present in most cell types, but not necessarily isotropic. An isotropic actin cortex is assumed in the 2D contour model for single cells on micropatterned structures, see Chapter 3.1.2, where it is modeled as a constant surface tension in the cell. In the context of the CPM, the

effect of the actin cortex is modeled via area constraints and interaction energies of neighboring voxels, reducing the energy of the system if the cell becomes more spherical . Wortel and colleagues [32] model the effect of the contracting actin cortex during migration with a negative energy contribution, which favors voxel copying attempts in regions where voxels were added recently.

In addition to the cortex network, stress fibers, which are aligned bundles of 10-30 actin filaments, are assembled by cells in areas of high stresses, see Fig. 2.1. They are crosslinked with proteins such as α-actinin, fascin and filamin. Myosin-II-motor proteins are present in most stress fibers, making them contractile. Stress fibers can couple directly to the ECM via focal adhesions, that contain proteins that are binding to actin filaments. Stress fibers are under isometric tension and are relevant for cell adhesion, migration and mechanosensing on the mesoscale, as they sense and mediate forces in their local microenvironment. Stress fibers are typically classified in three types, that differ in both function and composition. Dorsal stress fibers do not contain myosin and originate from a focal adhesion at the leading edge of migrating cells. Often, they couple to transverse arcs, which are contractile (myosin-containing) stress fibers that form parallel to the leading edge of the cell. Ventral stress fibers are contractile as well, but they are attached to focal adhesions on both ends [33, 34].

In structured environments, stress fibers typically form between points of adhesion in regions with high stress [34]. The stress fiber distribution after cell spreading can be described independently of the spreading mechanism by adding straight lines between points of adhesion when the line is completely within the cell body [35].

2.1.2 Other cytoskeletal proteins

Microtubules are the largest and most rigid components of the cytoskeleton. They are composed of tubulin protein subunits arranged in a hollow tube-like structure. Microtubules serve as crucial tracks for intracellular transport, guiding motor proteins that carry vesicles, organelles, and other cellular cargo. They also play an important role during cell division by forming the mitotic spindle, which ensures the accurate segregation of chromosomes into daughter cells. Additionally, microtubules are involved in maintaining cell shape, supporting cilia and flagella, and influencing cell polarity and intracellular signaling [36, 37].

Intermediate filaments are a diverse group of cytoskeletal components that provide mechanical strength and stability to cells. Unlike microfilaments and microtubules, intermediate filaments do not exhibit dynamic polymerization and depolymerization. Instead, they form stable networks that reinforce the structural integrity of cells, especially in tissues subjected to mechanical stress. Different types of intermediate

filaments are found in various cell types, such as keratins in epithelial cells, vimentin in mesenchymal cells, and neurofilaments in nerve cells [36, 38].

One of the most fascinating aspects of the cytoskeleton is its dynamic nature. All three types of cytoskeletal filaments are subject to constant assembly and disassembly, a process essential for cellular responses to changing conditions. This dynamic regulation is achieved through a range of proteins, such as actin-binding proteins, microtubule-associated proteins, and intermediate filament-associated proteins, which modulate the polymerization, stability, and interactions of cytoskeletal filaments [12].

2.1.3 Nucleus

The nucleus harbors the genomic material and additionally contributes to cellular mechanics. As the largest organelle in most eukaryotic cells, with diameters of up to 20 µm, it influences the shape of cells due to its size and stiffness, see Fig. 2.1. In relaxed cells, the nucleus is spherical or ovoid, and has an elastic modulus of 1-10 kPa, which is 5-10 times stiffer than the cytoplasm in differentiated cells [39]. Even though the nucleus is much stiffer than the cytoplasm, it can be deformed by cells, for example when they migrate through constrictions [39]. For stationary cells on 2D micropatterns, the nucleus is typically positioned at the center of the inner area, and extends to the third dimension, while the cytoplasm is relatively flat (fried-egg shape) [36]. At the same time, there has been evidence of a direct coupling between the nucleus and the cytoskeleton since 1997, leading to the speculation that the nucleus is actively involved in cell mechanical processes [40]. Much later, the LINC complexes (Linker of Nucleoskeleton and Cytoskeleton) were identified as modulators of the mechanical signal transmission between the cytoskeleton and the nuclear envelope proteins [41]. Additionally, mechanosensitive transcription factors, the most investigated being yes-associated protein 1 (YAP), were found to localize in the nucleus in cells under tension due to changes in the nuclear pore complexes [42].

The position of the nucleus during cell migration is typically at the rear of the cell, and for cells on micropatterned surfaces the nucleus takes a position close to the center of mass of the cell [43].

2.1.4 Focal adhesions

Focal adhesions connect the cell to the ECM, a fibrous network of collagen, fibronectin, and other proteins, thus they are important for cell migration and environmental sensing, see Fig. 2.1. Focal adhesions are protein complexes which are 1-5 µm long and 300-500 nm wide, depending on the intra- and extracellular local microenvironment.

The binding to the ECM is realized through integrin transmembrane receptors. On the inside of the cell, a nanostructure consisting of an integrin signalling layer, a force transduction layer and the actin-regolatory layer binds the focal adhesion to actin stress fibers [36]. The composition of focal adhesion depends on many factors, such as the stiffness and composition of the ECM. Focal adhesions on stiff glass substrates are larger and more numerous as compared to substrates with stiffnesses similar to the human body (1-100kPa). The average lifetime of focal adhesions is about one hour, depending on intra-and extracellular factors [15, 36, 44].

2.2 The importance of cell shape for biological processes

Cell shape is not just a mere structural aspect but is intimately tied to the cellular functions and behaviors that dictate the overall health and functionality of organisms [45]. Understanding the factors that regulate cell shape is crucial for advancing our knowledge of developmental processes, tissue homeostasis, and disease mechanisms.

Cell shape is intimately tied to the specific functions and roles individual cells perform within the complex web of life. Different cell types have evolved distinct shapes that are uniquely suited to their specialized tasks. For instance, neurons, with their long, branching extensions (dendrites and axons), enable the transmission of electrical signals over considerable distances, facilitating communication within the nervous system [46]. Conversely, red blood cells have a biconcave disc shape, which optimizes their surface area, allowing for efficient exchange as they transport oxygen throughout the body [47]. Furthermore, the tightly packed, cobblestone-like arrangement of epithelial cells forms protective barriers and linings in various tissues and organs, acting as a front-line defense against external threats [48]. This remarkable correlation between cell shape and function highlights the precision of cellular design and the adaptation of cells to perform their crucial roles in sustaining life.

Cell shape's dynamic nature is intimately connected to cell movement, a fundamental process with broad implications in biology. The cytoskeleton, a complex network of protein filaments, serves as the structural framework for maintaining cell shape and also plays a pivotal role in facilitating cellular motility. As cells migrate, they undergo coordinated changes in shape, driven by the dynamic rearrangement of actin filaments, microtubules, and intermediate filaments [49]. These rearrangements allow cells to change their morphology, extend protrusions like lamellipodia and filopodia, and form adhesions with the substrate for traction. Cell movement is

central to critical physiological processes, such as embryonic development, immune responses, and wound healing. Moreover, aberrant cell migration is associated with pathological conditions, including metastatic cancer cell invasion and tissue fibrosis [36]. Understanding the intricate interplay between cell shape and motility is vital in deciphering the complexities of cellular behavior and holds promise for potential therapeutic interventions targeting cell migration-related diseases.

Accurate cell shape is essential during cell division, ensuring the faithful transmission of genetic material to daughter cells. The process of cell division, also known as mitosis, relies heavily on the cytoskeleton's coordination and organization. Microtubules, a major component of the cytoskeleton, form the mitotic spindle, a specialized structure that segregates duplicated chromosomes during cell division. The spindle fibers exert forces that precisely separate the genetic material into two daughter cells [36]. Any disruptions or abnormalities in cell shape can lead to errors in chromosome distribution, resulting in genetic instability and potential cell death. Proper cell shape and cytoskeletal function are crucial for maintaining genomic integrity and ensuring the accurate transmission of genetic information, which is vital for tissue growth, repair, and development in multicellular organisms [45].

Cell shape not only influences cellular behavior but also determines how cells respond to their external environment [10, 45]. The interactions between cells and their surroundings play a crucial role in various physiological processes. Cell shape can dictate how efficiently cells interact with neighboring cells, ECM, or foreign particles.

Additionally, cell shape can be influenced by the mechanical properties of the extracellular environment, such as its stiffness. Numerous studies have shown that changes in the mechanical properties of the extracellular microenvironment can impact cell shape [50–52], migration [53–55], and differentiation [8, 56]. Understanding the complex relationship between cell shape and the extracellular environment is essential for unraveling the intricate mechanisms underlying tissue development, wound healing, and immune responses.

Moreover, the extracellular environment's mechanical properties, such as its stiffness or rigidity, can have profound effects on cell shape and behavior. Cells can sense and respond to the physical characteristics of their surroundings through mechanotransduction mechanisms [2, 57, 58]. For example, when cells encounter a stiff ECM, they tend to adopt a more spread-out and flattened shape, whereas in a softer environment, cells may take on a more rounded and compact shape. This mechanical sensing can influence various aspects of cell behavior, including cell proliferation [59, 60], migration [59, 61], and differentiation [62, 63].

The ability of cells to respond to their environment through shape changes is critical for tissue homeostasis, development, and wound healing. It also has implications in disease contexts, such as cancer metastasis, where cancer cells can alter their shape in response to cues from the surrounding microenvironment, allowing them to invade and migrate to distant tissues. Understanding the intricate interplay between cell shape and the extracellular environment provides valuable insights into cellular behavior and tissue dynamics.

3 Cells in structured environments*

During the last two decades, cell mechanics, forces and shape have emerged as important elements of the way biological cells interact with their environment [2]. While the importance of controlling cells through biochemical ligands such as growth factors, hormones and cytokines has been appreciated from the very start of cell culture experiments, the insight that spatial control of cell adhesion, the physical properties of the ECM, as well as the mechanics of the cytoskeleton and the nucleus might be equally important for cellular decision making are rather recent insights. Not surprisingly, it was tied to the development of new tools that allowed researchers to better control the extracellular environment. This development started by transferring tools from the microfabrication of electronic devices into the life sciences, most notably microcontact printing to generate adhesive islands to control cell adhesion to planar substrates [64]. This lead to pioneering work that showed that cell fate can be controlled by the size of the adhesive islands: cells only survived on large islands and triggered apoptosis on small ones [50]. Later it was discovered that this switch is related to the translation of the transcription factor YAP/transcription regulator 1 (TAZ) into the nucleus in mechanically stressed cells [65].

Apart from geometry, extracellular stiffness has also been found to be a major regulator of cell behavior, and again this insight was tied to advances in materials preparation. Soft elastic substrates were introduced into cell culture with the main aim of measuring cell forces from the substrate deformations [66, 67]. However, through their use it was realized that substrate stiffness has a profound influence on single cell organization and migration [68] as well as on differentiation [69, 70]. For example on large islands, cells on stiffer substrates spread better and YAP/TAZ is translocated into the nucleus [65, 71]. It was also shown that extracellular stiffness affects the migration of cell collectives, which often behave as an effective supracell that can sense more shallow stiffness gradients than single cells [72]. Together, these historical developments prove that tools from materials science can be instrumental

*This chapter is based on the review Link, R., Weißenbruch, K., Tanaka, M., Bastmeyer, M., & Schwarz, U. S. (2023). Cell Shape and Forces in Elastic and Structured Environments: From Single Cells to Organoids. *Advanced Functional Materials*, 2302145. https://doi.org/10.1002/ADFM.202302145 [10].
In detail, we use Section 1, Section 2, specifically 2.1, 2.2, and 2.4, Section 3, specifically 3.1, 3.2, and 3.3, Section 4, and Section 5, all with small changes.

for promoting progress in the life sciences. In particular, they open the door for novel biomedical applications and therapies, like analysis of patient samples and tissue regeneration in the test tube.

Since its inception around three decades ago, the field of mechanobiology has seen dramatic growth, with many new tools and model systems entering the field. Most importantly, we have seen a shift from single cell studies to work with cell collectives, cell monolayers, 3D model tissues and organoids [73, 74]. As the field moved from 2D to 3D, imaging and force measurements became more challenging, but were met by new technologies. To image 3D cell assemblies, light sheet and two-photon microscopies have been helpful [75–77]. Today, forces can be measured in situ by inserting oil droplets [78] or elastic microbeads [79] into tissue. Optogenetics can be used to control cell forces in space and time [80]. Direct laser writing of 3D scaffolds has been adapted to cell culture conditions and used to control cell shape and forces in 3D [81, 82]. More recently, microfabrication has been used to control the organization of organotypic systems [83] and organoids in 3D [84]. In this chapter, we will review these recent advances.

3.1 Single cells

Single cells are the fundamental building blocks of life. While there is an enormous diversity in animal species and their cell types, the cytoskeleton, which determines the cell's mechanics and shape, is strikingly universal. It is primarily made up of three different filament systems: actin filaments, which together with the molecular motor myosin II are responsible for contractility and motility; microtubules, which are important for the positioning of organelles and directed transport processes within the cell; and intermediate filaments, which reinforce and complement the mechanics provided by actin and microtubules, especially in epithelial monolayers, which have to perform under very large strains [36]. While each filament system is well-investigated independently, the interplay between them is the topic of much ongoing research [12]. Very importantly, cell mechanics are also strongly determined by the mechanics of the nucleus, which is typically ten times stiffer than the cytoplasm and tightly integrated with the cytoskeleton through the LINC-complexes [85]. For a long time, it was argued that cells have to use their cytoskeleton to sense and calibrate mechanical cues from their environment [86], and today the nucleus should be added as an additional measurement devise [87, 88].

With the help of rationally designed cell environments, the exact impact of physical cues, such as substrate geometry and stiffness, on cell organization, mechanics,

behavior, and fate can be investigated. The best understood subsystem is cell adhesion to the ECM [14]. Transmembrane proteins from the integrin-family located on the cell surface enable cells to adhere to ECM proteins such as fibronectin or collagen. Through a large number of adaptor proteins, the integrins are mechanically connected to the actin cytoskeleton [89]. Using the myosin II molecular motors, the actin cytoskeleton of the adhered cell contracts, therefore pulling on its environment to test substrate stiffness [55, 90], adhesive areas [50], geometry [91] and curvature [92]. The signaling pathway from local force sensing to global cell changes is not yet fully understood, but it is clear that large-scale structures such as stress fibers and the nucleus play an important role as integrative elements. Cell-level effects have been observed for different cell types and on different length and time scales: the mechanical microenvironment can lead to polarization via symmetry breaking [93], remodeling of the cytoskeleton[94–96], traction force distribution [97], and durotaxis [90, 98].

3.1.1 Effect of extracellular stiffness on single cells

While traditional cell culture works with stiff glass or polystyrene substrates, in recent times soft elastic substrates have been established to expose single cells to physiological stiffness values or even to stiffness gradients [99]. A popular choice are hydrogels, which are hydrophilic polymer networks that are able to absorb large amounts of water, which gives them mechanical and chemical properties similar to the natural cell environment. Hydrogels can be manufactured to have elasticities similar to physiological tissue [100]. Due to their high-water content, nutrients and other soluble factors can be transported to and away from the cell [101]. The large amount of water in hydrogels leads to optical clarity, which thus allows for microscopy through the hydrogel. Hydrogels are often produced from synthetic polymers because naturally derived hydrogels have high variability in their physical and chemical parameters. However, while the global properties of synthetic hydrogels can be measured and engineered with high precision, the local microenvironment of the single cell inside both naturally derived and synthetic hydrogels is not necessarily reproducible [102, 103]. Hydrogels also lead to water flow under cell traction, which makes quantitative analysis challenging in certain situations [104]. Because cells locally exert nN-forces onto their environment through µm-sized focal adhesions, one needs elastic substrates with a Young modulus around $\mathrm{nN\,\mu m^{-2}} = \mathrm{kPa}$ to measure these forces [105]. For the widely used polyacrylamide (PAA) system, different combinations of monomer and crosslinker concentrations can achieve such values [106, 107]. In order to avoid water flow through hydrogels and also to achieve more

optical contrast at the substrate-medium interface, for example to perform reflection interference contrast microscopy [108], one can use elastic substrates made from the rubber material polydimethylsiloxane (PDMS). However, it is notoriously difficult to achieve stiffness in the sub-kPa for PDMS, because the material becomes very sticky and viscous. Therefore, different formulations with longer polymer chains have been developed [109].

Early work in this field used mainly PAA and revealed that focal adhesions and stress fibers develop well only on stiffer substrates, with the crossover typically at a few kPa [68]. It was then found that substrate stiffness also affects cell differentiation [69, 110]. Later, nuclear translocation of YAP/TAZ was revealed as the underlying molecular mechanism [65, 71]. When working with elastic substrates, it is important to keep in mind that different bulk elasticities typically correspond to different surface properties, such as roughness and porosity, thus potentially convoluting global and local properties. However, it has been shown experimentally that cells respond mainly to the bulk properties of the elastic substrates [111], validating the notion that they gain information by performing an elastic test on their environment.

3.1.2 Single cells in 2D structured environments

While the advent of mechanobiology was strongly fostered by the insight that soft elastic substrates can have a dramatic effect on cell behavior and fate, the same holds true for geometrical and topographical cues. The effect of structured environments on single cell behavior was first studied in 2D culture for single cells using adhesive micropatterning [50]. The main advantage of this method is that it produces precisely reproducible mechanical environments and therefore allows for experiments that lead to statistically relevant results. Adhesive micropatterns were initially produced by microcontact printing, but are often generated with photolithography or laser-based methods today [112]. The biggest challenge of these approaches is not necessarily to functionalize the materials with adhesion molecules, but rather to find materials with anti-fouling properties that reliably passivate the non-adhesive regions. Frequently used repulsive molecules comprise BSA, Pluronic and PLL-PEG. Moreover, gold-thiol based chemistry can be used to fabricate patterned self-assembled monolayers with distinct hydrophilic and hydrophobic areas on gold-coated coverslips [113]. However, the necessary gold coating restricts these methods to glass coverslips.

Today, a zoo of interesting shapes has been established that allows us to investigate important biological questions with high resolution, like V-shapes for cell spreading, crossbows for polarized cells and H-patterns for cell doublets. Because cells only have a limited amount of cytoskeletal and membrane material available, the size of these

patterns must be adapted to the cell type under consideration. Once these reservoirs are exhausted, the cells run into the danger of rupturing their own membranes [114].

A prime example of the power of 2D adhesive substrates is the study of stress fibers, which are contractile actin bundles formed by many animal cell types. As an example, Fig. 3.1a,a′) shows a cell on an adhesive cross pattern, where the stress fibers form as invaginations at the four positions where the cell has to bridge inwards corners. This experiment reinforces the early insight that micropatterns can be used to control the exact position of stress fibers [96]. By varying the shape of the adhesive areas, the authors showed that stress fibers grow predominantly along non-adhesive edges, and that the strength of stress fibers depends on the distance between adhesive sites and the number of stress fibers in the cell. Furthermore, they were able to observe the spreading of a single cell on the micropattern, which revealed an approximately linear increase of the curvature radius over time. In the absence of stress fibers, cell shape invagination along non-adhesive edges is increased, showing that actin stress fibers counteract the contracting cell cortex and tend to pull the boundary straight.

Stress fiber growth, organization and force transmission is still a very active area of research, but today focuses more on the underlying mechanisms. It has been known for many years that stress fibers are formed by merging small actin bundles moving through the cytoplasm [115], which makes the formation of the stress fiber network in single cells is a complex process and difficult to predict. Micropatterns were used to provide reproducible environments for cells to spread, which allowed the prediction of stress fiber networks of cells on micropatterns from the cell spreading history [35]. To better understand stress fiber self-organization in stationary cells, Jalal and colleagues plated fibroblasts on circular micropatterns, see Fig. 3.1b,b′). Using live cell imaging, they observed transitions between circular, radial, and linear orientations and show that they depend on molecular players such as non-muscle myosin II and α-actinin [116, 117].

Micropatterns are often used to observe cell polarization and migration under reproducible conditions. In the “world cell race”, over 50 cell types were placed on fibronectin-coated tracks, see Fig. 3.1c,c′), and their polarization, speed and persistence were evaluated, revealing a universal correlation between speed and persistence [118, 119]. By gradually increasing the density of adhesive sites, see Fig. 3.1d,d′), Autenrieth and colleagues showed that the well-known process of haptotaxis, where fibroblast cells move in the direction of the highest ECM protein concentration, holds true for discrete adhesive sites as well [120]. Brückner and colleagues used a two-state micropattern, see Fig. 3.1e,e′), to show that the motion

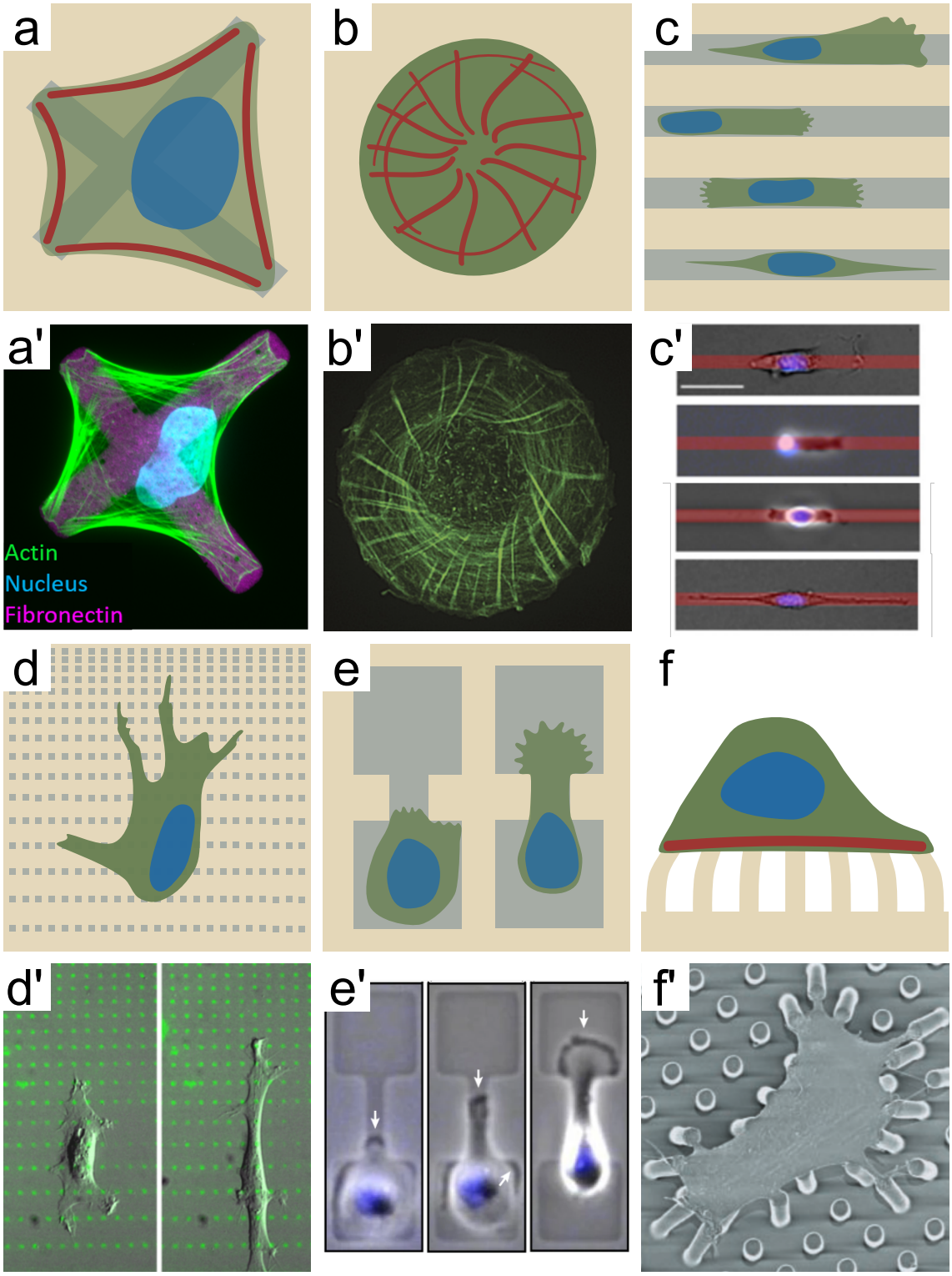
a
b
c
a'
Actin
Nucleus
Fibronectin
b'
c'
d
e
f
d'
e'
f'

Figure 3.1: **2D environments for single cell experiments. a,a′**) Schematics (a) of a single cell on a cross pattern with nucleus (blue) and stress fibers (red), image (a′) stained for actin (green), nucleus (blue), and fibronectin (magenta). **b,b′**) Schematics (b) and image (b′) of a single cell on a circular micropattern with different types of stress fibers (red). **c,c′**) Schematics (c) and image (c′) of a human skin fibroblast (top row), human mesenchymal stem cell (second row), human malignant melanoma (third row), and murine fibroblast on fibronectin tracks. **d,d′**) Schematics (d) and image (d′) of a single fibroblast cell on a substrate with discrete fibronectin sites of varying density. **e,e′**) Schematics (e) and image (e′) of a single cell on a two-state pattern. **f,f′**) Schematics (f) and image (f′) of a single cell on micropillars.
b′): Reproduced with permission [116], 2019, The Company of Biologists. c′): Reproduced with permission [118], 2012, Elsevier. e′): Reproduced with permission [121], 2019, Nature. f′): Reproduced with permission [122], 2003, National Academy of Sciences, U.S.A. All other images reproduced with permission [10], 2023, Wiley.

of a single cell through a constriction has both deterministic and stochastic contributions [121]. While wildtype cells crossed by stochastic transitions between two stable states, cancer cells were deterministically driven over the bridges in an oscillatory manner.

To measure cell forces in micropatterning experiments, one can combine planar soft elastic substrates with adhesive micropatterning [123, 124]. From the deformations of the elastic substrate, the cellular forces are calculated using the deformation of the micropatterns themselves or standard traction force microscopy [125]. In traction force microscopy (TFM), the displacement field of beads in the elastic substrate is used to calculate traction forces, usually by solving the inverse problem of elasticity theory. Length measurements of the deformed micropatterns can be performed in a high-throughput manner, but the dependence between force and length change depends on the geometry of the micropattern and must be calibrated with standard traction force experiments [124]. Micropatterns can also be used to control the actin cytoskeleton network, specifically the growth of stress fibers, allowing for reproducible settings and the measurement of traction forces after the photoablation of stress fibers [126].

Another method to measure cellular forces in well-controlled elastic environments are micropillar arrays, see Fig. 3.1f,f′). These are uniformly distributed cantilevers of equal size typically made of polymer material such as PDMS and can be used as a rationally designed mechanical environment in single cell experiments [112, 127]. Compared to micropatterns, cells subjected to micropillar environments have larger variations in cell shape. A major disadvantage is that the topography of such environments leads to cell processes being sent into the space between the pillars.

This can be avoided by passivating the pillar sides. Traction forces can be calculated from Euler-Bernoulli beam theory with corrections resulting from substrate warping [128, 129].

Cellular force generation can also be artificially altered by interfering genetically, chemically, or optically with the cell cytoskeleton [130]. One of the most exciting developments in this field is non-neuronal optogenetics. Optogenetics is a method where cells are genetically modified to make specific proteins light-sensitive. These cells can then be targeted by light, for example to contract actomyosin with a high spaciotemporal precision [131]. Optogenetics as a tool to manipulate the cell cytoskeleton was first used to control cell migration of HeLa-cells by photoactivating Rac1 [132]. The design of optogenetic switches has proven to be a challenging task due to the complex feedback loops used by cells to control their cytoskeleton. An interesting approach is to combine optogenetics with adhesive micropatterning. For example, de Beco and colleagues investigated the gradient formation of Rac1 and Cdc42 during cell migration for single cells on circular micropatterns with optogenetic activation [133]. Recently, optogenetics has been used to revert cell migration in one-dimensional situations [134, 135]. Optogenetics has also been combined with traction force microscopy to show that cell forces can be switched on and off by light [80, 136]. A recent combination with adhesive micropatterning revealed that cell size and actin architecture determine the dynamical response to such activation [137].

In addition to adhesive cues, cell behavior also depends on the curvature of the microenvironment, a process called “curvotaxis”. With initial observations that chicken heart fibroblasts on glass bars align along the minimal curvature line [138], it was later found by Pieuchot and colleages that both fibroblasts and mesenchymal stem cells use their nucleus to measure the local curvature and migrate towards concave valleys [53]. Werner and colleages used stereolithography to manufacture concave and convex hemispheres for cells to adhere to [139]. Mesenchymal stem cells increase their migration speed in concave environments, wheras cells in convex environments experience higher forces on their nucleus, which influences cell differentiation. For a detailed review on curvotaxis we refer to the work of Callens and colleagues [92].

3.1.3 Single cells in 3D structured environments

In vivo, cells live in a 3D environment, and the difference between a 2D and a 3D environment can be sensed by cells [140, 141]. Traditionally, the majority of single cell experiments was performed on stiff glass or plastic substrates, and the shift to include the 3D mechanical environment in the design of cell experiments only started in the 2000s [142]. The shift from 2D to 3D environments was made

possible due to advances in materials science and imaging, however, identifying the relevant mechanical factors in the local cell environment is more challenging than in 2D [143]. Cells in 2D versus 3D environments show differences not only in internal organization and morphology [140, 144], but also in cell migration [145], adhesion [146], and mechanotransduction [147]. There are many approaches to investigate cell fate and behavior in 3D environments, including the use of 3D hydrogels [99, 148] or 3D printed microfluidic devices [149].

Cells in 3D hydrogels, in particular the physiologically most important case of collagen gels, interact with their surroundings in a more distributed manner than in 2D, see Fig. 3.2a,a′), and this difference influences cellular mechanosensing, migration and growth [150]. As seen in Fig.3.2a), cell shapes in 3D collagen gels also show the invaginated arcs found for cells on adhesive micropatterns (compare Fig.3.1a), because the same competition between cortical surface tension and line tension in the contour is at play in 3D as in 2D [151, 152]. Similar to 2D traction force microscopy, beads can be placed in the hydrogel to measure the displacement. The displacement is then used to calculate the forces exerted by the cell, but the technical challenges are much larger in 3D than in 2D, due to the required 3D imaging and the complicated mechanical properties of the 3D gels, which necessarily have to be porous to allow for nutrient supply [153]. A different approach for using hydrogels to observe cellular force sensing is to spatiotemporally change the hydrogel stiffness with light and to observe cellular reactions to stiffness changes [154]. Some 3D hydrogels, for example alginate, can also be manufactured with 3D printing, allowing for printed microvascular environments [155, 156]. Micro-and nano-contact printing can also be used in combination with some hydrogels such as PAA. Tabdanov and colleagues [157] contact printed nano lines onto PAA hydrogels and showed that both actin and microtubule network architecture differed between in-groove and on-ridge regions. Similar scaffolds have been used as a platform to improve T-cell migration in 3D, by both pharmacologically and genetically manipulating the microtubule-contractility axis [158].

Cells need space and nutrients to survive in 3D environments, and rather than using the porosity of the 3D matrix, one can generate compartments for cell culture within the matrix. Minc et al. placed single sea urchin eggs into PDMS microfabricated chambers and observed the cell division axis relative to the shape of the chamber, see Fig. 3.2b,b′) [6]. In general, large eggs from marine organisms are a very useful model system because they interact little with their environment and are very large, thus providing good imaging conditions. The cavities with different geometries have the same volume as the eggs, which are forced into a given cavity

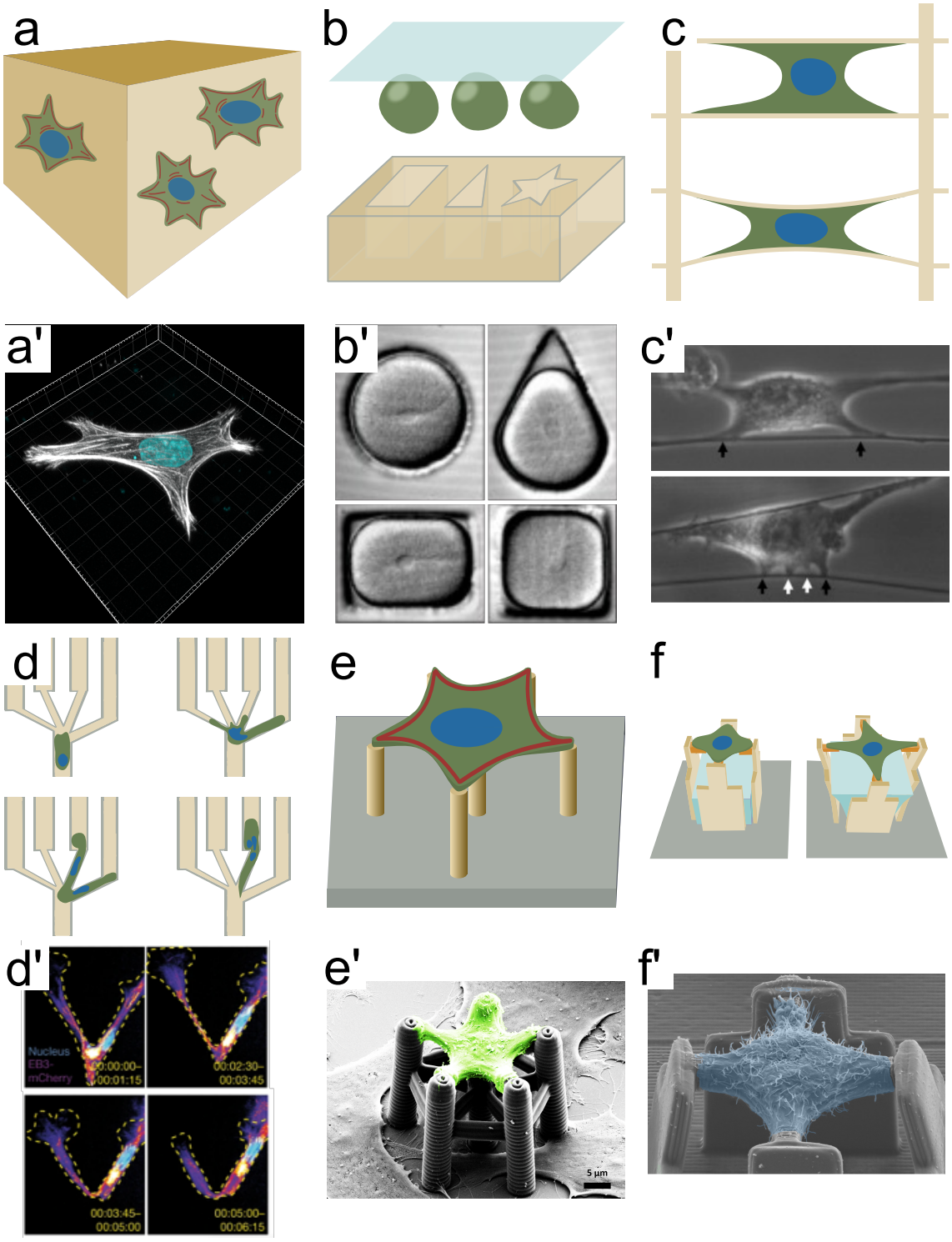
a
b
c
a'
b'
c'
d
e
f
d'
e'
f'
Nucleus
EB3-mCherry
00:00:00–00:01:15
00:02:30–00:03:45
00:03:45–00:05:00
00:05:00–00:06:15
5 µm

Figure 3.2: **3D environments for single cell experiments. a,a′**) Schematics (a) of single cells in hydrogel and image (a′) of a single cell in 3D collagen. **b,b′**) Schematics (b) and image (b′) of sea urchin eggs in microfabricated chambers. **c,c′**) Schematics (c) and image (c′) of a single cell in a nanonet structure. **d,d′**) Schematics (d) and image (d′) of a dendritic cell in a channel with varying pore sizes. **e,e′**) Schematics (e) and image (e′) of a single cell in a structure manufactured with direct laser writing (DLW). **f,f′**) Schematics (f) and image (f′) of a single cell in a 3D microscaffold with reversible host-guest system.
b′): Reproduced with permission [6], 2011, Elsevier. c′): Reproduced with permission [159], 2016, Elsevier. d′): Reproduced with permission [88], 2019, Nature. All other images reproduced with permission [10], 2023, Wiley.

geometry with a coverslip, see Fig. 3.2b). This study showed that the microtubule cytoskeleton positions the nucleus at the center and the division axis can be predicted by minimizing the microtubule force and torque in the cell [6]. Actin polymerization, the formation of focal adhesions and actomyosin contractility is also affected by geometrical constraints. Bao and colleagues controlled the size and shape of human mesenchymal stem cells in different 3D cavity geometries and sizes and showed that stress fiber density and distribution depend on both cell volume and shape [160].

A versatile method to mimic the mesh-like structure of the 3D ECM is electrospinning of polymer/protein nanofibers [161]. To date, nanofibers based on silk proteins [162, 163], collagen [164, 165], and gelatin [166] have been used for various applications, including wound healing and tissue engineering [167–169]. Although naturally occurring protein nanofibers do not need any additional crosslinkers, the Young's modulus of polymer/protein nanofibers can be controlled either by adding bifunctional crosslinkers[170] or by modifying the side chains by photocrosslinkers [171]. Inspired by biological systems, crosslinker-free nanofiber materials have also been designed [172, 173]. It is well established that the elasticity of fibrous ECM is dynamically modulated during diseases and development. To model dynamic changes in fiber elasticity accompanied with ECM remodeling, Hayashi and colleagues developed a gelatin-based nanofiber system that can modulate the Young's modulus by using reversible host-guest crosslinkers [174]. Methods to fabricate 2D meshes can also be used to manufacture 3D structures, for example by combining electrospinning with 3D printing [175] or by placing the syringe on a freely moveable platform [176]. 3D scaffolds produced with electrospinning are used to increase cell growth and viability for tissue engineering applications [161]. Nain and colleagues used non-electrospinning STEP (spinneret-based tunable engineered parameters), to enable a precise manufacturing of micro- or nanofiber thickness and position, see Fig. 3.2c,c′) [177]. Scaffolds produced with the STEP technique are called Nanonets

and can be used to measure mechanical forces and to test the single cell response to external forces [159]. When cells are seeded on the fibrous scaffold, they test their environment by pulling on the fibers. Again, one nicely sees the invaginated arc morphology resulting from the interplay of the different types of tension. From the displacement of the fibers one can then calculate the forces exerted by the cell. With the use of a micropipette puller, one can also pull on a nanofiber that the cell is attached to and measure the adhesion forces of the cell [159]. By changing the spacing between fibers within a scaffold, Jana et al. recently showed that the morphology and migration behavior of single cells strongly depends on fiber density [178]. Cells on dense networks are elongated and have longer persistence lengths than on intermediate and wide networks.

3D structured environments can also be used to study cell migration in more physiological environments. Renkawitz and colleagues engineered a channel system to guide amoeboid cells, specifically dendritic cells, to a decision point, from which pores with width between 2 and 5µm pan out [88], see Fig. 3.2d,d′). Amoeboid cells typically migrate with the microtubule organizing center (MTOC) behind the nucleus, while mesenchymal cells usually have the MTOC and the Golgi apparatus in front of the nucleus. They found that the nucleus of dendritic cells in the channel is drastically deformed and protrudes into several pores before the cell proceeds into one of them. Decoupling the decision point from the constriction of the pore leads to a loss of pore-size preference, showing that the cells use their nucleus to measure the pore sizes. This explains why it is useful for amoeboid cells to migrate nucleus-first: it allows for a fast probing of the environment and a quick decision making [88]. Using 3D nanofiber-based matrix with different degrees of crosslinks and tunable porosities, Huang at al demonstrated that cancer cells invasively migrate into nanofiber stacks, while non-tumorigenic cells do not [179].

Traditional micropatterning requires the use of masks and is very time-consuming. This promises to be revolutionized by 3D additive manufacturing methods. The use of scaffolds manufactured with DLW/3D nanoprinting, see Fig. 3.2e,e′), has the great advantages of allowing for rationally designed 3D environments as well as a high reproducibility [180]. In 3D nanoprinting, a femtosecond-pulsed laser beam is used to excite photopolymerizable resists. Given the pulsed nature of the laser beam, two-photon polymerization is achieved, allowing to precisely polymerize material only in the focal voxel of the laser. By moving the laser focus along predefined trajectories, complex 3D structures with nano-resolution can be fabricated. With the use of two different polymers, selected parts of the printed structures can be made adhesive, which gives additional possibilities for the scaffold design [81, 152].

Similar to nanonets, structures manufactured with 3D nanoprinting can be used to measure forces of single cells positioned on beam-type structures. Klein and colleagues used chicken primary cardiomyocytes, which start contracting after 1-2 days after seeding onto the structure [181]. The deformations of the 3D printed beams were measured and used to calculate the forces exerted by the cells. 3D structures fabricated with DLW were also used to compare the volume of nuclei and cells in 2D and 3D environments [182]. Fibroblast-like cells have a larger volume and nuclei in 3D compared to 2D environments, while there was no significant difference for epithelial-like cells. With the use of different photoresists, structures were deformable or non-deformable for cells. The soft and stiff 3D environment did not change the cell volume significantly [182].

3D structured environments fabricated with 3D nanoprinting improved cardiomyocyte derivation from pluripotent stem cells [183]. 3D rectangular and hexagonal scaffolds were used both to constrain single stem cells geometrically and as contact points for cell attachment. The rectangular shape led to parallel alignment of myofibrils and an improved Ca^{2+} reuptake [183]. 3D nanoprinting is also suitable to manufacture systematically varying sizes and shapes of so-called 2.5D microwells, which are open on the top side to allow cells to spread inside the chamber. By changing only a few parameters such as size and shape, the effects of these parameters on single cells can be observed in experiments. These structures were used to investigate the mechanotransduction via YAP in mouse embryonic stem cells [184]. While the cell division rate increases with increasing adhesive area on 2D substrates, it decreases with increasing well size in 2.5D [184]. More recently, Hippler and colleagues introduced a stimuli-responsive host-guest system, see Fig. 3.2f,f′), to measure cellular forces during cell stretching using structures fabricated with DLW[185], see Fig. 3.2f). With this host-guest system, cells can be stretched in a well-defined temporal and spacial manner. An advantage of this technique is that cells can be chemically fixed at any point during the experiment, allowing for a comparison of the actin cytoskeleton during and after stretching [185].

3.2 Cell collectives and monolayers

Tissue function requires not only the spatiotemporal regulation of subcellular structures, but also a coordinated cellular behavior across scales [186]. Tissues are composite materials comprising of different cell types and the ECM, which in turn is composed of three classes of macromolecules: collagens, proteoglycans, and non-collagenous glycoproteins. From a materials perspective, collagens resist tensile

stress and proteoglycans resist compressive strain, while glycoproteins mainly serve as a type of glue by presenting binding sites for the cells [187, 188]. Individual cells in the tissue are mechanically linked together via different classes of cell-cell adhesions, mediated mainly by the cadherin superfamily [189], or indirect via cell-ECM adhesions, mediated by the integrin family [190]. Intracellular adaptor proteins and linker molecules connect these transmembrane anchors with the cytoskeleton, most notably actin filaments and intermediate filaments [191, 192]. Due to this network architecture, tissues exhibit far more complex mechanical behaviors than linearly elastic materials, including viscoelasticity, nonlinear elasticity and mechanical plasticity [193, 194].

Tissues have to cope with a large range of mechanical challenges. During development and regeneration, spatial patterns of cell growth [195, 196] or contraction of adjacent tissues [197] can generate mechanical stresses that expand, push, bend, fold, and twist distinct cell populations into specific 3D forms [92, 110]. For example, one strategy to build an organism in 3D is to first build a 2D cell layer which then can be folded. The best-known case is the fruit fly, which forms a cell monolayer through its first 14 divisions that then is folded during gastrulation. In general, mechanical processes such as folding or buckling lead to complex folded and branched structures in our organs, such as in the lung, kidney, brain, intestines or in the circulatory system [198]. The remarkable degree of self-organization, cooperation and synchronization across individual cells in a multicellular mechanical network has led to the paradigm that certain cell collectives behave as higher-ordered 'supracells' [199–202]. Spatial induction of fate-determinants [203, 204], nonlinear interactions between individual cells or the ECM [205, 206], and cell-to-cell variability[207, 208] enable symmetry breaking and pattern formation from a previously unspecified and homogenous population of cells. Although the induction of pattern formation is to a certain degree genetically encoded [209–211], full engagement and reinforcement of heterogenous cell patterning requires implementation of multicellular forces and compartment boundaries from the ECM [1, 212, 213]. In certain cases, mechanics might be even equally important. Palmquist and colleagues found that mesenchymal mechanics are sufficient to spontaneously shape the regular morphological pattern of feather follicles in the skin of chicken embryos ex vivo and in the absence of fate-determining molecular programs [214, 215]. Similar, Cohen and colleagues showed that the development of periodic checkerboard-like pattern of hair cells and supporting cells in the mammalian hearing organ of Corti is based on mechanical forces rather than signaling events, as global shear and local repulsion forces on hair cells were sufficient to drive the transition from disordered to ordered cellular pattern

[216]. Thus, investigating the bi-directional influence of ECM geometry and tissue morphology in rationally designed cell culture environments bears the potential to dissect complex morphogenetic processes during tissue formation in simplified and controllable in vitro systems.

In contrast to single cells, cell collectives have a stronger power to change their environment, which then can feed back onto the collectives. To permanently shape tissues during developmental and regenerative processes, cells have to structurally reorganize the surrounding ECM by degrading, realigning or secreting new ECM molecules, processes that typically occur on the time scale of hours to months [217]. These processes are often triggered or modulated by mechanical stresses that result from cellular growth and the subsequent increase in surface, volume and density [110]. The structure of the surrounding ECM vice versa influences the induction and magnitude of multicellular mechanical stresses. With today's abilities in microfabrication, engineered cell culture substrates can address many aspects in this regard, by tuning the rigidity of the substrate, by patterning or shaping the size of the adhesive domains, or by including repulsive areas and physical barriers in the substrate [64].

3.2.1 Cell collectives on elastic substrates

For cell collectives, elastic substrates have revealed many surprising processes that would have gone unnoticed otherwise. The most studied model system for collective migration are sheets of epithelial cells migrating into open space after the removal of a confining barrier. This assay has been developed as a version of the traditional wound healing assay, but avoids the damage afflicted by the traditional scratching approach [218]. When combined with elastic substrates, it allows to perform traction force microscopy and even to reconstruct stresses inside the cell sheets, using an approach called monolayer stress microscopy [219, 220]. Using TFM and monolayer stress microscopy on soft elastic substrates, it has been shown that higher substrate stiffness correlates with increased collective migration speed, persistence, directionality and coordination of epithelial monolayers. This effect is caused by stiffness sensing at the edge of the cell colony and force transmission between cell-cell-contacts [59]. Sunyer and colleagues went one step further and used fibronectin-coated PAA hydrogels with a stiffness gradient to show that sheets of epithelial cells are able to sense and collectively migrate towards the higher stiffness (durotaxis) [72]. While durotaxis has been described before for single cells [98], these experiments revealed that the collectiveness increased the durotactic sensitivity due to long-range intercellular force transmission in the colony, highlighting the supracellular aspect [61, 72, 221]. A

comparable behavior was observed for Xenopus neural crest cells (a multipotent mesenchymal cell population), which were shown to migrate in distinct clusters towards higher stiffness on PAA hydrogels [222]. During migration, these clusters showed a higher-ordered supracellular behavior, with collectively coordinated actin polymerization at the migratory front and synchronous collective contraction at the clusters rear end [200]. Strikingly, using in vivo atomic force microscopy, the group showed that the neural crest cells not only sense the gradient through cell–matrix adhesions, but also induce the gradient formation via N-cadherin mediated cell-cell interactions and softening of the underlying placodes, thus self-generating the stiffness gradient on which they migrate in vivo [222]. Importantly, these results are not restricted to stiffness gradients. When Clark and colleagues monitored the collective cell migration of human squamous cell carcinoma or colorectal carcinoma cell clusters on homogenously elastic PAA gels coated with deformable collagen I networks, they found that the cells generated asymmetric collagen densities and alignments underneath the cluster in the absence of any biochemical cue [223]. Thus, the cells self-steer their migratory persistence by generating a viscoelastic gradient in the collagen fiber network.

The concept that cell collectives self-generate durotactic/mechanical gradients opens new research directions that will shape our current understanding of how mechanoreciprocity between cells and the ECM steers collective cellular behavior during embryonic development, metastasis spreading, wound healing and more [224–227]. For example, a long-standing research question with contrary results is how cancer cells interact with their stroma, which is often stiffer than comparable healthy tissue [228, 229] while the cancer cells themselves tend to be softer [230], in order to collectively invade foreign tissue during metastasis formation [60]. As this process requires detachment from the primary tumor site, intra- and extravasation of basement membranes, and collective migration through interstitial matrices, tumor collectives must breach several barriers and perform long-range migration through tissues with various stiffness. The stiffness of PDMS substrates was shown to promote epithelial-mesenchymal transition of MDCK cells, a process linked to cancer dissemination [231]. However, it remains unclear how stiffness-induced malignancy is maintained over time after cancer cell dissemination in vivo. Self-generated gradients could allow cell collectives to operate over greater ranges of stiffness, larger distances, and longer time [232, 233].

3.2.2 Cell collectives in 2D confining environments

Like for single cells, 2D micropatterns are a very popular method to generate confining environments for cell collectives, because microscopy is easy with planar substrates. Microcontact printing, photolithography techniques and spotting-based molecular printing [234] are among the most frequently used methods to transfer desired 2D shapes on coverslips or PDMS/PAA hydrogels [64, 235]. Raghavan and colleagues even developed a double microcontact printing approach to pattern gold-coated coverslips with self-assembled monolayers that include a region, which can be electrochemically switched from non-adhesive to adhesive, allowing to temporally control confinement release [236]. Alternatively, large scale boundaries can be created via physical obstacles of a desired shape, which can be placed permanently or transiently via magnetic stencils [72]. Transient application of a growth restricting obstacle has the advantage that the confinement can be released at a defined time point, allowing to add the temporal dimension more easily.

As already mentioned above, 2D micropatterns with such confining barriers are very well suited to investigate different aspects of collective cell migration. As the adhesive area on which the cells are able to migrate can be rationally designed, it is possible to guide, restrict or coordinate the movement of the cell collective. These approaches replaced the classic 'scratch assay' and allow to tackle fundamental questions on how cells generate distinct migration patterns in much more refined assays. Vishwakarma and colleagues used PAA hydrogels with a removable barrier to investigate how leader cells are selected for their function in collectively migrating epithelial monolayers, and found that upon confinement release, leader cell territories emerge in response to force transmission from the follower cells [237]. By designing stencils with different shapes, they showed that the distance between leader cells converges to a typical value of around 170 µm set by the mechanics of the cell monolayer. Vazquez and colleagues added a removable magnetic physical barrier with triangular cavities to a PDMS hydrogel in order to spatially control the protrusion formation in the cellular monolayer [238]. In another approach, pillar stencils have been used to fabricate micro-gaps of desired shape and size in epithelial monolayers [239]. Since the number, shape and size of the barrier stencil can be individually shaped as desired, this approach is scalable and allows gap closure monitoring along several spots, as a model for wound healing.

In contrast to wound healing assays, where cells move into an open space, micropatterns that restrict the migratory space can be used to guide the migratory cells along spatially defined routes, in order to monitor how spatial confinement affects the speed and directionality of migrating cell collectives. Vedula and colleagues [240]

as well as Marel and colleagues [241] fabricated adhesive strips of different width and monitored collective cell migration speed and persistence. Using particle image velocimetry, they found a negative correlation between the overall migration speed and the width of the adhesive strips [240]. Other groups used confining patterns to monitor distinct motion patterns inside the cell colony. Peyret and colleagues showed that epithelial cells exhibit coherent oscillations when confined on micropatterns of varying shapes and sizes, with period and amplitude of the oscillations being dependent on the substrate size [242]. Another advantage of this approach is that the size of the adhesive pattern can be adjusted in order to tune the number of cells that are able to adhere to the substrate. Segerer and co-workers monitored the spontaneous formation of vortices on micropatterned circles, see Fig. 3.3a,a′), and found that the persistence of coherent angular motion increased with the number of confined cells [243]. Finally, asymmetries can be incorporated in the pattern, in order to guide collective cell polarization and migration [244]. For instance, Rausch and colleagues plated cells on stencil-masks with varying local curvatures, see Fig. 3.3c,c′). They showed that high curvature areas induce leader cells formation, and moreover that polarization of the cells and high traction forces are present in areas of high curvature even before migration [245]. This growth guidance can in principle be mapped towards any desired 2D shape, from straight lines to branching points up to complex mazes, monitoring cellular path finding and decision-making branching morphogenesis.

Besides collective cell migration, 2D micropatterns have proven valuable for ongoing research on how crowding and confinement affects cellular fate decision. As mentioned above, distinct patterns of cellular growth lead to different mechanical stresses at the edges of boundaries and in the center of the mass, respectively. It is an ongoing debate, how these different stresses affect cellular decision making. Depending on the cell type, different stresses might lead to the induction of differentiation, proliferation, or apoptosis, respectively. Nowadays, the flexibility in terms of shape and size of 2D micropatterns allows to precisely induce, guide, map and monitor these stresses in cell colonies over time. Thus, micropatterned substrates are frequently used to decipher how different stresses are transduced on the molecular scale, in order to guide cell differentiation and cellular fate decision. Gomez and colleagues showed that mouse mammary epithelial cells are under high mechanical stress along the edges of different substrate geometries that were printed on glass via microcontact printing, and that these cells preferentially undergo epithelial-to-mesenchymal transition, while the cells in the center did not [246]. Strikingly, inhibiting cytoskeletal tension abrogated the spatial patterning of the epithelial-to-mesenchymal transition. In contrast, Wei

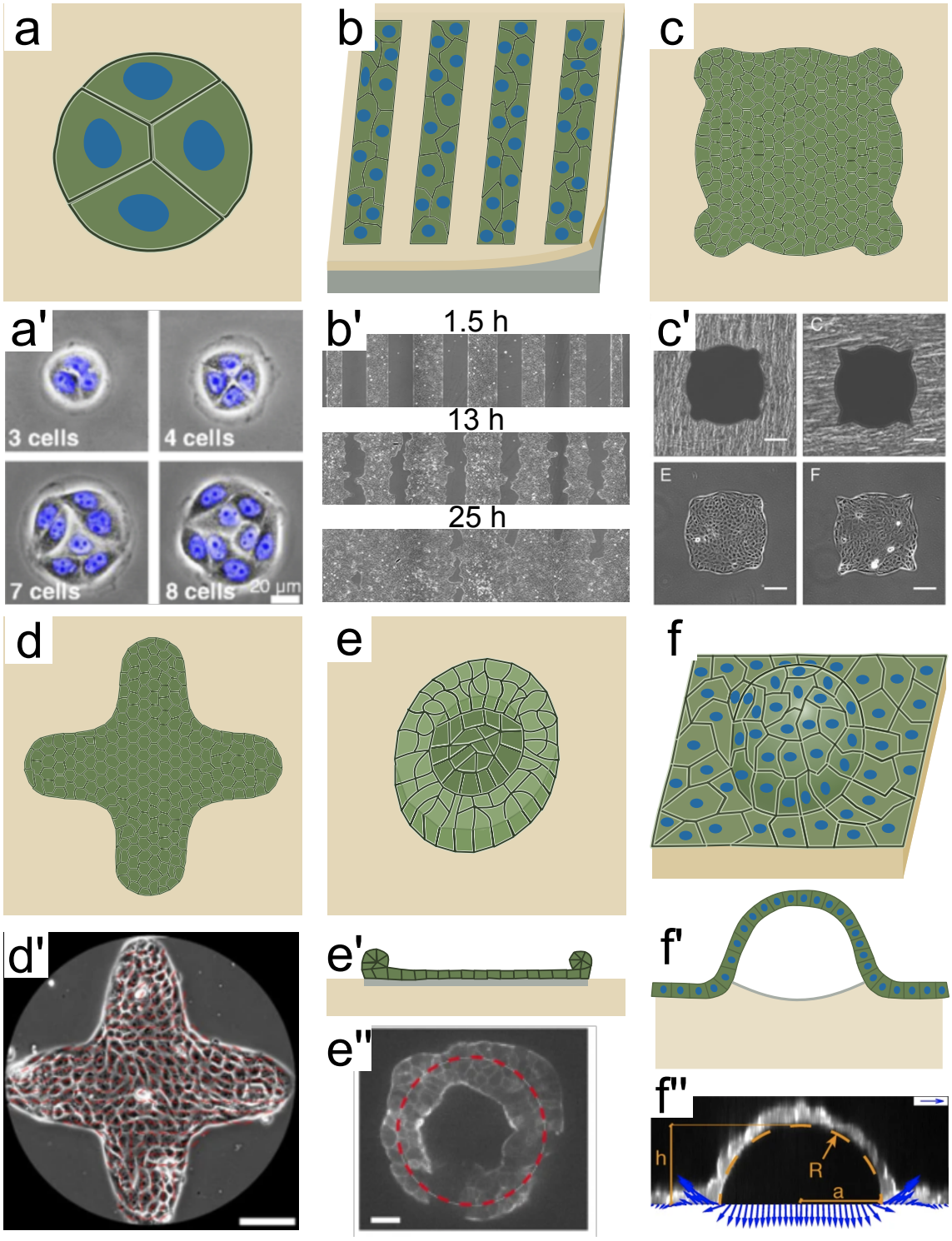
a
b
c
a'
3 cells
4 cells
7 cells
8 cells
20 µm
b'
1.5 h
13 h
25 h
c'
C
E
F
d
e
f
d'
e'
e''
f'
f''
h
R
a

Figure 3.3: **2D environments for experiments with cell collectives.** **a,a′**) Schematics (a) and image (a′) of circular micropatterns to study collective cell migration. **b,b′**) Schematics (b) and image (b′) of a wound healing assay with a removable microstencil. **c,c′**) Schematics (c) and image (c′) of cell collectives on micropatterns to analyze the influence of geometry-based cues. **d,d′**) Schematics (d) and image (d′) of microcontact printed cell monolayers to investigate cell extrusion. **e,e′,e″**) Schematical top (e) and side (e′) view of adhesive cellular patterns to study monolayer development into the third dimension. **e″**) Image of the confocal ring. **f,f′,f″**) Schematic top (f) and side view (f′) of epithelial cells coated seeded on soft PDMS substrate with micropatterned nonadhesive areas. **f″**) Image of the side view and measured traction forces.
a′): Reproduced with permission [243], 2015, American Physical Society. b′): Reproduced with permission [218], 2007, National Academy of Sciences, U.S.A. c′): Reproduced with permission [245], 2013, American Institute of Physics. d′): Reproduced with permission [247], 2017, Nature. e″): Reproduced with permission [248], 2014, Nature. f″): Reproduced with permission [249], 2018, Nature. All other images reproduced with permission [10], 2023, Wiley.

and colleagues did not observe increased epithelial-to-mesenchymal transition when they cultivated single MDCK epithelial cells on circular micropatterns [231]. These results suggest that both multicellular confinement, and the shape of the geometric boundaries are important for the observed effects. This is in line with findings from Nelson and colleagues, showing that regions of concentrated growth corresponded to regions of high traction stress within a cell sheet on micropatterned substrates, while inhibiting actomyosin-based tension or cadherin-mediated cell-cell connections disrupted the spatial pattern of proliferation [110]. Similarly, researchers from the lab of Gregory Underhill fabricated elastic PAA hydrogels for traction force measurements and spatially deposited collagen in circular shapes onto the hydrogel via microcontact printing [250]. Using this approach, they found that liver progenitor cells exhibited patterned differentiation in response to spatially controlled downstream mechanotransduction. On the boundary, cells expressed high E-Cadherin levels and exerted higher traction forces, leading to increased biliary differentiation in this region, whereas cells in the interior differentiated towards the hepatocytic lineage [250, 251].

These results clearly show that cell differentiation patterns arise from the mechanical status of distinct cell populations, which is in turn dependent on the ECM geometry and the boundaries. A natural path forward is to focus future research on deciphering the molecular downstream pathways that convert these mechanical signals into biochemical reactions. In this spirit, Muncie and colleagues cultivated human embryonic stem cell colonies on patterned hydrogels of soft nature (0.4-2.7

kPa) that recapitulate the biophysical properties of the early embryo [252]. They found that specific geometries promoted local areas of high adhesion-mediated tension that enhanced spatial patterning of morphogens, ultimately inducing mesoderm specification. Of note, the clever integration of microfluidic devices in the hydrogels even allows to mechanically stretch the microtissues by controlling the pressure in the micropatterned compartments, leading to either negative or positive out-of-plane deformations of the epithelial monolayer [252, 253]. Using this approach, Blonski and colleagues showed that inward bending of the epithelium led to high tension in the adjacent cells next to the imposed negative curvature, inducing the spread of calcium waves, while positive curvature resulted in the opposite and prevented calcium spread [253]. Thus, these studies demonstrate creative ways to combine soft elastic substrates, micropatterning, and active mechanical perturbation in order to investigate the conversion of mechanical cues into biological patterning mechanisms [252].

Another interesting direction from the biophysical and biomechanical perspective is the transition from 2D to 3D growth due to confinement and cellular crowding. Given that cell proliferation in the restricted area leads to a finite population size in 2D monolayers, cells react to this either by growth arrest or by cell extrusion, ultimately extending the growth in axial direction and forming multilayered cell sheets. Saw and colleagues investigated cell extrusion in confined environments, see Fig. 3.3d,d′, and found that it is not cell density, but topological defects that lead to cell extrusion and apoptosis [247]. Mechanically, folding or buckling is a sudden out-of-plane collapse of a material caused by an increasing in-plane compressive load [254]. In order to monitor tissue folding and buckling in vitro, compression or confinement can be engineered by restricting the growth area of cells on the substrate [110, 249, 255]. Deforet and colleagues monitored the latter process by confining cellular monolayers on circular micropatterns, see Fig. 3.3e-e″), and found that cellular rims formed along at the periphery of the substrate because of the additional degree of freedom of the border cells and independent of the substrate size [248]. Saw and colleagues showed that cells are extruded at topological defects; in analogy to nematic liquid crystals, these are places of high elastic energy in the sheet [247]. These results demonstrate that epithelial confinement alone can induce morphogenesis-like processes including spontaneous collective extrusion and transition from 2D to 3D.

Cell extrusion is not needed when the whole monolayer can escape into the third dimension to relax its growth stress. This process has recently been controlled using adhesive micropatterning. Latorre and colleagues cultivated an epithelial monolayer on adhesive PDMS gels that were interspersed with non-adhesive islands,

see Fig. 3.3f-f″). The cells eventually overgrew the islands and formed pressurized cellular domes above these restrictive areas. The pressure within the domes was measured with 2.5D TFM. This experiment revealed the unusual elasticity of the cell monolayer, which showed strain values of up to 1000 percent, which until then has been known only for the "superelasticity" of metal alloys [249]. Similar to the case of the metal alloys, these large strain rates are possible due to an underlying bistability in the system: first the stress is held by the actin network, which then yields and gives way to a new stable situation provided by the intermediate filaments. Usually, tissues undergo small-scale deformations and the resulting changes are mainly elastic [256] with a linear relationship between tensional increase and deformation [257, 258]. This allows cells in tissues to return to their default state after the stress is released, a process known as tensional or mechanical homeostasis [259, 260]. Above a certain threshold, however, the bonds between cytoskeletal filaments, cell-cell junctions and cell-matrix adhesions rupture, leading to irreversible deformations that prevent full recovery, even if the associated stress is released [194, 261, 262]. However, with the help of micropatterned elastic substrates, Latorre and colleagues were able to provide an explanation on how certain epithelial tissues can undergo reversible, large-scale elastic deformations in 3D without tissue rupture.

3.2.3 Cell collectives in 3D confining environments

As explained above, cell collectives in 2D often extend into 3D by themselves. However, today one can design assays that include the 3D aspect right from the start, in order to mimic the 3D physiological environment in vivo and to support and monitor collective supracellular growth in all three dimensions. Historically, in vitro pattern formation and higher-ordered supracellular behavior in 3D has been observed already in the early 1980s, in the context of connective tissue. In a reductionist approach, Stopak and Harris mixed fibroblasts and collagen to reconstitute connective tissue [263]. To resist the collagen gel shrinkage induced by the tensile forces from the fibroblasts, they simply attached fix points in form of polystyrene cylinders in the culture dish. Given that the free edges along the collagen-culture liquid interface served as a natural barrier, leaving nothing to attach, the fix points caused the cells to self-organize into aligned tracks along the margin of the collagen, in order to resist the centripetal stress, exerted by central cells. Around 25 years later, Bischofs and colleagues used a similar approach and found that the collective architecture of fibroblasts in collagen resembled the morphology of single fibroblasts on a macroscopic scale, if the boundaries, that is, the subcellular adhesion sites of the single fibroblasts and the anchor points of the hydrogel, are comparable in geometry [264]. In both

cases, the previously described relation of tension and elasticity leads to the observed phenotypes, however the structural architecture arises on different scales. While bundled actin arcs restricted the edges of the single cells, the edges of the collagen hydrogel were defined by polarized cells that aligned perpendicular to the direction of the central stress, resembling the structure of individual actin arcs in the single cells on a supracellular scale. Although being an extreme example, this shows that cell collectives resemble certain biomechanical aspects of single cell morphogenesis, given that the geometric boundaries are predefined.

Today, modern microfabrication techniques like 3D nanoprinting enable researchers to engineer cell culture systems with physical boundaries down to the microscale. Multicellular force generation in such scaffolds can be monitored by state-of-the-art light microscopy in space and time, allowing researchers to perform much more refined assays. To generate 3D microstructures with defined geometry, micro-molding or stenciling techniques have emerged as valuable tools. In principle, the same elastic polymers that are regularly used to fabricate plane 2D substrates can be used to cast desired 3D shapes from a master structure, that is, a positive replica of the desired form. Thus, the structures can be fabricated with different elasticities, optionally from synthetic polymers or from biologically-derived materials like collagen, and can be combined with TFM to estimate the cellular forces [265–267]. Moreover, micro-molding processes are not restricted to soft materials, as components like ceramic powder can also be incorporated in polymerizable materials to fabricate stiff scaffolds to promote for example osteogenic differentiation [268]. However, due to the nature of the casting process, the incorporation of small topographies or fine details in the structure is difficult. Nevertheless, micro-molded 3D structures can be used to monitor tissue growth in a nutshell, and confinement in all three dimensions can be achieved by adding a 'lid' on the micro-molded structure, see Fig. 3.4a,a′) [265].

Mechanobiological research in micro-molded 3D environments is receiving growing attention as advances in volumetric imaging and optical sectioning allow the capture of large 3D stacks with increased axial resolution in a reasonable amount of time. This in turn allows to tackle long-standing basic questions, for example, if and how the mechanisms of collective cellular force generation differ between 2D and 3D setups. However, compared to plane 2D substrates, force calculation and mapping of cellular stresses is much more challenging. Gjorevski and colleagues micro-molded 3D collagen hydrogel structures of different geometries and incorporated fluorescent microspheres for the calculation of tissue stress within epithelia [266]. To account for the heterogeneities in the collagen network, they performed confocal reflectance and atomic force microscopy measurements. Together with computational modelling,

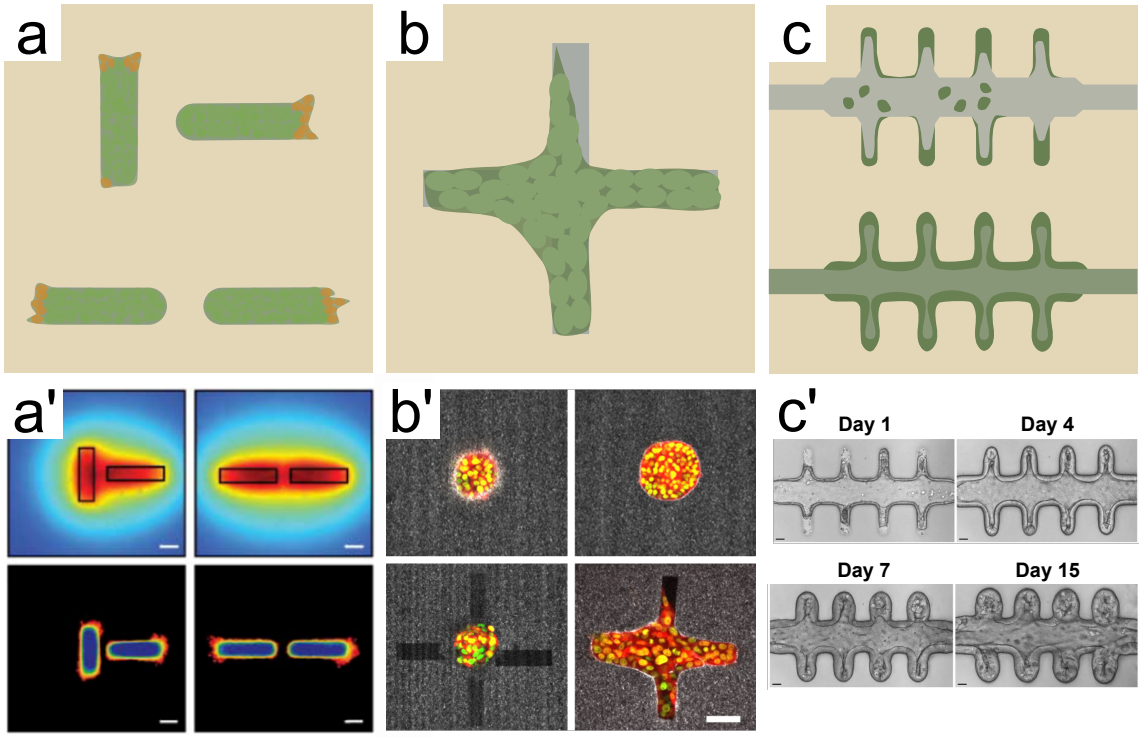

Figure 3.4: **Cell collective experiments in 3D structured environments. a,a′**) Schematics (a) and images (a′) of epithelial cells growing in cavities of collagen gel. **b,b′**) Schematics (b) and images (b′) of mammary tumor breast cancer cells in 3D microtracks of collagen matrices created with two-photon laser ablation. **c,c′**) Schematics (c) and images (c′) of intestinal stem cells in a collagen microchannel generated with laser ablation. a′): Reproduced with permission [265] 2006, AAAS. b′): Reproduced with permission [269], 2011, IOP Publishing. c′): Reproduced with permission [270], 2020, Nature. All other images reproduced with permission [10], 2023, Wiley.

these techniques allowed them to quantify patterns of mechanical stress throughout the surrounding matrix and to observe unexpected geometry-dependent mechanical behavior in curved duct-like tissues. The same approach was used to monitor the stress and pulling forces, exerted during collective cell migration, showing that tensile forces at the invasive front propel the colony forward and condition the cells and matrix for further extension [267].

Besides these basic mechanobiological questions, micro-molded 3D structures are frequently used to monitor biological and cellular output in response to the 3D environment. Similar to plane 2D micropatterns, studies investigating cell proliferation, differentiation and collective cell migration are among the most prominent. Kollmannsberger and colleagues used microscope projection lithography and micromolding to fabricate 3D PDMS scaffolds with macroscopic square-shaped clefts for

the cultivation of microtissues [271]. Using this set-up, they monitored microtissue formation over several weeks and found that especially at the highly tensed growth front, cell proliferation was upregulated and fibroblasts transitioned into myofibroblasts. Thus, predicting tension generation in patterned tissues allowed the correlation of multicellular forces and cell proliferation in 3D, similar to examples described in the 2D set-ups above. Similarly, Nelson and colleagues fabricated surfaces with pyramidal arrays and found that cell proliferation was highest in the grooves, suggesting that the tissue form can feed back to regulate patterns of cell proliferation [110]. Xi and colleagues monitored collective cell migration in 3D microchannels [272]. Their experiments revealed emergent patterns of collective cell migration under tubular confinement: In contrast to flat constraint, cell sheets in smaller microtubes demonstrated slow motion with periodic relaxation, but fast overall movement in large microtubes.

The flexibility of photolithographic and soft-lithographic approaches allows to upscale the dimensions and complexity of the 3D structures, in order to steer multicellular growth on the scale of millimeters. The approach of Xi and colleagues, where cells were crawling through microchannels, was designed to mimic tubulogenesis [272]. Moreover, increasing the complexity of the structures can resolve cellular decision-making processes during tissue growth, for example during vascularization and branching morphogenesis in glands and lung tissue. This was for instance done by monitoring the growth of epithelia in microchannels with different curvatures [273], resembling tissue folding and winding growth processes as they occur in the brain or in the intestine. Nelson and colleagues harvested this approach to control the initial 3D structure of mouse mammary epithelial tubules [265]. By quantifying the extent of branching, they found that the geometry of tubules dictates the position of branches, as they initiated at sites with a local minimum of autocrine inhibitory morphogens, revealing that tissue geometry can control organ morphogenesis by defining the local cellular microenvironment.

Besides these micro-molding approaches, several other creative approaches have been established to investigate the multicellular behavior in complex 3D environments. To monitor collective cell invasion of completely encapsulated cancer spheroids in collagen hydrogels, Ilina and coworkers used an approach that does not rely on the precasting of microstructures, but rather on the generation of micro-tracks via two-photon laser microsurgery after cell seeding and hydrogel polymerization, see Fig. 3.4b,b′) [269]. Using two-photon excitation, regions of interest with variable length, widths and depths can be positioned directly adjacent to the edge of multicellular spheroids. This gives a striking degree of freedom, allowing not only to monitor invasion in real

3D confinement, but also to dynamically adjust the micro-tracks to the desired need. This laser ablation approach was also used to show that E-cadherin dependent cell-cell adhesion and ECM confinement cooperate to determine unjamming transitions and stepwise epithelial fluidization during breast cancer invasion [227]. Nikolaev and colleagues laser-ablated a gut-like 3D structure in a hydrogel, see Fig. 3.4c,c′), and observed epithelium formation and cell-fate patterning in these environments [270].

Another way to increase the complexity of 3D scaffolds for cell cultivation was established by adapting 3D printing approaches towards biomedical research. On the multicellular scale, both bottom-up and top-down approaches are basically established to engineer cell patterning and microtissue formation. Extrusion-based, inkjet-based, and laser-assisted bioprinting are among the most common approaches to spatially deposit cell-laden Bioink in complex 3D forms. Given the extent of this growing area of research, we refer to more comprehensive reviews for further reading [274, 275]. Trushko and colleagues recently developed a different interesting bottom-up approach for mechanobiological applications [276]. Using a 3D printed microfluidics device [277], they produced hollow alginate spheres with encapsulated epithelial cells in the center and Matrigel coating on the inner surface of the spheres. Upon reaching confluency in the monolayer grown on the inner side of the sphere, confinement leads to the local detachment from the Matrigel and folding of the sheet towards the sphere center [276]. Considering the apparent pressure required to buckle together with a continuum theoretical approach, the authors established a minimal system to monitor stress-induced epithelial folding and conclude from these experiments that both capsule stiffness and cell stiffness have to be high in order to relax excess cell proliferation by buckling.

In principle, such approaches can be refined down to the microscale by combining different techniques and additive manufacturing. As described above, 3D nanoprinting techniques allow the fabrication of 3D structures in the regime of single microns. Additionally, an increasing palette of available biocompatible photoresists with protein-adsorbing or protein-repellent features and tunable stiffness ranges can be used to fabricate sophisticated scaffolds with complex geometry and topography landscapes [82, 278]. Published results in recent years show the biocompatibility of 3D printed micro-scaffolds with various cell types and populations under different conditions. For example, micro-scaffolds have been adapted to monitor and guide neurite outgrowth [279, 280], microglia cultivation [281], or glioma cell colonization [282]. Complex woodpile scaffolds were used to monitor cell invasion through narrow spaces in response to growth factors [283]. The recent and rapid improvements in 3D nanofabrication, for example the development of faster printing techniques [284, 285],

will allow the fabrication of large-scale composite scaffolds for studies on microtissues in the near future.

3.3 Organoids

One of the most exciting developments in modern biology are organoids, which are 3D cell assemblies that differentiate and grow in the test tube and thereby develop organ-/tissue-specific features [74, 286]. They are closely related to stem cell technology, because fate induction is typically achieved in induced pluripotent stem cells (iPSCs). To date, a wide range of organoid types from different cellular origins has been developed. This includes not only basic embryonic spheroids resembling early developmental stages, like blastuloids, gastruloids or epithelial organoids, but also spheroids derived from adult stem cells that resemble specific organ types or sub-organ regions, such as intestinal organoids, retinal organoids or cerebral organoids. These features make organoids an attractive choice for basic biomedical research, for example for in vitro drug testing on patient derived material or for the investigation of organ development processes in a simplified system. In the long-term, organoids might bear the potential to overcome some of the long-standing problems in regenerative medicine, as they in principle allow the differentiation of organs-in-a-dish from patient-derived stem cells. However, major weaknesses of the organoid technology thus far are the lack of reproducibility and their heterogeneity in terms of ill-defined sizes, morphologies, patterning, cell type composition and differentiation efficiency, thus limiting their current application in clinical research.

The induction of organoids, that is, the activation of distinct fate programs in stem cells, requires not only the addition of certain biochemical factors, but also, at least equally as important, the embedding of the cells in a 3D matrix, typically in cell-derived matrices like Matrigel^{TM}. Due to the natural origin of these products, their biomolecular composition often varies significantly between different lot numbers and charges, leading to the above-mentioned heterogeneities. Moreover, the self-organizing capacities of the organoids are limited, meaning that autonomous growth, folding and differentiation processes only occur up to a certain degree, possibly because certain cues that exist in a physiological context are missing.

To narrow the gap between self-organizing organ development in vivo and organoid growth in vitro, microfabrication approaches that allow the generation of defined 3D synthetic cell niches offer exciting possibilities. One of the best-studied and most suitable examples in this regard are intestinal organoids. In vivo, the architecture of the small intestine can be subdivided into the functional units of villi and crypts, with

the latter harboring a reservoir of intestinal stem cells, see Fig. 3.5a-d). Gjorevski and colleagues recapitulated this architecture in microscaffolds to improve the structure and reproducibility of intestinal organoids [84]. In contrast to the randomized spatial induction of crypt domains under conventional culture conditions (Figure 8b), cultivation in 3D microstructures instructed the precise cellular self-organization into crypt and villus domains, respectively, see Fig. 3.5c-e). Another approach used a collagen-based scaffold and achieved similar results [57], showing that indeed the 3D architecture of the scaffold is important to drive self-organization of intestinal organoids/enteroids. Nikolaev and colleagues went one step further and bioengineered intestinal stem cells via scaffold-guided organoid morphogenesis into tube-shaped epithelia with an accessible lumen that was connected to a microfluidic system, see Fig. 3.4c,c′) [270].

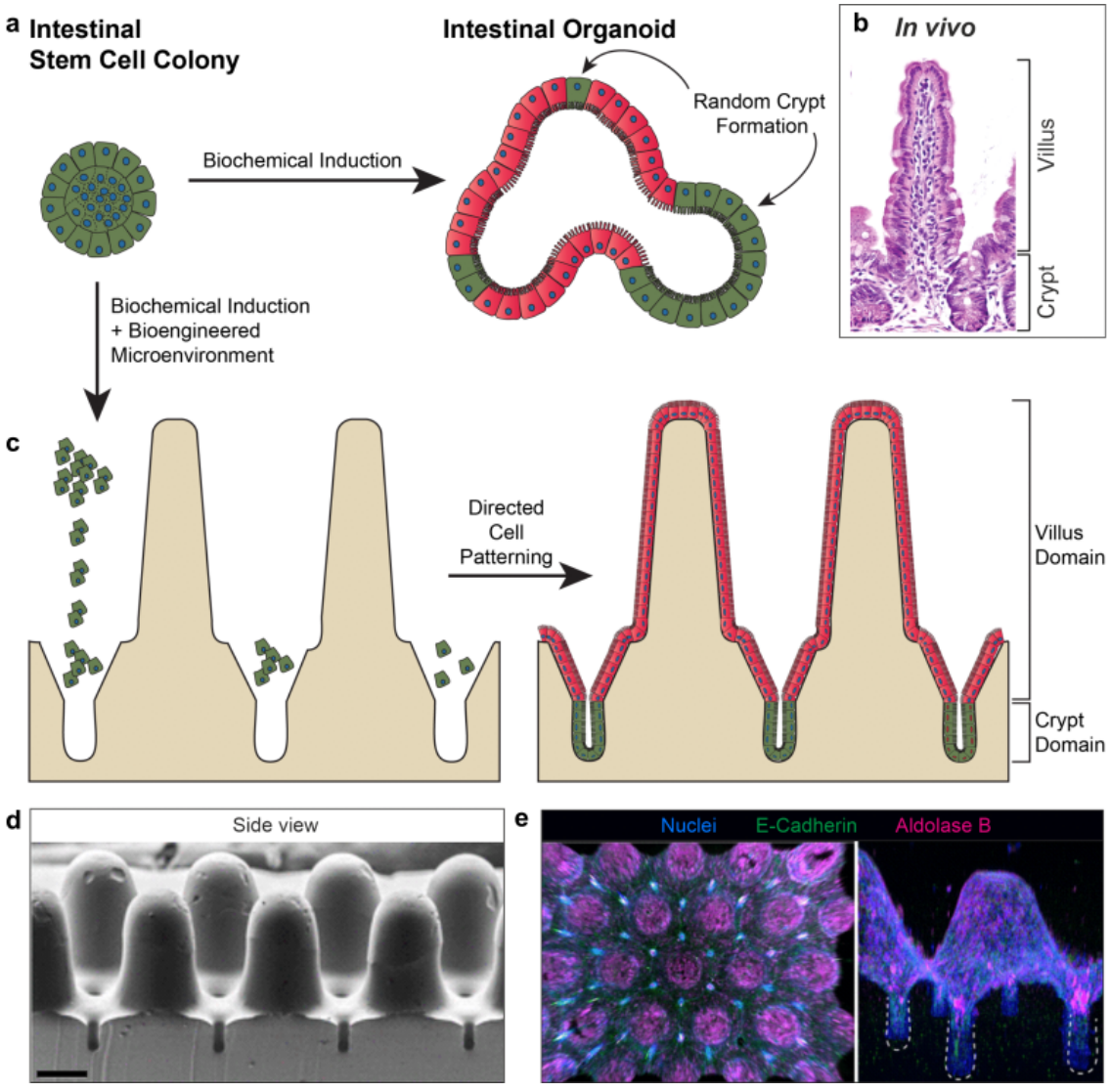

Figure 3.5: **Self-organized versus directed growth of organoids.** **a**) Self-organized intestinal organoids can be derived through biochemical differentiation from isolated crypts or intestinal stem cells, but suffer from heterogeneities in size, morphology, and cellular composition. Crypt domains harbor the stem cells in intestinal organoids (marked in green) but form at random positions. **b**) Immunohistochemical staining of the in vivo intestinal epithelium, showing the hierarchic architecture of villus- and crypt domains. **c**) Recapitulating the in vivo architecture of intestinal epithelia in biomimetic 3D scaffolds directs patterning of the different cellular domains. When seeding dispersed intestinal stem cells onto the scaffolds, they self-organize into villus- and crypt-like domains in response to the scaffold architecture. **d**) Scanning electron micrograph of a biomimetic 3D scaffold, recapitulating villus- and crypt domain architecture. **e**) Immunofluorescent staining of the same scaffolds after cellular colonization. 48 hours after cell seeding, intestinal stem cells established a confluent monolayer. Induction of differentiation resulted in stereotyped organoid patterning. Aldolase-B (magenta) marks enterocytes and other differentiated intestinal cell types in the villus-domain, E-Cadherin (green) marks stem cells in the crypt domains.
b): Reproduced with permission [287], 2013, Elsevier. d) and e): Reproduced with permission [84], 2022, AAAS. All other images reproduced with permission [10], 2023, Wiley.

While the scaffold allows guiding organoid morphology towards an in vivo-like architecture, the perfusion system allows the continuous removal of metabolites and cellular debris, prolonging the microtissue lifespan to several weeks. This concept comprises another step towards functional organoids-on-a-chip.

Microfabricated scaffolds were also used to decipher the biomolecular mechanisms behind these morphogenetic processes. Using micro-molding and photopatterning, it was shown that the geometry-driven cell patterning in intestinal organoids arises from local differences in cell crowding that guide the downstream activity of the mechanosensitive transcriptional co-activator YAP [84]. Regions of high curvature lead to increased cell crowding and YAP remains inactive in the cytoplasm, leading to the upregulation of intestinal stem cell markers. In less narrow and flat regions, YAP is imported into the nucleus and promotes intestinal stem cell differentiation into absorptive cells of the villus-like domain. In traditional organoid culture, this process acts stochastically and leads to random crypt formation in regions where curvature is generated by differential actomyosin contractility and luminal pressure [288, 289]. Again, soft elastic substrates helped define the force distribution during these processes, unveiling how patterned forces enable compartmentalization, folding and collective migration in the intestinal epithelium. Pérez-González and colleagues mapped 3D force distribution in mouse intestinal organoids, showing that the crypt

shape relies on cell surface tension and cortical actomyosin density. Cells of the villus-like domains are subsequently dragged out of the crypt along a gradient of increasing tension [290].

In addition to investigating morphogenetic features of intestinal organoids on micropatterned 2D and 3D substrates, a range of different approaches start to control the formation of various organoid and organotypic tissues by tuning the respective culture substrates. Numerous developmental processes that lead to the formation of stratified and layered tissues rely on the reciprocal transduction of mechanical signals between the cells and the ECM [291] and thus bear the potential to be manipulated or guided by microengineering approaches. Furthermore, the above-described knowledge might be included in future research and combined with larger-scale biofabrication and bioprinting approaches, for example, to guide the vascularization of growing organoids and to recapitulate complex architectures of vascular beds in biomimetic scaffolds [292–294]. Current materials and microfabrication approaches steadily increase our ability to mimic complex shapes and furthermore start to improve scaffolds for long-term cell cultivation, for example by including dynamic dimensions like perfusion systems or controlled release of molecules [295]. Blatchley and colleagues recently provided a comprehensive review of various techniques for spatiotemporal regulation of organoids, including top-down methods such as extracellular matrices, bottom-up approaches such as confined environments to position single cells, and middle-out engineering, which utilizes external stimuli such as optogenetics to modulate both scaffold properties and cell behavior in time [296].

3.4 Discussion

Cell culture is one of the most important achievements of the life sciences and allows us to perform systematic and quantitative experiments outside living organisms. The beginnings of in vitro cell culture were characterized by attempts to specify and improve cellular culture conditions via the use of chemical compounds, including growth factors, hormones, and cytokines. Customized culture media formulations were established that activate biochemical signal cascades promoting proliferation, differentiation or simply survival of specific cell types. They were complemented by standardization through cell lines, which usually are transformed cells that can proliferate without limits. Despite these advances in quantification and standardization, it remained challenging to cultivate distinct cellular populations in the absence of their natural growth environment.

Three decades ago, this situation changed dramatically with the advent of mechanobi-

ology, which demonstrated that physical aspects of the extracellular environment (in particular stiffness, geometry, and topography) play an equally important role for cellular decision making as biochemical factors do. Maybe the most decisive factor for this development was the transfer of new methods from materials science into cell biology and biophysics: starting with PDMS-technology, microcontact printing and photolithography, it has become customary to prepare mechanically and geometrically defined environments for cell culture. Biologists collaborated with physicists, chemists, material scientists and engineers in order to develop sophisticated cell culture platforms by microfabrication, for example by DLW of cell culture scaffolds in three dimensions. These experimental developments were complemented by advances in quantitative imaging processing and modeling. First applied to single cells, these tools are now increasingly applied to cell collectives, from cell monolayers to 3D spheroids and organoids.

Thanks to these interdisciplinary approaches, we are now in the exciting position to take the next step. As the field has grown from single cells towards multicellular systems, future studies should aim to merge the knowledge from biochemistry, molecular biology, and biophysics to control cellular growth and behavior in vitro. The emergence of organoid technology is a prime example in this regard. As described above, fate induction in organoids is first established biochemically, while scaffolds with tuned elasticity and microtopography later help guide the growing spheroids into structured tissues with a function. Future studies in this direction are expected and bear the potential to take another step towards organs-in-a-dish. One interesting direction is the transition from 2D to 3D culture systems. More refined methods in microfabrication and molecular biology allow us to tackle the recreation of multilayered and stratified tissues in 3D, for example of an artificial retina. Mathematical models might help to accelerate this process and to suggest interesting designs, thus avoiding delays or dead ends in experimentation. The contribution of materials science does not need to be confined to spatial and mechanical aspects, but also could cover the time domain. Stimuli-responsive materials and optogenetics can be used to implement temporal protocols to guide cell development or even to implement feedback loops that automatically adjust the physical properties of the environment to the current state of the biological system. Bringing together these different technologies opens up numerous exciting and very promising new avenues for the control of cells, tissues, and organs.

4 Modeling cells in structured environments*

4.1 Modeling single cells

Cells are complex systems that rely on a large number of molecular pathways and cellular components to govern their behavior. Capturing all the relevant interactions and feedback loops in one model is a difficult task. Small-scale models focus on the interactions of amino acids, which are the building blocks of proteins, in full atomic detail. These proteins are the fundamental building blocks of cells by forming larger structures and interacting with each other. Molecular dynamics simulations are used to predict protein structures and dynamics or model dynamic processes, however the typical length- and timescale simulated with molecular dynamics is up to the µm and µs scale [297].

However, cellular processes occur at multiple spatial and temporal scales, ranging from molecular interactions within cells to cell-cell communication and tissue-level behaviors. Describing these processes can only be achieved with coarse grained models. In such cases, cells are can be approximated as isotropic viscoelastic materials, as contractile networks or by describing their surface.

Cell models can be categorized as static or dynamic. Static models describe the steady state or average behavior of cells. They do not consider changes over time or the dynamics of cellular processes. Static single cell models are computationally less demanding and typically used when temporal changes are minimal in an experiment. In contrast, dynamic single-cell models capture the temporal dynamics of cellular processes over time. They consider the changes in cellular behavior and molecular interactions as the cell responds to stimuli, undergoes differentiation, or transitions between different states. These models often incorporate differential equations or stochastic simulations to represent the time-dependent changes in cellular components

*This chapter is based on the review Link, R., Weißenbruch, K., Tanaka, M., Bastmeyer, M., & Schwarz, U. S. (2023). Cell Shape and Forces in Elastic and Structured Environments: From Single Cells to Organoids. *Advanced Functional Materials*, 2302145. https://doi.org/10.1002/ADFM.202302145 [10].
In detail, we use Section 2, specifically 2.3, and 2.5, Section 3, specifically 3.4, Section 4, all with further elaboration.

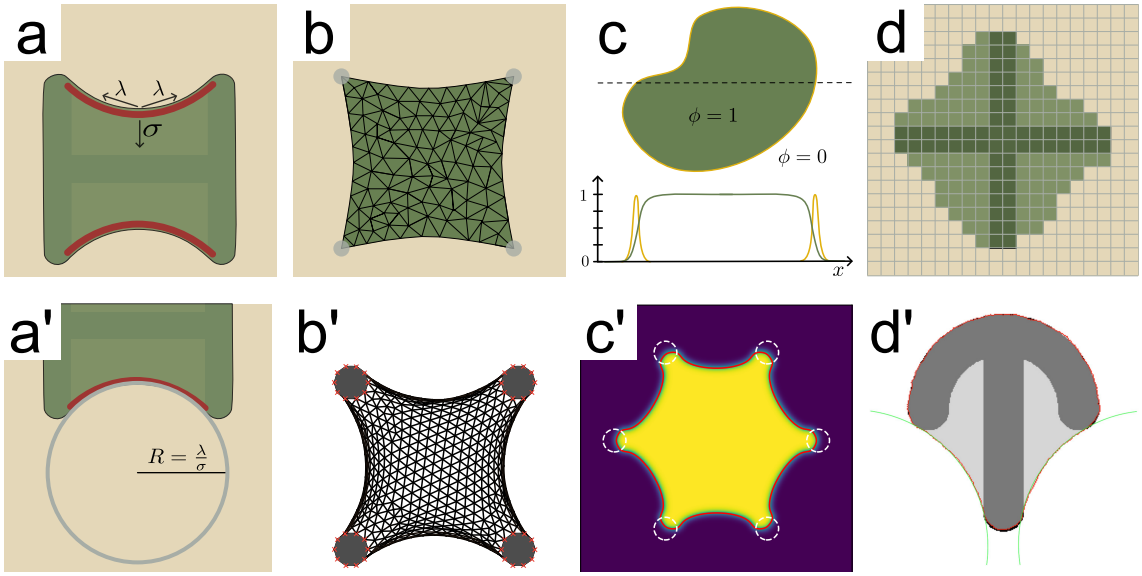

Figure 4.1: **Models to describe cells in environments in 2D. a,a′**) Schematics of the contour model which predicts the radii of invaginated arcs from surface tension σ and line tension λ. **b,b′**) Schematics (b) and image of a simulation (b′) of a 2D network model. **c,c′**) Schematics (c) and image of a simulation (c′) of a 2D phase field model. **d,d′**) Schematics (d) and image of a simulation (d′) of a 2D cellular Potts model.
d′): Reproduced with permission [19], 2014, Elsevier. All other images reproduced with permission [10], 2023, Wiley.

such as ATP cycles. Dynamic single-cell models are well-suited for investigating time-varying behaviors such as cell shape changes and cellular responses to perturbations.

In the following, we will explore the different approaches to model single cells in structured environments, with a special emphasis on how the cell-environment interaction is implemented. In addition, we will discuss how these models can be used to develop and parametrize mathematical models, which in the future are expected to become more predictive regarding optimal design [298].

4.1.1 Modeling single cells in 2D

Modeling single cells in 2D reduces the computational complexity and simplifies the modeling process. Many cellular processes, such as adhesion, migration, and signaling occur at the cell surface. These interactions can be studied with a 2D model. Additionally, experimental data often generates 2D data, which can be directly compared to 2D model predictions. Shape and forces of single cells have been modeled in 2D with a variety of different methods, including static contour models, network models, and continuum models as well as dynamic models such as phase field models and the CPM [298–300].

Contour models describe the static boundaries of a sessile cell based on the idea that non-motile cells on substrates are effectively two-dimensional and span their contours between focal adhesions, see Fig. 4.1a,a′). They are motivated by experiments with cells in structured environments, which often show strong geometrical features, compare Fig. 3.1a). The simplest approach is to assume a constant surface tension σ, due to the contracting actomyosin cortex, and a constant line tension λ, arising from actin stress fibers lining the periphery and counteracting the cortical tension. The surface tension energy is thus given by $E_A = \sigma \int \mathrm{d}A$ and the energy from the line tension by $E_L = \lambda \int \mathrm{d}L$. Assuming the system is in equilibrium, the energy must be in a minimum, and thus $\mathrm{d}E = 0$. This leads to the Laplace law for soap bubbles, which can be used to describe cells boundary on adhesive structures:

$$\begin{aligned} \sigma\,\mathrm{d}A &= \lambda\,\mathrm{d}L \\ \sigma\,\mathrm{d}(\pi R^2) &= \lambda\,\mathrm{d}(2\pi R) \\ \sigma 2\pi R\,\mathrm{d}R &= \lambda 2\pi\,\mathrm{d}R \\ R &= \frac{\lambda}{\sigma} \end{aligned} \tag{4.1}$$

The surface tension acts in normal direction of the cell boundary while the line tension is parallel to the boundary. R describes the radius of invaginated arcs between adhesive points [301]. This simple argument suggests a constant invagination radius. Experimentally, a linear relation between radius and spanning distance of invaginated arcs was found. This can be explained with the introduction of an additional elastic line tension [264] or with a dynamical version of the interplay between tension and elasticity [151]. Recently, elliptical arcs have been described for the case when the stress fibers do not line the periphery, but pull towards the cell body [302]. Contour models can often be solved analytically and the dependance of input parameters on the solution as well as their biological meaning follow directly from the model. For example, they have been used to predict cell forces from shape [301]. However, they have been devised mainly to describe cell shape on 2D adhesive micropatterns and cannot be easily generalized to different situations. Contour models describe the static shape a cell reaches in equilibrium, but cannot describe dynamics. Moreover, they use phenomenological effective model parameters such as surface and line tensions.

Network models describe cells as a 2D network of cables, thereby replacing the coarse-grained surface tension in contour models with a more detailed model that is directly motivated by the key physical properties of the actin cytoskeleton, see Fig.4.1b,b'). The actin filament bundles are approximated as mechanical links joined

at discrete nodes, which represent cross-linkers. Adhesion to the micropatterns is modeled by fixing the respective nodes. Actin filaments are semiflexible polymers which can be stretched but not compressed. In fact actin filaments buckle under compression [33]. The mechanical force between nodes is therefore described as an elastic force when the filament is stretched and no force when the filament is compressed. The spring constant of actin bundles is given by EA/L_0, where E is the Young's modulus, A the cross section and L_0 the rest length of the actin filament. Due to the motor activity, an additional active force is introduced, which is proportional to the rest length L_0 of the link, and the force density per length T arising from the molecular motors is assumed to be constant. As this would lead to a finite active force for length $L = 0$, a small length scale L_C is introduced below which the force decays linearly, such that the total force disappears for $L = 0$. Thus we can describe the force between two nodes i, j:

$$\vec{F}_{ij} = \begin{cases} (TL_0 + EAu_{ij})\vec{e}_{ij} & \text{if } L_0 < L_{ij} \\ TL_0\vec{e}_{ij} & \text{if } L_C \leq L_{ij} \leq L_0 \\ TL_0\frac{L_{ij}}{L_C}\vec{e}_{ij} & \text{if } L_{ij} < L_C, \end{cases} \tag{4.2}$$

where $u_{ij} = (L_{ij} - L_0)/L_0$ is the strain of the actin fiber and $\vec{e}_{ij}$ is the unit vector along the link.

Actively contractile cable networks under isometric tension reproduce the experimentally observed invaginated arcs, independent of the architecture of the cable network, revealing a fundamental and unconventional property of the contractile actin cytoskeleton [303]. Therefore, network models allow for the modeling of experimentally more complex situations, such as cells on micropatterns that are contracting due to optogenetic activation [80]. Recently, cable networks have been used to describe the effect of laser cutting stress fibers that are strongly connected to the actomyosin cortex [126]. Network models are well suited to predict force distributions of single cells on micropatterns. While the explicit network architecture is not relevant for the simulations, network models are limited by the fact that the connections cannot change throughout the simulation, but cytoskeleton remodeling is often observed in experiment, for example during cell migration.

Following more traditional approaches from continuum mechanics, homogeneous 2D (visco-)elastic sheets under tension can also be used to model cells in 2D [137, 304, 305]. These models describe single cells as thin contractile layers with intracellular stress $\sigma_{ij} = \sigma_{ij,\mathrm{p}} + \sigma_{ij,\mathrm{a}}$, which has a passive contribution $\sigma_{ij,\mathrm{p}}$ due to the cell deformation, and an active stress $\sigma_{ij,\mathrm{a}}$ arising from actomyosin contraction, similar

to active gel theory [306]. The passive contribution can be modeled for example with a Kelvin-Voigt model as a linear viscoelastic solid: $\sigma_{ij,\mathrm{p}} = (1 + \tau_c \partial_t)(\lambda \epsilon_{kk} \delta_{ij} + 2\mu \epsilon_{ij})$, where the strain tension is given by $\epsilon_{ij} = (\partial_i u_j + \partial_j u_i)/2$ with displacement field u_i and Lamé parameters λ and μ, and the relaxation constant $\tau_c = \eta_c / E_c$ depends on effective viscosity η_c and Young's modulus E_c. The force balance is then given by

$$\partial_j \sigma_{ij}(x,t) = Y(x) u_i(x,t), \tag{4.3}$$

where $Y(x)$ describes the substrate geometry and stiffness as a spring constant density. Adhesion to the substrate can also be modeled with a fixed boundary condition representing sites of adhesion to compliant material. Finite element simulations can then be used to predict, for example, traction forces and stress distribution inside the cell [307]. Continuum models are useful to understand how processes at the boundaries propagate into cells and to predict cell forces on the scale of the whole cell.

In many situations of interest, a more dynamical description than that provided by continuum mechanics models is desired, especially in the case of large deformations or even topology changes. Phase field models [308, 309] use an energy-based description in contrast to the previous models, which are force-based. Energy-based models are better suited to describe and predict dynamics but make it difficult to model forces. In phase field models, an auxiliary field $\phi(x, y, t)$ is used to represent the boundary of a cell, as $\phi = 1$ represents the inside of the cell, and $\phi = 0$ the outside, see Fig.4.1 c,c′). There is a smooth transition between the interior and exterior phases and the dynamics of ϕ are described by an overdamped equation of motion. Single cell migration can then be modeled through an energy functional with an additional polarization vector or velocity field to model cell motility [308, 310].

A computationally very efficient alternative to phase field models is the CPM, which was initially devised to model cell collectives [16, 21, 311–313]. Like phase field models, the CPM is an energy-based description of cells on a lattice, see Fig.4.1d,d′). A generalized cell represents a biological cell, a subcellular compartment, the surrounding medium, or other physical entities and can span over more than one pixel on the lattice. For 2D systems, the Hamiltonian typically consists of an elastic area constraint and interaction energies between neighboring pixels that belong to different generalized cells [314]. In the context of cells on micropatterns, an alternative approach is the use of energy terms of area and line tension, combined with an energy gain for the occupation of predefined adhesive sites [19, 313]. In this case, area is not determined by the area constraint, but by the size of the adhesive area, reflecting the fact that cells in 2D can generate area by material transfer from

3D to 2D. In any version of the CPM, a modified Metropolis algorithm is used to find the energy minimum, making this approach essentially a Monte Carlo simulation. This is a very versatile approach that can be applied to model complex systems. However, some parameters used in cellular Potts type simulations do not have a direct biological interpretation. We will discuss the CPM in detail at the end of this chapter.

4.1.2 Modeling single cells in 3D

3D computer simulations have increasingly helped to deepen our understanding of single cell mechanobiology in structured environments. 3D models represent the spatial context in which cells live more accurately, especially the interaction with the ECM. Additionally, mechanical forces such as tension, compression, and shear, as well as cell shape changes can be described in a 3D model.

Many 2D simulation methods can be extended to three dimensions. For example, the shape of single cells 3D-printed scaffolds was described with a network model of active cables by Brand and colleagues, see Fig. 4.2a,a′) [152]. The total energy is minimized numerically for a shape connecting the given adhesion platforms. Brand and colleagues reported good agreement between the experimentally observed shape of a NIH 3T3 fibroblast and found the same curvature radius to spanning distance dependence as in the 2D contour model, although no explicit line tension was included. This suggests that the stress fibers lining the invaginations in 2D are condensed versions of the actin cortex which is folding back onto itself in 3D.

Continuum models can be extended to three dimensions as well and often are implemented with the finite element method (FEM) [315]. Stiffness and viscosity of single cells or subcellular compartments can be measured and directly used as parameters in the simulations. Finite element models such as Cytopede [316] have been used to describe crawling fibroblast and keratocyte motility [317]. In addition to cell migration, 3D finite element modeling can be used to predict cellular responses of nanoindentation [289] and to calculate the force distributions within cells [318, 319]. The open-source software Virtual Cell uses finite volume solvers to describe actin polymerization inside a 3D cell with a predefined geometry [320]. Cytosim is an open-source software that can describe the mechanics of cytoskeletal networks using Brownian dynamics of fibers and motors [321]. More coarse-grained models describe the formation of pseudopodia of a 3D cell on an 2D substrate with a finite element model [316, 322] or as an active nematic droplet [323].

Winkler and colleagues described single cells in 3D mechanical environments with an extended phase field model, see Fig. 4.2b,b′) [324]. Both the cell and the

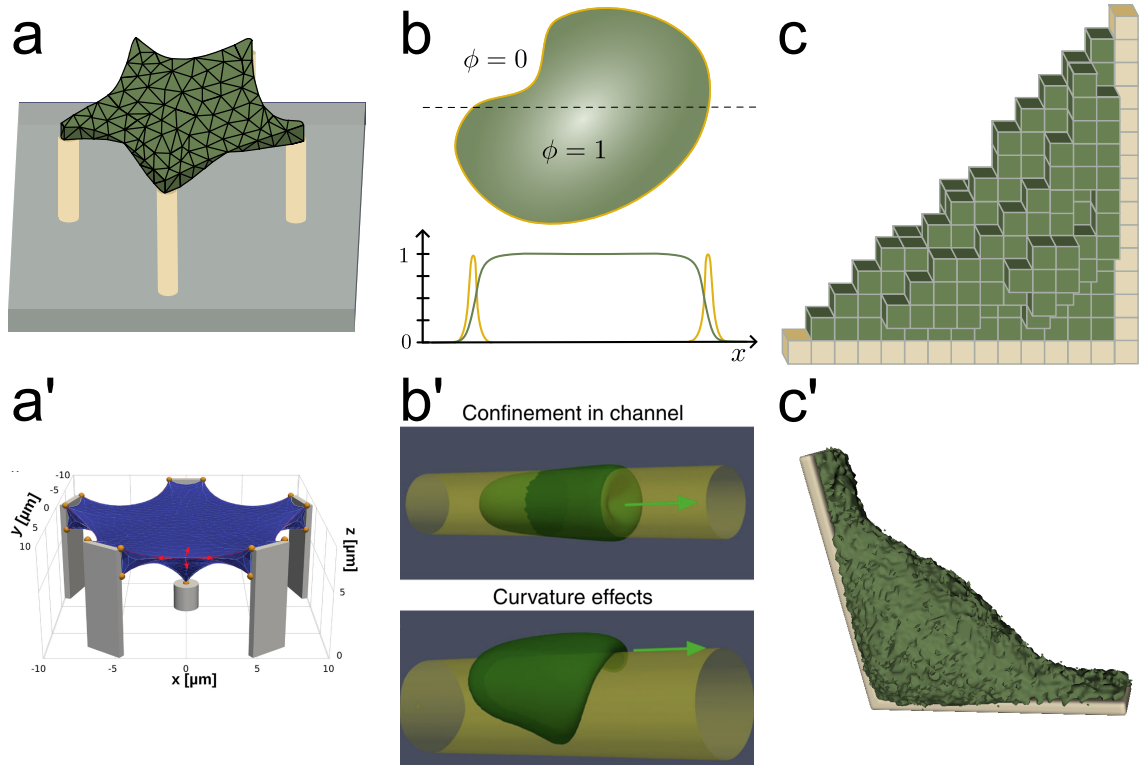

Figure 4.2: **3D models to describe single cells in environments.** **a,a′**) Schematics (a) and image from the network model simulation (a′) of a single cell in a 3D structure. **b,b′**) Schematics (b) and image (b′) of a 3D phase field simulation. **c,c′**) Schematics (c) and image (c′) of a single cell in a 3D CPM simulation.
a'): Reproduced with permission [152], 2017, Elsevier. b'): Reproduced with permission [324], 2019, Nature. All other images reproduced with permission [10], 2023, Wiley.

mechanical environment are described with a scalar 3D field, while the actin inside the cell field is described with a vector field. The actin distribution inside the cell is modeled via a source term modeling actin polymerization close to the boundary, a sink term, and a diffusive term. Symmetry-breaking leads to front-read polarity and cell movement. This method predicts cell shape, velocity, and alignment on arbitrarily shaped substrates.

Extending the CPM to 3D is straight-forward, see Fig. 4.2c,c′). Typically, the Hamiltonian includes an area constraint and a volume constraint, in addition to the interaction energies between neighboring generalized cells. Moreover, the nucleus can be implemented as a sub-cellular compartment with higher stiffness than the cytosol. Scianna and colleagues investigated the influence of a fibrous environment on a single cell with an explicit nucleus representation and compared cell velocity and persistence length for increasingly aligned fibrous networks and different pore

sizes [20]. More recently, single cell motion was described with the CPM by explicitly modeling lamellipodia of mesenchymal cells [325] or by coupling the actin dynamics inside the cell to its shape and external cues [32].

The aim of many in silico experiments is to better understand cell migration in 3D [326]. Predicting the 3D shape of a single cell in structured environments with the goal of improving scaffold design for biomedical applications is a novel research avenue and so far has only been discussed in 2D [298].

4.2 Modeling cell collectives

Cells in collectives exhibit complex behavior such as collective migration and pattern formation that in principle could result from relatively simple rules being followed by the single cells. Thus, these are ideal model systems to be studied by mathematical and especially by computational models. As we have seen in Chapter 3, epithelial tissue is characterized by cell coordination over large length and time scales, resulting from mechanosensitive interaction between cells via cadherin-mediated adhesions [327]. The strong cohesion in these systems means that modelling can proceed either by individual-based or continuum models. In individual-based models, cells are described by single or multiple particles, either in a continuous space or on a lattice. Cell activity resulting in motion can then be introduced by self-propulsion, like for active Brownian particles. Cell sheets can also be approximated as continuum elastic or fluid materials. In this case, cell activity resulting in motion is often modeled by active stresses, which typically arise from actomyosin contractility.

Cell-cell interactions can easily be implemented in the CPM by including interaction energies between cells in the Hamiltonian. With the introduction of two cell types and the definition of pair-wise interaction energies, see Fig. 4.3a,a′), the differential adhesion hypothesis (DAH) [328] was implemented numerically in 2D as the first application of the cellular Potts model [329]. Soon, it was extended to 3D and coupled with partial differential equations to describe chemotaxis, which allowed the modeling of the formation and crawling of Dictyostelium discoideum [21]. This model has been adapted and extended by Merks and colleagues to describe vasculogenesis, where cell elongation was described explicitly with an additional energy contribution [330]. More recent 2D simulations based on the cellular Potts framework focus on describing both single and collective cell dynamics [298, 331]. Due to its versatility, the CPM can be extended to 3D and applied to more complex systems, such as reproducing the morphology of vascular tumors, their growth and angiogenesis [332].

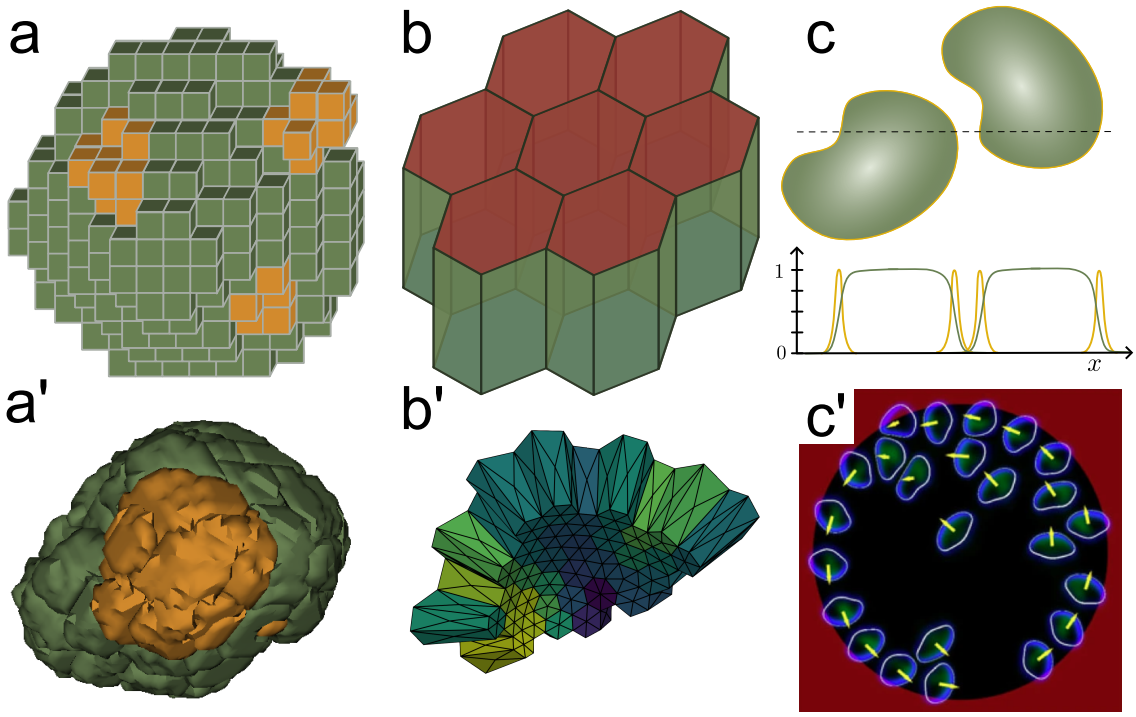

Figure 4.3: **Models to describe cell collectives in structured environments.** **a,a′**) Schematics (a) and image (a′) of a 3D CPM describes cell sorting, a process where cell types arrange according to the difference in their adhesion strength. **b,b′**) Schematics (b) and image (b′) of a vertex model, describing tightly packed monolayers. **c,c′**) Schematics (c) and image (c′) of a phase field model simulation of interacting cells on a adhesive micropattern.
c′): Reproduced with permission [333], 2015, Nature. All other images reproduced with permission [10], 2023, Wiley.

In contrast to the CPM, which uses very variable cell shapes, the 2D vertex model uses simple polygons to describe epithelial monolayers [334]. The forces acting on the vertices can result either from phenomenological force descriptions or from an energy formulation as in the CPM. Using the purely geometrical Voronoi tessellation, which divides space into cellular compartments based on the neighborhood relations to their centers, one also can use a formulation for the midpoints of the polygons, which makes the system similar to individual-based models. Typical terms for the energy function include elastic constraints on volume and area of the polygons, as well as an interaction term for neighboring polygons proportional to the length of the boundary interface [335]. In 3D, one uses polyeders rather than polygons, see Fig. 4.3b,b′). One of the first applications of the 3D vertex model was a simulation of the Drosophila wing disk, which showed that the tension in the system was sufficient for the formation of the dorsal appendages of Drosophila eggshells [336]. The ensemble behaviour of vertex models can be approximated with a continuous mean field theory. Czajkowski and colleagues developed a hydrodynamic model that

takes cell shape anisotropy, motility, and polarization into account to model pattern formation in embryonic development [337].

The phase field model can also be used to describe cell collectives. In one of the first formulations of multicellular systems with the phase field model, each cell is modeled by a separate phase field, see Fig. 4.3c,c′), and the phenomenological free energy of the system includes terms for the individual cell shape, the interaction of the cell with the substrate and with other cells [338]. Löber and colleagues coupled the scalar phase field to a vector field describing the orientation of actin fibers inside the cell to model cell collisions [333]. A different approach is to model a cell sheet as a single phase field. By adding elastic forces to the phase field equation, Chojowski and colleagues describe a reversible elastic phase field that captures deformations due to contractility and finger formation [339].

4.3 Modeling organoids

Organoids are complex and interacting cell systems and combining them with structured environments is a promising novel approach. Again, mathematical and computational models can help better understand how emergent properties arise from cell interactions and to test hypotheses and make predictions. To account for the complexity of cellular systems, simulations of organoids often include both biomechanical properties as well as signalling pathways [340]. The optic cup formation of retina organoids was successfully described with a vertex model that includes cell growth and division, intercellular signalling and cell shape deformations [341]. These simulations suggest that mechanical feedback is important for formation of the optic cup [342]. In addition, the vertex model was combined with a Turing model for activation and inhibition to describe undulation, tubulation and branching [343]. Cerruti and colleagues used a CPM approach to simulate lumen formation in epithelial cysts, suggesting that accumulation of multiple lumens correlates with fast cell division rates [344].

While there are successful models of organoid morphogenesis [342, 345] and growth [346], these models are typically not yet including interactions with the extracellular environment. A first approach to include the local microenvironment in the mathematical model describes Matrigel as a semi-flexible elastic polymer network which gives rise to a bending rigidity of the organoid surface. The polymer network can be remodeled by the cells attached to it and the local curvature of the organoid surface partially regulates cell specification. This model describes intestinal spatiotemporal organization and growth [347, 348]. A continuum approach was used

to better understand the oxygen transport and consumption in human midbrain organoids. Oxygen levels of an organoid in laminar flow were modeled with a reaction-diffusion model describing the oxygen diffusion in the local microenvironment as well as diffusion and consumption in the organoid [349].

In summary, theoretical approaches can complement experimental studies and help to better understand the complex interplay between different aspects of cellular systems. Once established, they might also guide the design of future experimental systems and applications.

4.4 Introduction to the cellular Potts model

With different modeling approaches for cells presented in the previous sections, we now focus on the CPM, which is the model we use throughout this thesis. The CPM is an energy-based model that inherits its framework from statistical physics. Is is used to simulate the shape and behavior of biological cells and tissues. In this model, generalized cells are represented on a lattice, where each lattice site with the same index belongs to the same cell or non-cellular material. The model also considers internal cell states for each cell, which are defined as the properties of the cell that influence its behavior and interactions with other cells.

Many ideas used in CPM type simulations directly come from statistical physics, specifically the Ising and Potts models [314]. The Ising model is one of the most important models of statistical physics, and has been invented to explain the second order phase transition in ferromagnetic materials for dimensions larger than two. It describes spins on a lattice with orientations up or down ($\sigma = \pm 1$), which obey Boltzmann statistics and interact with their nearest neighbors. In the absence of external magnetic field, the Ising Hamiltonian is given by the sum of interactions between nearest neighbor spins

$$\mathcal{H}_{\text{Ising}} = -\frac{J}{2} \sum_{(\vec{i},\vec{j}) \text{ neighbors}} \sigma(\vec{i})\sigma(\vec{j}), \tag{4.4}$$

where aligned spins lower the total energy by $-J$, while anti-aligned spins add the energy J to the system. The factor $\frac{1}{2}$ prevents double-counting. The idea of an energy penalty per unit length of boundary is used in both the Ising model and its generalization to the CPM.

A direct generalization of the Ising model is the Potts model, where each lattice site has one of q states [314]. Following the idea of the Ising model, the Hamiltonian is determined by neighbor interactions, the total energy of the system is obtained by

summing over neighbors, and if neighbors are not in the same state the energy is increased by J:

$$\mathcal{H}_{\text{Potts}} = J \sum_{(\vec{i},\vec{j})\ \text{neighbors}} \left(1 - \delta(\sigma(\vec{i})\sigma(\vec{j}))\right), \tag{4.5}$$

where δ is the Konecker-Delta, which equals one if $\sigma(\vec{i}) = \sigma(\vec{j})$ and zero otherwise. The Potts model is also used to study phase transitions as it can model systems with multiple domains at low temperature.

The CPM is a further generalization and modification of these ideas [314]. It introduces uniquely labeled domains σ and allows evolution only at the interfaces. The use of type-dependent boundary energies allows for the modeling of complex dynamics, such as cell sorting [16, 329]. The CPM can incorporate auxiliary fields, such as chemical gradients, the ECM or gravity, to represent external forces that affect the behavior of the cells. An effective energy or Hamiltonian $\mathcal{H}$ is defined to encapsulate the interactions between the model elements, which can include potential energies, elastic constraints, and other factors. The Hamiltonian can also include PDEs and boundary conditions for the time evolution of fields. Additional mechanisms, such as cell division, can also be included in the model to capture the dynamics of cell growth and proliferation. Typically, sub-cellular processes are modeled phenomenologically, and the interaction between different mechanisms is expressed is terms of the Hamiltonian.

The first CPM described cell sorting in 2D. To describe this process, the Hamiltonian included interaction energies and volume constraints between cells σ with cell types τ:

$$\begin{aligned}\mathcal{H}_{\text{CPM}} = &\sum_{(\vec{i},\vec{j})\ \text{neighbors}} J(\tau(\sigma(\vec{i})), \tau(\sigma(\vec{j}))) \cdot \left(1 - \delta(\sigma(\vec{i}), \sigma(\vec{j}))\right) \\ &+ \sum_{\sigma} \lambda_{\text{V}}(\tau) \left(v(\sigma) - V_{\text{T}}(\tau(\sigma))\right)^2\end{aligned} \tag{4.6}$$

Here, J depends on the cell types τ of the neighboring domains $\sigma(\vec{i})$ and $\sigma(\vec{j})$. Following the Potts model Hamiltonian, see Eq. 4.5, the interaction energy J is nonzero only if the neighboring lattice sites belong to different domains. The additional volume constraints ensures that domain sizes are close to a predetermined target volume V_{T}, which depends on the cell type τ. The strength of this constraint λ_{V} depends on the cell type τ as well.

A modified metropolis algorithm is used to evolve the system [314, 350]. A voxel at the boundary between generalized cells is chosen randomly and flipped to a randomly

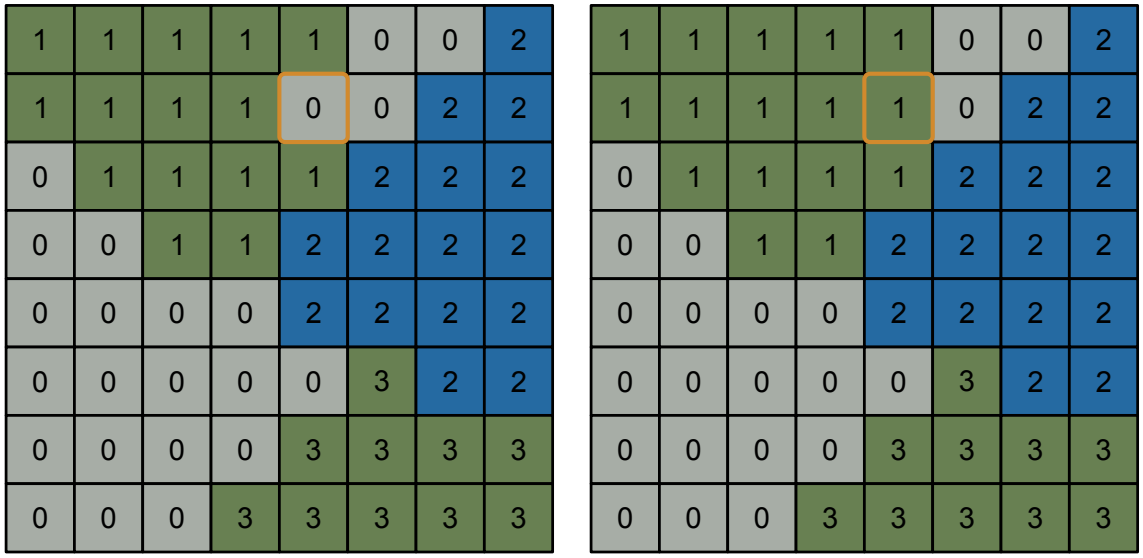

Figure 4.4: **Schematics of the spin-flip in the CPM.** Left: 2D CPM simulation with three cell indices $\sigma = 1, 2, 3$, outside medium $\sigma = 0$ and two cell types τ, represented by green and blue coloring. A voxel at the boundary of a generalized cell is chosen randomly (marked in orange). Right: The index of the randomly chosen voxel is changed to one of the neighboring indices. The energy change due to the changed index $\Delta\mathcal{H}$ is used to calculate the probability to accept the new index, see Eq. 4.7.

chosen cell index σ of a neighboring cell as a test, see Fig. 4.4. The energy change $\Delta\mathcal{H}$ due to this flip is calculated, and the changed cell index is kept with probability p

$$p = \begin{cases} 1 & \text{if } \Delta\mathcal{H} < 0 \\ \mathrm{e}^{-\Delta\mathcal{H}/T} & \text{if } \Delta\mathcal{H} > 0. \end{cases} \tag{4.7}$$

This ensures that the system evolves towards the minimum energy configuration while it allows the crossing of local energy maxima by accepting spin flips into higher energy states with the Boltzmann probability. Note that the modified Hamiltonian used in the CPM breaks detailed balance, as cells can disappear when their volume becomes 0, but new cells cannot appear randomly. At the same time, the metropolis algorithm allows for the description of dynamics in the simulation. At $T = 0$, the metropolis algorithm is no longer statistical and deterministically drives the configuration towards a local energy minimum. At low temperatures, it introduces a pseudo-time because it only allows for local changes that tend to lower the total energy of the system, while the Boltzmann probability (Eq. 4.7) ensures that the system is able to evolve across local energy minima [314].

To describe the kinetics of the system evolving with a modified metropolis algorithm, we consider configurations $\vec{S}_1, \vec{S}_2, ...$ that differ in one spin value, and every spin

flip lowers the total energy of the system, such that $\mathcal{H}_1 > \mathcal{H}_2 > ....$ If the energy difference between configurations with one differing spin value are small compared to the simulation temperature T, we can describe the net transition rate of the system as

$$\begin{aligned} r(\vec{S}_i \to \vec{S}_{i+1}) = p(\vec{S}_i \to \vec{S}_{i+1}) - p(\vec{S}_{i+1} \to \vec{S}_i) = 1 - \exp\left(\frac{-\mathcal{H}_i + \mathcal{H}_{i+1}}{T}\right) \\ \approx \frac{-\mathcal{H}_i + \mathcal{H}_{i+1}}{T} + \mathcal{O}\left((\frac{-\mathcal{H}_i + \mathcal{H}_{i+1}}{T})^2\right). \end{aligned} \tag{4.8}$$

Thus, the transition rate r is approximately linearly proportional to the energy change in the system after a spin flip. From this, we can describe the velocity of the system as

$$\vec{v}(\vec{S}_i \to \vec{S}_{i+1}) = \frac{\vec{\nabla}\mathcal{H}(\vec{S}_{i+1} - \vec{S}_i)}{T}, \tag{4.9}$$

where we define the unit time step as one spin-copy and the position variable of the gradient is the length of one pixel (in 2D) or voxel (in 3D). Now we see that the CPM dynamics obeys an overdamped force-velocity relation

$$\vec{\nabla}\mathcal{H} = \vec{F} = \mu\vec{v} \tag{4.10}$$

with effective mobility $\mu = T$. Due to their microscopic internal structures, biological cells exhibit a high level of dissipation, making them primarily influenced by viscosity rather than inertia. As a result, the impact of external forces on cells can be most accurately described within the Aristotelian regime, where the force is proportional to the velocity, $\vec{F} \sim \vec{v}$. In conclusion, if we ensure that $\frac{\Delta\mathcal{H}}{T}$ is small, we can describe the viscous dynamics of a biological system with the modified metropolis algorithm.

When comparing the CPM to the Ising model, we find several noteworthy differences [314]. One of the main differences between the Ising model and the CPM lies in their initial conditions. In the Ising model, the initial conditions are typically chosen randomly, whereas in the CPM, the initial conditions are often biologically motivated. This means that the initial configuration of the system is based on real biological observations, rather than being completely arbitrary. In many cases, the final configuration or the dynamics depend on the initial conditions, therefore choosing initial conditions that represent biological systems is crucial. Adding to this is the fact that the CPM incorporates biologically motivated domain properties, such as the fact that cells remain connected. In contrast, the Ising model assumes that each spin interacts only with its nearest neighbors and does not incorporate any

domain-specific knowledge. Furthermore, the Ising model assumes a single contact energy between spin values, while the CPM can incorporate more complex energy terms that reflect the physical properties of the system being studied. This allows the CPM to capture more nuanced interactions and behaviors within the system. Another significant difference is that the Ising model has no external control over domain size or shape, they are the outcome of the simulation for given T and J, whereas the CPM can be used to model the growth and shape of cells, tissues, and other biological structures due to additional energy terms describing perimeter, area or volume energies. Finally, the standard Ising model has no dynamics, whereas the CPM can be used to model the movement and behavior of cells over time. This makes the CPM particularly useful for studying dynamic biological processes, such as cell shape changes, migration and tissue development.

4.4.1 Modeling cell shape with the CPM

We focus on cell shape in this work, and to model cell shape successfully, we implement the effects of different intracellular structures described in Chapter 2 as energy terms of the CPM Hamiltonian.

We model the effect of the actin cortex with an area energy constraint of the cell. This constraint is often chosen to be elastic [351–353],

$$\mathcal{H}_{\text{cortex}} = \lambda_{\text{A}}(A - A_T)^2, \tag{4.11}$$

where λ_{A} is the strength of the constraint, A is the surface area and A_T is a predefined target area. Others have argued that extending the cell surface area always costs energy [298, 313], thus describing the effect of the contractile actin cortex with a linear area constraint

$$\mathcal{H}_{\text{cortex}} = \lambda_{\text{A}} A, \tag{4.12}$$

where λ_{A} is again the strength of the constraint and A the cell surface area. We will analyze the resulting differences in cell shape for the two approaches to describe the contractile nature of the actin cortex in the frame of the CPM in Chapter 6.

Additionally, we implement stress fibers in the 3D CPM in Chapter 5 by compartmentalizing the cytoplasm of the cell and introducing line tensions between the center of mass of neighboring compartments. Stress fibers can then be initiated by introducing line tensions between points of adhesion on a micropattern. This approach ensures that the cell shape changes due to varying line tensions. The

contribution of stress fibers to the cell shape in the form of a line tension is given by

$$\mathcal{H}_{\text{stress fibers}} = \sum_{\text{SF}} \lambda_\ell \ell, \tag{4.13}$$

which is the sum over all stress fibers, λ_ℓ is the strength of the stress fiber energy and ℓ is the length of the stress fiber segment.

In cellular Potts type simulations, the nucleus has been implemented as a cellular compartment, and its higher stiffness can be described by increasing the energy constraint parameters. Preciosi and colleagues used a compartmenalized CPM to describe cells with nuclei in structured environments in 3D [20, 351].

Following this idea, we implement the nucleus as a compartment with volume and surface constraints in the simulations of cells in structured environments throughout this work. This approach allows us to additionally prescribe the interaction energies between the nucleus and other generalized cell types in the CPM. Additionally, we impose the position of the nucleus with an elastic energy constraint between the center of mass of the cell and the nucleus:

$$\mathcal{H}_{\text{nucleus position}} = \lambda_{\text{C}}(\vec{X}_{\text{cell}} - \vec{X}_{\text{nucleus}})^2, \tag{4.14}$$

where λ_{C} is the strength of the constraint, $\vec{X}_{\text{cell}}$ is the center of mass of the cell cluster, consisting of the generalized cell types nucleus and cytoplasm, and $\vec{X}_{\text{nucleus}}$ is the center of mass of the nucleus.

In the CPM used throughout this work, we describe the binding of the cell to adhesive surfaces such as the ECM and fibronectin with a negative interaction energy. This parameter influences how far cells can spread on adhesive areas, as it counteracts the energy cost due to the surface area increase.

4.4.2 Simulating cell shape with CompuCell3D[†]

There are several open source simulation frameworks for 3D cellular Potts type simulations[355–357]. We chose CompuCell3D (CC3D) [355] for our simulations, as it is actively maintained and developed, while being modular and fully customizable at the same time. In the following, we describe the CC3D architecture and the custom extensions that were needed to model single cells and organoids in structured environments.

[†]A step-by-step guide on modeling cell shape can be found in Link, R. & Schwarz, U. S. (2023) Simulating 3D Cell Shape with the Cellular Potts Model. In: Zaidel-Bar, R. (eds) *Mechanobiology. Methods in Molecular Biology*, vol 2600. Humana, New York, NY. https://doi.org/10.1007/978-1-0716-2851-5_22 [354].

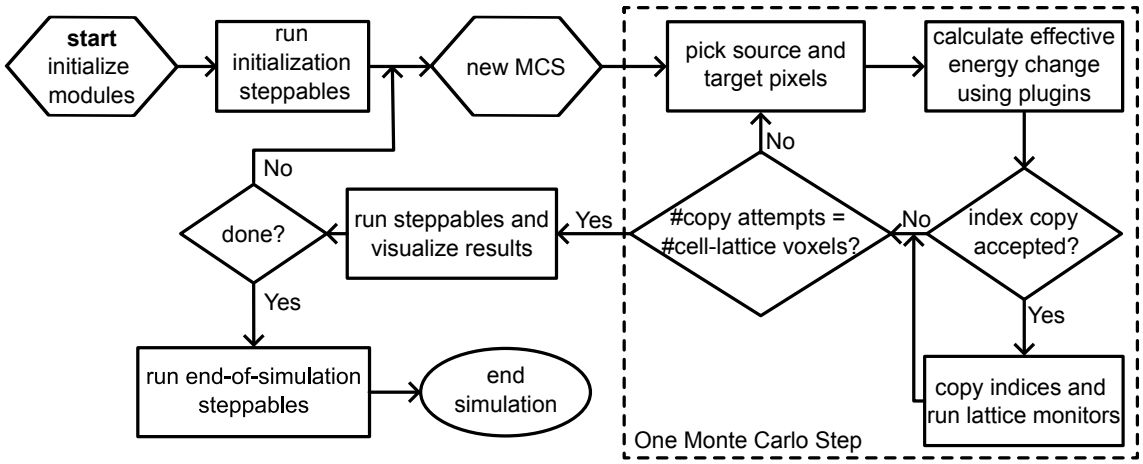

Figure 4.5: **Flow chart of the CC3D algorithm.** Reproduced from [358].

The simulation contains a list of objects, which are generalized cells or fields. Generalized cells represent cells, subcellular compartments or other materials. They occupy one or more voxels and have a unique cell index σ, as well as a cell type τ. Each generalized cell has a list of attributes, including the type, volume, surface area and center of mass.

The simulation dynamics is governed by rules for cell behavior and interactions, which are specified in plugins and steppables. Plugins are called at every voxel copy attempt to calculate energy changes due to changed voxel indices or after index changes to monitor the lattice. Steppables are called before the first Monte Carlo step (MCS) to load initial conditions or after a predefined number of MCS to change parameters and to save results. Plugins are typically written in C++ as they are called for each index copy attempt, while steppables are written in Python to allow for an easy simulation set-up and flexibility. In Fig. 4.5, the architecture of the CC3D algorithm is depicted.

To describe single cells with nucleus in structured environments, we use the following plugins: The *CellType* plugin is used to define the cell types *Medium*, *Cytoplasm*, *Nucleus*, *Adhesive* and *NonAdhesive*. To implement the elastic volume constraint, we use the *Volume* plugin, where we can specify the constraint strength λ_V and the target volume V_T for each cell type. Similarly, we use the implemented elastic area constraints *Surface* and *ClusterSurface*, for which we specify the constraint strength λ_A and target area A_T for the nucleus and the cell respectively. Finally, we prescribe interaction energies with the *Contact* and *ContactInternal* plugins.

Clusters add an additional index to each cell. Several cells can have the same cluster index. While the traditional CPM enables subcellular modeling with partial differential equations and ordinary differential equations, the use of compartmental-

ized clusters allows for the explicit modeling of subcellular units such as filopodia, apical and basal membranes and the nucleus. We use clusters to describe cells which consist of two compartments, the *Nucleus* and the *Cytoplasm*, which are both generalized cell types. Combining them to a cluster is necessary to properly describe their cell surface, as opposed to the cytoplasm surface.

The elastic constraints calculate the resulting change in energy for each voxel copy attempt. For the cell that gains one voxel due to the proposed copy attempt, the volume constraint energy changes by

$$\begin{aligned}\Delta E_{\mathrm{V}}^{+} &= E_{\mathrm{after}} - E_{\mathrm{before}} \\ &= \lambda_{\mathrm{V}}(V + 1 - V_{\mathrm{T}})^2 - \lambda_{\mathrm{V}}(V - V_{\mathrm{T}})^2 = \lambda_{\mathrm{V}}(1 + 2(V - V_{\mathrm{T}})),\end{aligned} \tag{4.15}$$

and similar if the cell loses one voxel due the copy attempt:

$$\Delta E_{\mathrm{V}}^{-} = \lambda_{\mathrm{V}}(1 - 2(V - V_{\mathrm{T}})). \tag{4.16}$$

For the elastic area constraint for cells and clusters, the energy change is given by

$$\begin{aligned}\Delta E_{\mathrm{A}}^{+} &= E_{\mathrm{after}} - E_{\mathrm{before}} \\ &= \lambda_{\mathrm{A}}(A + 1 - A_{\mathrm{T}})^2 - \lambda_{\mathrm{A}}(A - A_{\mathrm{T}})^2 = \lambda_{\mathrm{A}}(1 + 2(A - A_{\mathrm{T}})),\end{aligned} \tag{4.17}$$

if the cell or cluster gains a voxel due to the proposed area change, if it looses a voxel the energy change is given by

$$\Delta E_{\mathrm{A}}^{-} = \lambda_{\mathrm{A}}(1 - 2(A - A_{\mathrm{T}})). \tag{4.18}$$

Furthermore, the interaction energy change ΔE_J due to the voxel copy attempt is calculated for all voxels in the neighborhood area, and the total energy change $\Delta E = \Delta E_{\mathrm{V}} + \Delta E_{\mathrm{A}} + \Delta E_J$ is used to calculate the probability p to accept or reject the voxel copy attempt, see Eq. 4.7.

In Chapter 6, we compare cell shapes in 3D scaffolds simulated with either elastic or linear area energies. To implement the linear area energy functions in CC3D, we developed the plugins *SurfaceLinear* and *ClusterSurfaceLinear*. In this case, the energy change when the area is increased due to attempted voxel changes is given by

$$\Delta E_{\mathrm{A}}^{+} = E_{\mathrm{after}} - E_{\mathrm{before}} = \lambda_{\mathrm{A}}(A + 1) - \lambda_{\mathrm{A}}(A) = \lambda_{\mathrm{A}}, \tag{4.19}$$

and if the cell surface area is reduced due to the proposed voxel change the energy

change is given by

$$\Delta E_{\mathrm{A}}^{-} = -\lambda_{\mathrm{A}}. \tag{4.20}$$

In Chapter 7, we compare the influence of matrigel on vesicle formation in organoids with increased pressure on the cell cluster. In this case, we need an elastic volume constraint, similar to Eq. 4.15 and Eq. 4.16, on the cluster. The pressure p is then given by

$$p = -\frac{\partial \mathcal{H}}{\partial V} = 2\lambda_{\mathrm{V}}(V_{\mathrm{T}} - V), \tag{4.21}$$

where the volume V, target volume V_{T} and elastic constraint strength λ_{V} depend on the cluster, not on the cell type. We can then increase the pressure on the system by increasing λ_{V}. This was implemented in the CC3D with the custom-build *ClusterVolume* plugin.

5 Modeling cell shape on micropatterned surfaces

A commonly used approach to manipulate the internal organization of cells and investigate the influence of mechanical cues on cell behavior is the use of adhesive micropatterned surfaces. We previously summarized experimental findings from single cells on micropatterns in Section 3.1.2, and modeling efforts in Section 4.1.1, demonstrating the feasibility of predicting and describing the shape of cells on these surfaces in 2D. However, these models were limited to 2D projections rather than the full 3D shape and did not consider the nucleus in the simulation or enforce a fixed cell area during the simulation, with the argument that cell area can be added or removed from the third dimension, which is consequently not described in these models. To overcome these limitations, we use a 3D CPM to simulate the shape and spreading dynamics of cells on micropatterned substrates. This allows us not only to predict the 3D cell shapes over time but also to investigate the influence of the nucleus on shape and spreading dynamics of the single cell.

5.1 Influence of the nucleus on cell shape and spreading

CC3D is used to calculate interaction energies between the generalized cell types *Cytoplasm*, *Nucleus*, *Adhesive* and *NonAdhesive*, while elastic constraints are employed to model the volumes of the cytoplasm and the nucleus and the surface area of the nucleus and the cell. Cells are modeled as clusters, with compartments *Cytoplasm* and *Nucleus*. The generalized cell types *Adhesive* and *NonAdhesive* are used to model the micropattern geometry and are therefore kept fixed during simulations. Cell adhesion to the micropattern then happens because of the different interaction energies between the *Cytoplasm* and the *Adhesive*/*NonAdhesive* gerenalized cell types.

The Hamiltonian used in this section is therefore given by

$$\begin{aligned}\mathcal{H}_{\mathrm{CPM}} = &\sum_{(\vec{i},\vec{j})\ \text{neighbors}} J^{\mathrm{int}}(\tau(\sigma(\vec{i})),\tau(\sigma(\vec{j}))) \cdot \Big(1-\delta(\sigma(\vec{i}),\sigma(\vec{j}))\Big) \cdot \delta(\alpha(\vec{i}),\alpha(\vec{j})) \\ &+ \sum_{(\vec{i},\vec{j})\ \text{neighbors}} J^{\mathrm{ext}}(\tau(\sigma(\vec{i})),\tau(\sigma(\vec{j}))) \cdot \Big(1-\delta(\sigma(\vec{i}),\sigma(\vec{j}))\Big) \cdot \Big(1-\delta(\alpha(\vec{i}),\alpha(\vec{j}))\Big) \\ &+ \sum_{\sigma} \lambda_{\mathrm{V}}(\tau(\sigma))\,(v(\sigma)-V_{\mathrm{T}}(\tau(\sigma))^2 + \sum_{\sigma} \lambda_{\mathrm{A}}(\tau(\sigma))\,(a(\sigma)-A_{\mathrm{T}}(\tau(\sigma))^2 \\ &+ \sum_{\alpha} \lambda_A(\alpha)(a(\alpha)-A_{\mathrm{T}}(\alpha))^2 + \lambda_{\mathrm{C}}(\vec{X}_{\mathrm{cell}}-\vec{X}_{\mathrm{nucleus}})^2. \end{aligned} \tag{5.1}$$

The introduction of clusters enables the use of different interaction energies J^{int} and J^{ext} depending not only on the cell types but also on the cluster indices of neighboring voxels. The first two sums in Eq. 5.1 describe internal and external interaction energies between different cell types. Additionally, we use volume constraints for the generalized cell types cytosol and nucleus and an area constraint for the nucleus. The cytosol does not have an area constraint, instead we constrain the cluster area $a(\alpha)$ as to avoid counting the internal boundary between cytosol and nucleus. The use of area constraints gives us more flexibility for the interaction energy J, as it becomes possible to assign negative interaction energies [359]. Finally, we introduce an elastic centering constraint with strength λ_{C}, keeping the center of mass of the nucleus $\vec{X}_{\mathrm{nucleus}}$ close to the center of mass of the cell $\vec{X}_{\mathrm{cell}}$.

To investigate the role of the nucleus during cell spreading, we modify our simulation to exclude the nucleus compartment and compare the cell shapes and the time until the final position is reached for simulations with and without explicit representation of the nucleus. This simplifies the Hamiltonian used in our simulations:

$$\begin{aligned}\mathcal{H}_{\mathrm{CPM}} = &\sum_{(\vec{i},\vec{j})\ \text{neighbors}} J(\tau(\sigma(\vec{i})),\tau(\sigma(\vec{j}))) \cdot \Big(1-\delta(\sigma(\vec{i}),\sigma(\vec{j}))\Big) \\ &+ \sum_{\sigma} \lambda_{\mathrm{V}}(\tau(\sigma))\,(v(\sigma)-V_{\mathrm{T}}(\tau(\sigma))^2 + \sum_{\sigma} \lambda_{\mathrm{A}}(\tau(\sigma))\,(a(\sigma)-A_{\mathrm{T}}(\tau(\sigma))^2 \end{aligned} \tag{5.2}$$

Here, we describe the cell as homogeneous, and consequently we do not introduce clusters in this simulation. Then, we only need one type of interaction energies, and elastic volume and area constraints are used again.

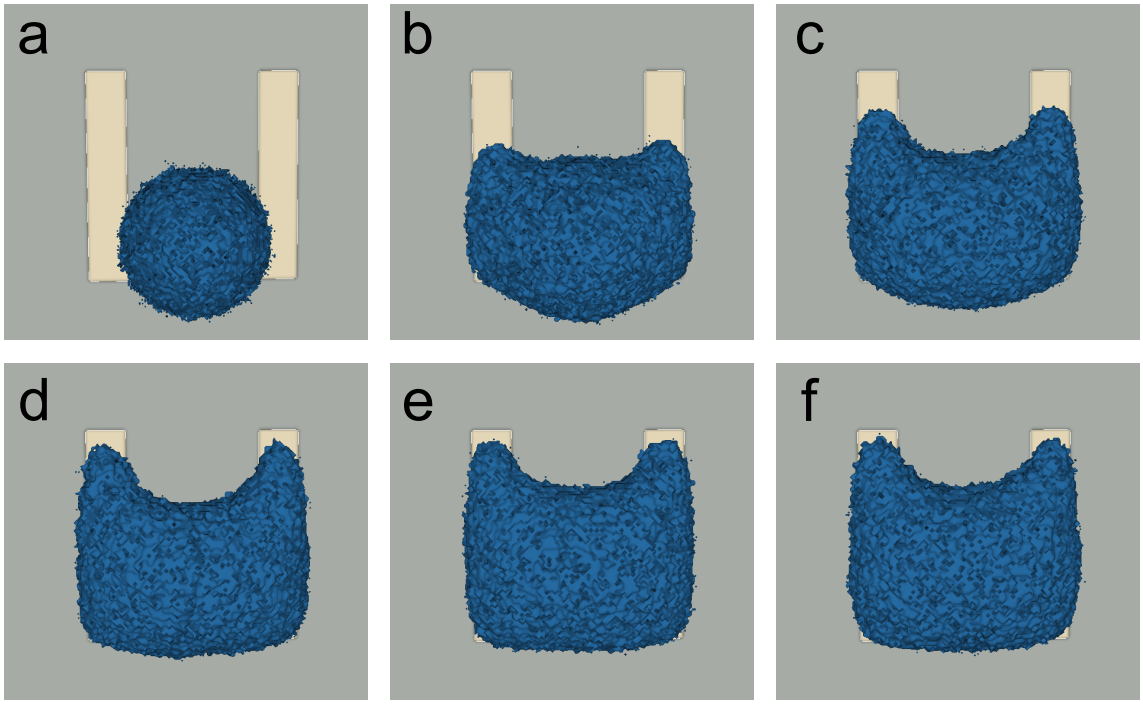

Figure 5.1: **Snapshots from the simulation of a single 3D cell with nucleus on a U-shaped micropattern.** The adhesive area is depicted in beige, the non-adhesive area in gray, and the cell in blue. **a**) MCS = 0, **b**) MCS = 100, **c**) MCS = 250, **d**) MCS = 500, **e**) MCS = 1000, **f**) MCS = 2000. All parameters used in the simulation can be found in Table A.1.

5.1.1 Simulated cell shapes on micropatterns

Adhesive micropattern geometries for cell culture are designed to control and manipulate the spatial arrangement of cells on a substrate. These geometries influence cell behavior, shape, and interactions. Originally, circular adhesive spots of different sizes were used [50]. Today, there is a wide range of micropattern geometries that are used for different purposes [5, 51, 124, 305, 360], for example H-shaped micropatterns are used to immobilize cells [124], crossbow shapes which lead to polarization and increased force generation [5] or squares which even lead to rotation in adhered cell doublets [361]. Many micropatterns provide an adhesive surface for cells to adhere to completely. In contrast, other micropattern geometries such as the tripod or the arrow provide only adhesive lines for cells to adhere to, forcing them to cross substrate areas without adhesive sites. This typically leads to invaginated arcs, as explained in Section 4.1.1.

We are interested in the morphological behavior of cells as they spread across non-adhesive regions, leading to the formation of invaginated arcs. To investigate this phenomenon, we specifically selected three distinct micropattern shapes: the U-shape the V-shape and the crossbow-shape. Cells on U-shaped and V-shaped micropatterns

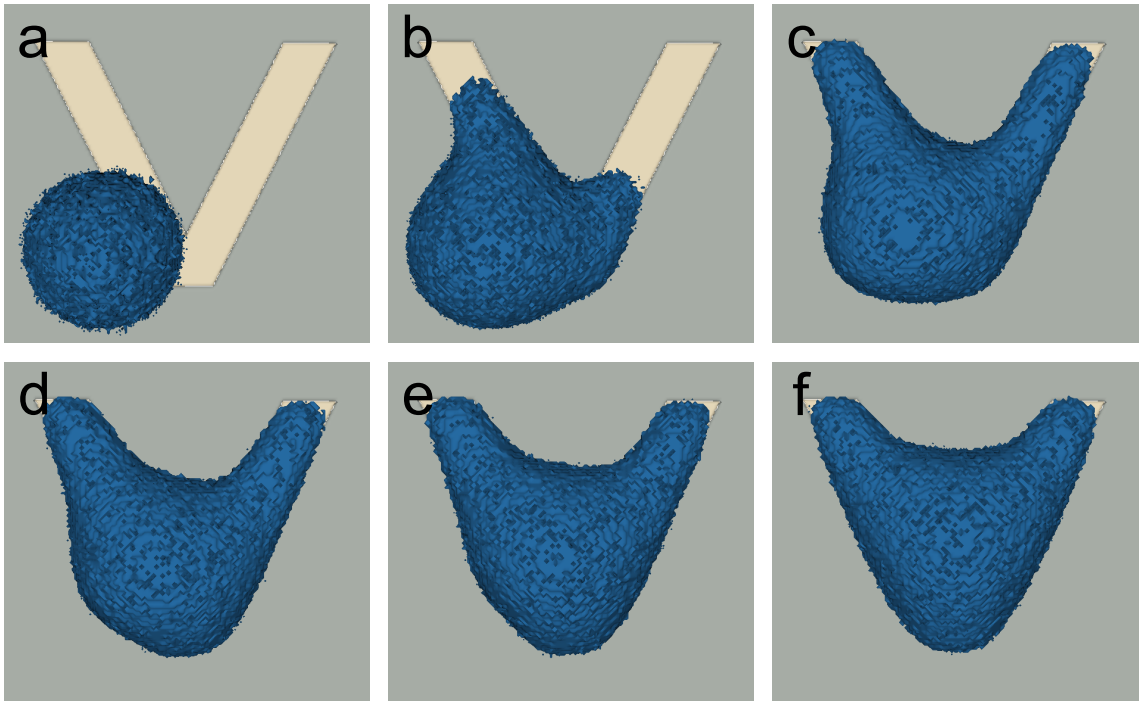

Figure 5.2: **Snapshots from the simulation of a single 3D cell with nucleus on a V-shaped micropattern.** The adhesive area is depicted in beige, the non-adhesive area in gray, and the cell in blue. **a**) MCS = 0, **b**) MCS = 100, **c**) MCS = 250, **d**) MCS = 500, **e**) MCS = 1000, **f**) MCS = 2000. All parameters used in the simulation can be found in Table A.1.

form one invaginated arc. Notably, cells cultured on U-shaped micropatterns adopt a more square-shaped configuration, whereas those on V-shaped micropatterns exhibit triangular shapes, with limited space for the nucleus at the structure's center due to the close proximity of adhesive bars. Cells on crossbow-shaped micropatterns become polarized due to the asymmetric micropattern geometry and form two invaginated arcs.

We initialize the simulation by placing a compartmentalized cell with *Nucleus* and *Cytoplasm* as a cluster on U-shaped, V-shaped and crossbow-shaped micropatterns, see Fig. 5.1a), Fig. 5.2a), Fig. 5.3a). The initial position of the compartmentalized cell is chosen randomly. The *Cytoplasm* is initialized as a half-sphere and we include the *Nucleus* as a sphere at the center of mass of the cell.

For the U-shaped micropattern, we find invaginated arcs between the two parallel adhesive bars, and find that the simulated cell placed symmetrically on the U-shaped micropattern spreads evenly along the bars, see Fig. 5.1. The final shape is minimizing the total energy of the system, where the surface area constraint is rounding up the cell because the cluster surface area is larger than the cluster target surface area and thus counteracting the negative interaction energy between cytosol and adhesive

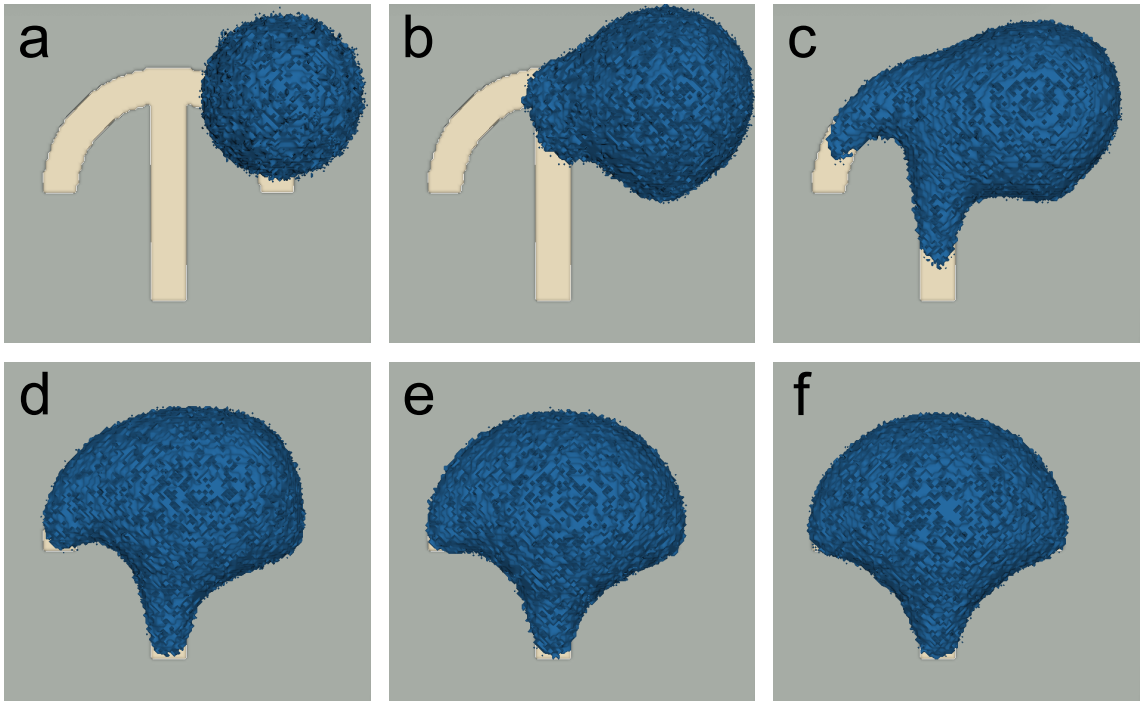

Figure 5.3: **Snapshots from the simulation of a single 3D cell with nucleus on a crossbow-shaped micropattern.** The adhesive area is depicted in beige, the non-adhesive area in gray, and the cell in blue. **a**) MCS = 0, **b**) MCS = 100, **c**) MCS = 250, **d**) MCS = 500, **e**) MCS = 1000, **f**) MCS = 2000. All parameters used in the simulation can be found in Table A.1.

micropattern. With this parameter choice, the micropattern is not fully covered by the cell.

The cell on the V-shaped micropattern is initialized in the lower left corner of the substrate, which leads to an asymmetric spreading on the micropattern, see Fig. 5.2. The cell adheres fully to the left adhesive bar before it adheres to the right bar. Even after the *Cytoplasm* is in adhered to the full area of the micropattern, the asymmetric spreading is still apparent because the *Nucleus* moves slower towards the center of mass of the cell. After 2000 MCS, the final cell morphology is reached and the asymmetry observed during spreading is no longer visible.

We find a similar result for the cell spreading on the crossbow-micropattern, see Fig. 5.3. The cell is initialized in the top right corner of the substrate and adheres first to the right part of the adhesive arc, and then the *Cytoplasm* adheres further onto the left side of the adhesive arc and the straight bar. Again, the asymmetric spreading is visible even after the *Cytoplasm* is adhered fully to the crossbow. At this point, the cell shape does not follow the adhesive arc as the nucleus is moving slowly from the top right corner towards the center of mass of the cell. This leads

to different radii of the two invaginated arcs. However, the system equilibrates and after 2000 MCS, the invaginated arcs have the same radius and the cell shape follows the adhesive arc at the top of the structure.

The final cell shape geometries in Fig. 5.1f), Fig. 5.2f) and Fig. 5.3f) are as expected: the cell adheres to the adhesive parts and spans across non-adhesive areas, forming invaginated arcs. We compare our results to the 2D images of cells on micropatterns, and find qualitative agreement. For the U-shaped micropattern, we find a pronounced invaginated arc, similar to experimental findings [5, 96]. Similarly, we find one invaginated arc in cells on V-shaped micropatterns, which is also observed in experiments, however the simulated arc has a smaller radius compared to the experiment [96]. The cell shape on the crossbow micropattern closely resembles the experimental finding, but the elastic nucleus centering constraint leads to a nucleus positioned at the center of mass of the cell, which is an approximation. The equilibrium position of the centrosome and the nucleus is not necessarily at the center of mass of the cell, but at the center of an "inner zone", which is defined by the absence of actin bundles and the radically organized microtubules [5, 43].

5.1.2 Analysis of landmark points

Available microscopy data of cells on micropatterns is only two dimensional. This is useful for the comparison with 2D single cell models as described in Section 3.1.2. The 2D representation of single cells allows for straightforward visualization and interpretation of the model's results. Visualization tools and techniques are well-established for 2D data, aiding in the analysis and understanding of the simulated cellular behaviors. While modeling single cells in 2D offers several advantages, it is essential to consider the limitations. Cells in 2D models lack the full spatial context present in 3D environments, potentially overlooking crucial biological phenomena related to cell shape, mechanical interactions, and tissue organization. We chose the 3D single cell model for more accurate representation and understanding of 3D cell shape. However, the lack of experimental 3D data of single cells on micropatterns stops us from directly comparing experimental cell shapes with our simulation results. To better characterize the 3D cell morphology we obtain in our simulations, we rely on the analysis of landmark points [49].

We initialize 100 cells with nucleus with random starting positions on one of the three different micropatterns and use the Hamiltonian in Eq. 5.1 to evolve the system. We exclude cells from our analysis which are stationary because they are too far away from the micropattern to start spreading. As described previously in Section 5.1.1, asymmetric cell spreading is observed depending on the initial position

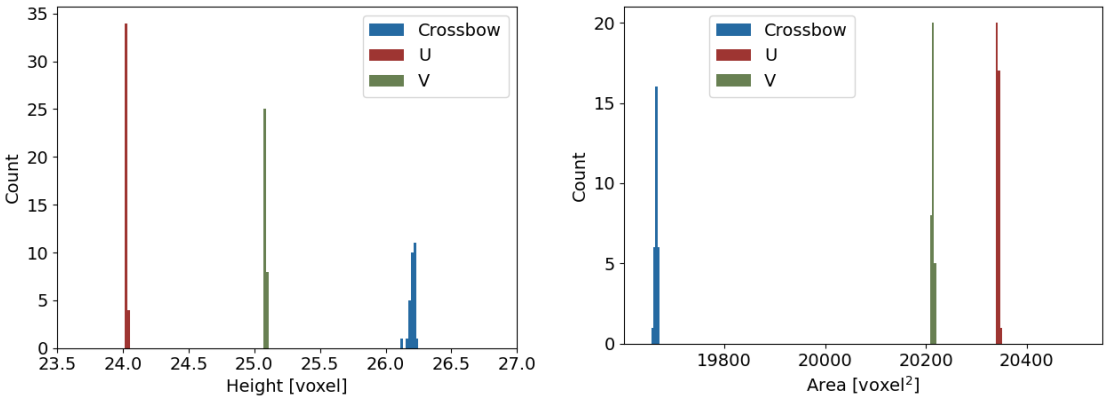

Figure 5.4: **Cell shape landmark points.** Height (left) and surface area (right) of the final cell morphology of cells with nucleus on U-shaped (38 simulations), V-shaped (33 simulations) and crossbow-shaped (29 simulations) micropatterns.

of the cell. However, the final cell shapes appear very similar and independent of starting position, for the same micropatterned surface.

To confirm that the cell morphology is indeed independent of the starting position of the cell, we compare landmark points of their shapes, specifically their height and area in Fig. 5.4. We find that the shape fluctuations of the final cell morphologies are minor and all cells reach a well-defined final shape that depends on the geometry of the micropattern they are adhered to. Even though the volume and area constraints are identical for cells on the different micropatterned structures, we find differences in their final height and surface area. Cells on U-shaped micropatterns have to spread out the most, leading to the lowest height and the highest surface area when compared to the cells on V-shaped and crossbow-shaped micropatterns. On the other hand, cells on crossbow-shaped micropatterns are more spherical, leading to a more spherical shape characterized by a lower surface area and an increased height.

Next, we compare the landmark points we obtained for cell shapes with nucleus, see Fig. 5.4, with landmark points from the simulations without nucleus with the Hamiltonian in Eq. 5.2. For simulations without expicit nucleus representation, we increase the target volume of the *Cytosol* by the target volume of the *Nucleus* and initiate the cell as a half sphere at a random position on the substrate. Similar to the simulations with nucleus, the cell spreads on the micropatterned surface and evolves to a well-defined equilibrium shape, see Fig. 5.5.

We find a slightly increased height between the simulations with and without nucleus, and the surface area of the cell is increased in the simulations without nucleus as well. The increase is observed for all three micropattern geometries,

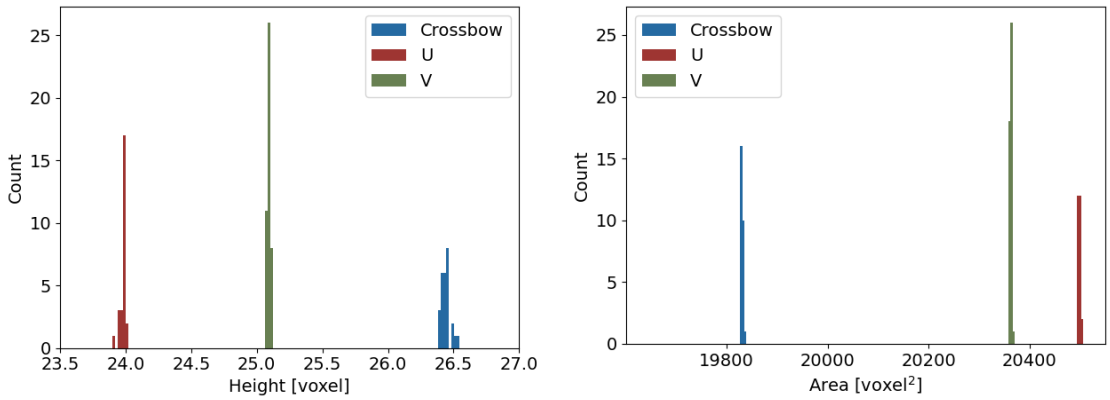

Figure 5.5: **Cell shape landmark points without nucleus.** Height (left) and surface area (right) of the final cell morphology of cells without explicit nucleus representation on U-shaped (26 simulations), V-shaped (45 simulations) and crossbow-shaped (27 simulations) micropatterns.

while the relative differences between morphologies in the different micropattern geometries remain similar. This increase is due to the fact that the explicit nucleus representation as a compartment inside the cytosol is implemented as a sphere, and even though the nucleus shape changes during the simulation, the elastic area energy term of the nucleus and the interaction energy penalty between cytosol and nucleus lead to a spherical nucleus shape. At the same time, the spherical nucleus imposes a more spherical shape on the cell, thus reducing the total surface area. In the absence of the nucleus, the equilibrium cell morphology has therefore a larger surface area. Thus we conclude that the cell can flatten more in the absence of the nucleus.

We note that even though we cannot compare these results directly to experiments, we expect experimental cells to show a larger variability in shapes than we observe in our simulations. Our simulations aim to describe average cell configurations on micropatterned structures and do not include individual cell surface fluctuations.

5.1.3 Trajectories of cells spreading on micropatterns

Next, we focus on the trajectories of the center of mass of the cells from the previously described simulations. By tracking the simulated movement of cells as they spread onto the micropatterns, we can observe speed and directionality. In Fig. 5.6, the trajectory of the center of mass of the cells starting at random positions on the substrate are shown. We find that the final cell shape and position is reached independently of the starting position of the cell, as long as the cell is initialized close enough to the micropattern. Additionally, we show the number of MCS until the final position is reached. As we discussed in Section 4.4, we can use the pseudo-time

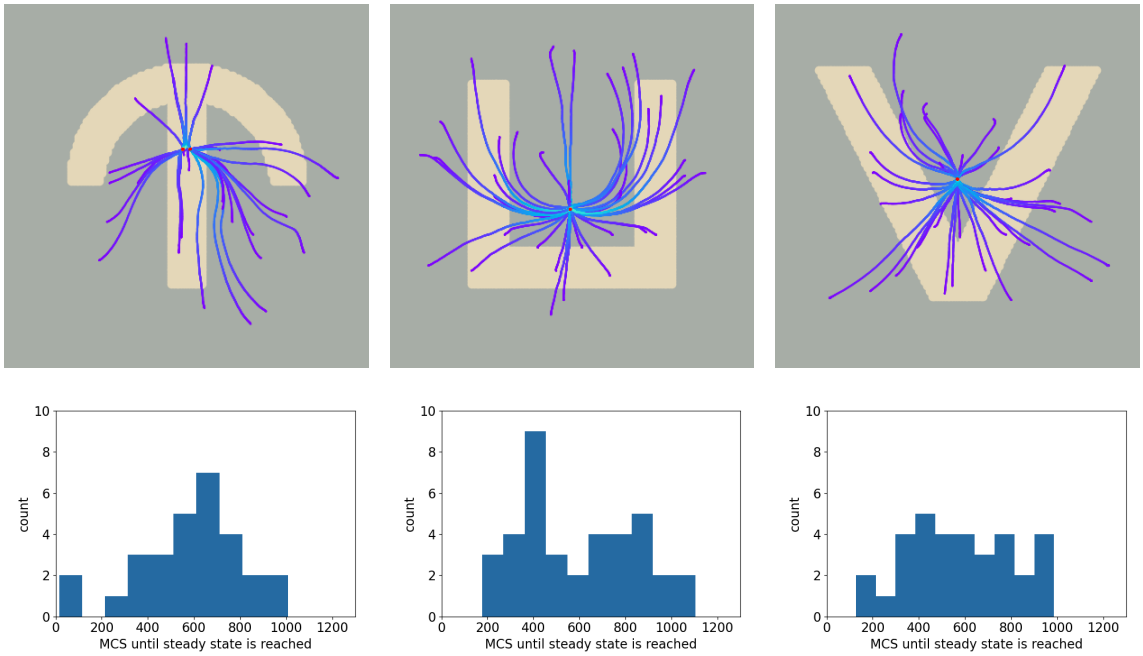

Figure 5.6: **Trajectories of the cell with nucleus spreading on micropatterns.** Center of mass trajectories of cells with explicit nucleus representation initialized randomly on the crossbow-shaped, U-shaped and V-shaped micropatterned scaffold, color coding represents MCS (top). Number of MCS until the final position is reached by the center of mass.

of the Monte Carlo simulation to describe the dynamical evolution of the system. Noticeably, the cell center of mass does not follow a straight line towards the final position, but tends to move more along the adhesive parts of the micropattern.

We further analyzed the trajectories of the cell center of mass for cells both without an explicit nucleus compartment, as depicted in Fig. 5.7. The trajectories of the cell center of mass for cells without nucleus compartment are comparable to the trajectories we found for cells with explicit nucleus compartment, see Fig. 5.6. However, the key distinction between the simulations lies in the number of MCS necessary until the final position is reached by the center of mass of the cell. For simulations without explicit nucleus representation, this is much smaller compared to the simulations with the nucleus. This observation can be attributed to two main factors: it is partially due to the fact that the additional interface between *Cytoplasm* and *Nucleus* in simulations with explicit nucleus representation increases the number of necessary spin flips for the cell to spread on the micropattern and because the nucleus as a stiff object slows down the migration speed. Due to these influences, it remains challenging to precisely quantify the extent to which the spreading speed would be altered in cells lacking a nucleus. Furthermore, given that the nucleus is not merely a stiff passive structure but actively participates in cell migration, the

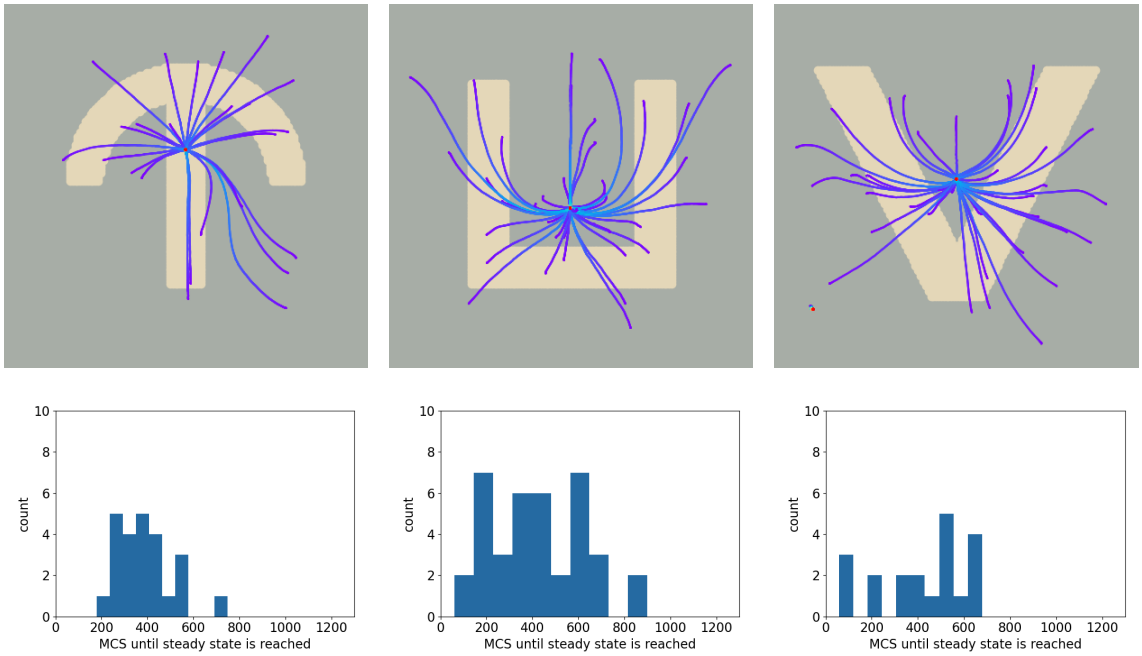

Figure 5.7: **Trajectories of the cell without nucleus spreading on micropatterns.** Center of mass trajectories of cells without explicit nucleus representation initialized randomly on the crossbow-shaped, U-shaped and V-shaped micropatterned scaffold, color coding represents MCS (top). Number of MCS until the final position is reached by the center of mass.

consequences of nucleus removal on cell spreading cannot be predicted from our model. Unraveling the full impact of nucleus absence on cell spreading necessitates further investigation beyond the scope of our simulations.

5.1.4 Influence of the neighbor order parameter on cell shape

In CPM simulations, the neighbor order N refers to the range of cell-cell interactions considered in the simulation, see Eq. 4.6. In other words, it defines the number of adjacent lattice sites, which are often called neighbors, that influence the behavior of a particular cell. A higher neighbor order allows for more complex cell-cell interactions but comes at the cost of increased computational complexity.

The neighbor order N is a very important parameter for simulated cell shape, see Fig. 5.8. For small neighbor order parameters $N < 20$, we find an almost sphere-like shape with extensions along the parallel bars of the U-shape instead of the expected invaginated arc. Note that for small N, the interaction energy J^{ext}(cytosol,adhesive) was increased to allow for cell spreading, as the energy gain due to increasing the interface between the *Cytoplasm* and the *Adhesive* cell types would not be higher than the increase in area constraint energy due to the extension.

The cells formed the invaginated arc only after increasing N above 10. Table 5.1 shows the relation between N and the distance "visible" to the cell, meaning that all voxels up to the distance displayed in Table 5.1 are used for the calculation of the interaction energy. Note that even for large neighbor order parameters N, the cell target volume $V_T = 68000$, which corresponds to a sphere with radius 25, is larger than the neighborhood area used for the interaction energy calculation, where for $N = 100$ voxels with a distance of up to 10.86 from the spin flip voxel are included in the calculation. Increasing the neighbor order incentivizes the cell to spread along the micropattern and makes the overall shape smoother. This is expected as a larger neighborhood is taken into account when calculating interaction energy changes.

Additionally, the neighbor order parameter N plays an important role for the radius of the invaginated arc. As discussed previously, cells in simulations with a small neighbor order N do not form invaginated arcs as the surface area energy can be reduced by becoming sphere-like, and at the same time no energy can be gained from the formation of invaginated arcs. Increasing the neighbor area leads to energy gains at voxels with a greater distance from the *Adhesive* substrate, which creates incentives for a less spherical cell shape.

5.2 Spreading dynamics of cells on micropatterns

Despite the widespread use of micropatterns for single-cell manipulation, experimental data on cell shapes predominantly exists in 2D. To compare aspects of our simulation with experimental results, we therefore compare the spreading dynamics and final cell shapes of our 3D simulation only as a 2D projection. The 2D projection of the simulated spreading dynamics of cell with nucleus on a V-shaped micropattern can be seen in Fig. 5.9, next to experimental data of a human Retinal Pigmented

Neighbor Order N	Distance
1	1.00
4	2.00
7	2.83
10	3.32
30	5.91
60	8.37
100	10.86

Table 5.1: Correspondence between the neighbor order parameter N and the maximal distance from the voxel that is included in the interaction energy calculation.

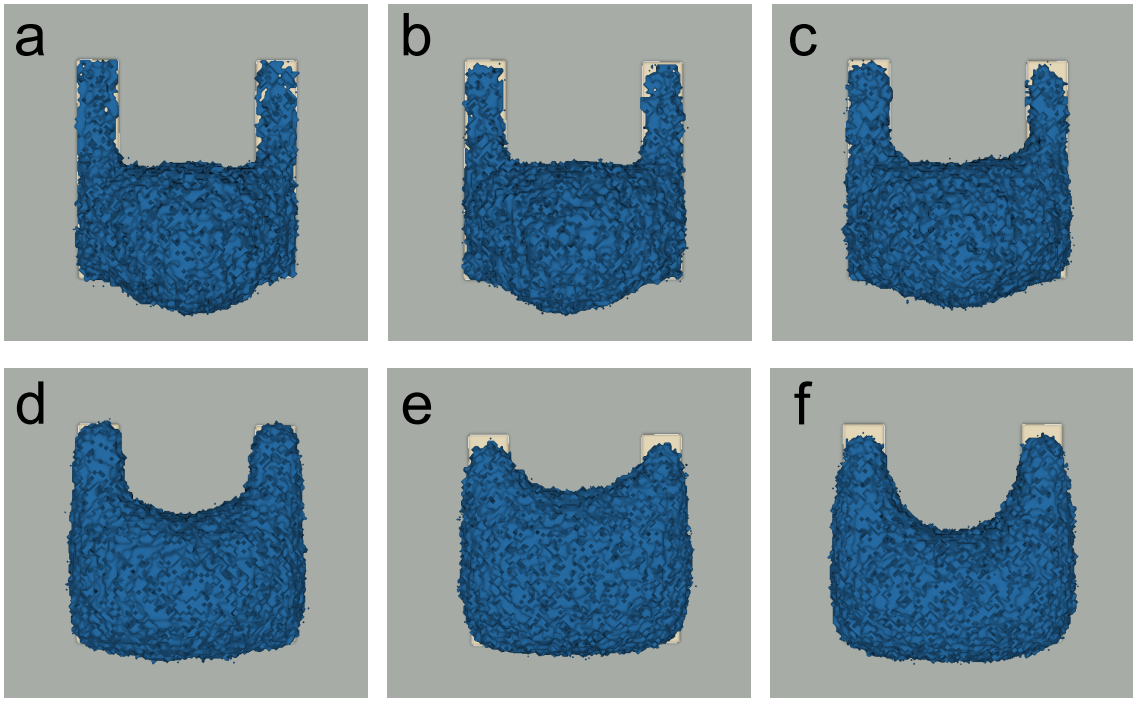

Figure 5.8: **Neighbor Order N dependence for cell shapes on micropatterned substrates.** **a**) $N = 1$, **b**) $N = 4$, **c**) $N = 10$, **d**) $N = 30$, **e**) $N = 60$, **f**) $N = 100$. All parameters used in the simulations can be found in Table A.2.

Epithelial cell on a V-shaped micropattern [96]. This comparison allows us to gain insights into the correspondence between our computational model and experimental observations.

The experimental images were obtained using reflection interference contract microscopy, where area with cell-substrate contacts appear black, and areas with less contact appear white or gray. Our simulated cell spreading on a V-shaped micropattern is initialized to adhere partially to the micropattern, in order to replicate the experimental data. Remarkably, our simulations successfully reproduced several experimentally observed spreading features quantitatively, such as the invaginated arc across the nonadhesive area and that the cell adheres completely to the right bar while only partially adhering to the left bar due to the asymmetric starting position of the cell. However, it is important to acknowledge one notable distinction between our simulations and experimental setups. In our computational model, we assumed spreading from the nonadhesive surface to the micropattern, while experimental cells often adhere to micropatterns from suspension. This dissimilarity does not diminish the overall similarities between our simulation and experimental results in capturing the spreading dynamics on the V-shaped micropattern. These findings underscore the robustness and utility of our computational approach in emulating key aspects

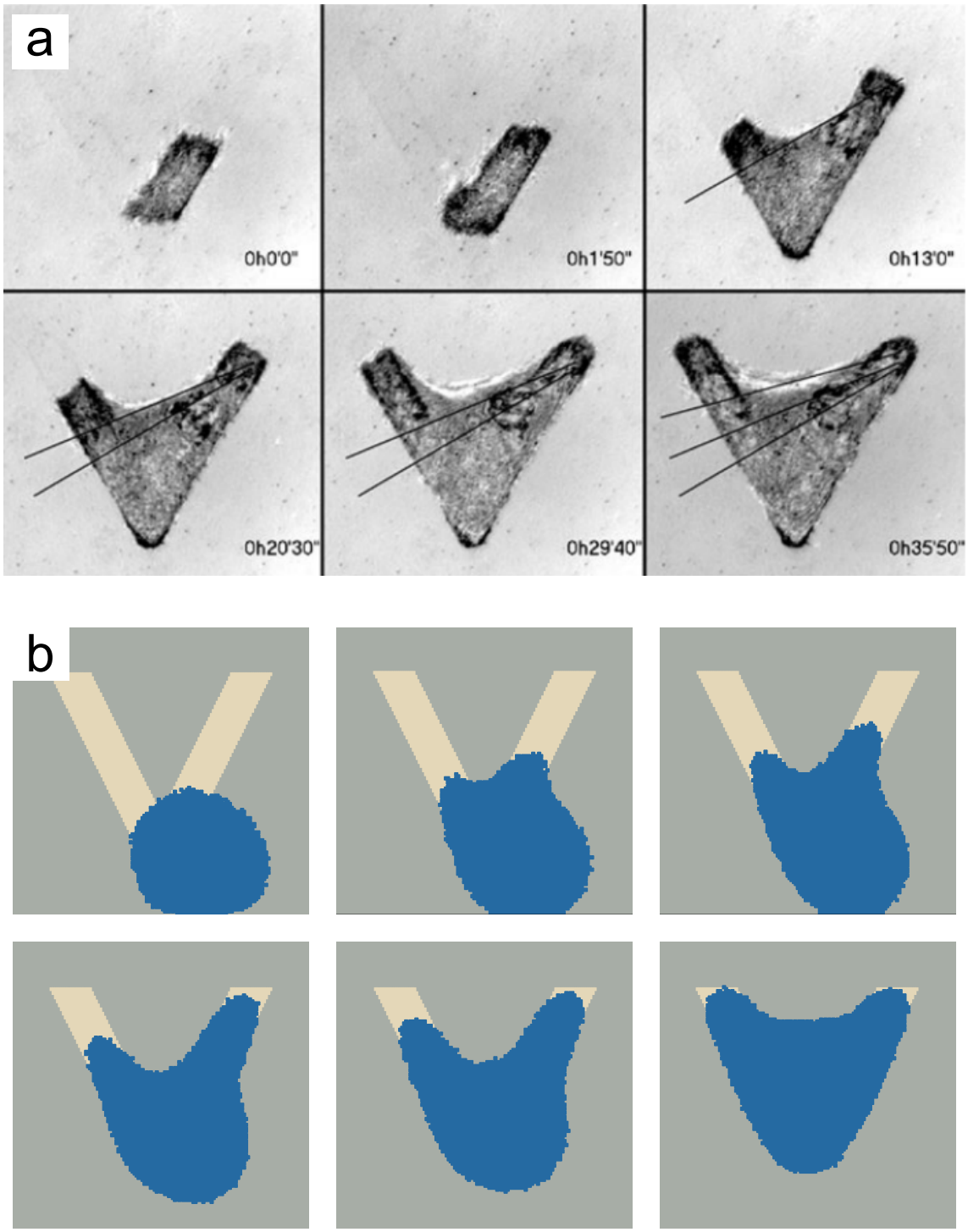

Figure 5.9: **Cell spreading on micropatterns. a**) Time lapse of a human Retina Pigmented Epithelial cell spreading on a V-shaped micropattern. **b**) Cross section images from the 3D simulation of a cell spreading on a V-shaped micropattern. Note that in the experiment, the cell spreads onto the micropattern from the solution while our initial configuration in the simulation is a half sphere. Parameters for the simulation can be found in Table A.1.
a) Reproduced with permission [96], 2006, Wiley.

of real cellular behavior while allowing for important insights into cell-substrate interactions.

Following the initial phase of cell spreading, subsequent changes to the cell shape occur at a slower pace and exhibit more subtle alterations, resulting in a reduction in the curvature of the invaginated arc, a process called reinforcement. In addition to the surface tension stemming from the actin cortex, the line tension is predominantly influenced by the presence of actin stress fibers at the cell periphery. The change in curvature of the invaginated arc is a result of stress fiber reinforcement, which leads to an increase of line tension at the invaginated arc. In addition to the surface tension due to the actin cortex, the line tension is the result of actin stress fibers at the cell periphery. In the following Section 5.3, we present our approach to incorporating line tension within the Cellular Potts Model (CPM), thereby elucidating the underlying mechanisms and dynamics governing this phenomenon.

5.3 Stress fibers in the 3D cellular Potts model

Up to this point, we have modeled cells as objects with volume and surface constraints that obtain their shape due to interaction energies minimized with volume and surface constraints. We implemented the nucleus as a compartment of the cell, which has an - albeit relatively modest - effect on effect on the cell shape by making it more spherical. This model allowed us to qualitatively predict cell spreading on micropatterned surfaces as discussed in the previous sections of this chapter. However, it is well known that cells in experiments go through an internal reinforcement process after the spreading event [96]. An important internal structure are stress fibers, which were introduced in Section 2 and form in regions of high stress [34].

Several cell models that include stress fibers have already been described in the literature. Bischofs and colleagues use a contour model to describe the static boundary of cells on micropatterned surfaces [264]. Stress fibers are included in the 2D model as a line tension counteracting the surface tension. The biological structures modeled with the line tension are the actin cortex and stress fibers, which resist the increase of cell contour. This tension-elasticity model explains invaginated arcs forming between adhesive sites, where the radius of the invagination depends on the distance between the adhesive points. Schakenraad and colleagues observed elliptical invaginations in cells with an anisotropic cytoskeleton and modeled this observation with a contour model that predicts cell shapes from the orientation of the stress fibers [302]. Here, the line tension varies along the cellular arc. Recently, Andersen and colleagues introduced stress fibers as active linear elastic materials in a two-dimensional finite

element model to describe the effect of optogenetic activation of the Rho-pathway for single cells and doubles in H-shaped micropatterns [137].

Stress fibers have also been implemented in the 2D CPM by Albert and colleagues [362]. The Hamiltonian contains terms for 2D surface tension, adhesion to the micropattern as well as linear and elastic terms for the line tension. The linear term is proportional to the whole perimeter of the cell, thus modeling the effect of the contracting actin cortex, whereas the elastic line tension models the stress fibers forming between adhesive sites. It depends on the squared difference between the length of the cell contour between adhesive sites and their distance, following the tension-elasticity model.

In 3D models, the cell contour is a two-dimensional surface instead of the one-dimensional perimeter that describes the cell interface in 2D models. The assumption that stress fibers form between adhesive sites along the perimeter of the cell cannot be generalized to the 3D CPM, because singling out voxels on the cell surface and attributing them with an additional line tension is a local process that could easily lead to rupture of the simulated cell. To ensure that the line tension effect of the stress fibers has an effect similar to the experimentally observed reinforcement, we introduce compartments to the cytoplasm of our simulated cells. These compartments do not represent any physical intracellular structures of the cell, but serve as anchorage points for stress fibers growing through the cytoplasm. The introduced line tension therefore affects the cell shape on a larger scale.

The Hamiltonian for the simulation of stress fibers in a single cell on a micropattern is therefore given by

$$
\begin{aligned}
\mathcal{H}_{\mathrm{CPM}} = & \sum_{(\vec{i},\vec{j}) \text{ neighbors}} J^{\mathrm{int}}(\tau(\sigma(\vec{i})),\tau(\sigma(\vec{j}))) \cdot \Big(1-\delta(\sigma(\vec{i}),\sigma(\vec{j}))\Big) \cdot \delta(\alpha(\vec{i}),\alpha(\vec{j})) \\
& + \sum_{(\vec{i},\vec{j}) \text{ neighbors}} J^{\mathrm{ext}}(\tau(\sigma(\vec{i})),\tau(\sigma(\vec{j}))) \cdot \Big(1-\delta(\sigma(\vec{i}),\sigma(\vec{j}))\Big) \cdot \Big(1-\delta(\alpha(\vec{i}),\alpha(\vec{j}))\Big) \\
& + \sum_{\sigma} \lambda_{\mathrm{V}}(\tau(\sigma))\,(v(\sigma)-V_{\mathrm{T}}(\tau(\sigma))^2 + \sum_{\sigma} \lambda_{\mathrm{A}}(\tau(\sigma))\,(a(\sigma)-A_{\mathrm{T}}(\tau(\sigma))^2 \\
& + \sum_{\alpha} \lambda_A(\alpha)(a(\alpha)-A_{\mathrm{T}}(\alpha))^2 + \lambda_{\mathrm{C}}(\vec{X}_{\mathrm{cell}}-\vec{X}_{\mathrm{nucleus}})^2 \\
& + \sum_{\text{SF between } \sigma_i,\sigma_j} \lambda_{\mathrm{SF}} l_{i,j},
\end{aligned}
\tag{5.3}
$$

which differs compared to the Hamiltonian in Eq. 5.1 due to the linear line tension with strength λ_{SF} and distance between the center of mass of the respective compartments

with stress fibers $l_{i,j}$. For simplicity, we assume that stress fibers do not interact with each other, and new stress fibers can only form between compartments where no stress fibers are present. Note that the target volume and area of the cytoplasm change due to the compartmentalization.

5.3.1 Stress fiber reinforcement

As discussed in Section 5.2, cells undergo a process of stress fiber reinforcement at the invaginated arc once they have achieved complete spreading on the micropattern. Throughout this phase, the cell actively reduces the curvature at the invaginated arc gradually, until it reaches its final shape. Notably, the radius of curvature increases almost linearly during both the initial cell spreading and the subsequent reinforcement stages, as documented by Théry and colleagues [96].

To model this behavior, we place a compartmentalized cell with an invaginated arc on a V-shaped micropattern. We implement the stress fiber reinforcement process in our CPM with a linear line tension energy between the center of mass of the cytoplasm compartments along the invaginated arc of the cell, see Fig. 5.10.

During the simulation, the line tension exerts forces on the cell boundary, resulting in an increased radius of the invaginated arc. This process continues until an equilibrium is achieved between the line tension and the surface tension, closely resembling the observations made in experimental studies. By implementing this reinforcement mechanism within our CPM, we successfully capture the dynamic changes in cell shape.

5.3.2 Stress fiber growth and disaggregation

The prove of concept in the previous section demonstrates that it is possible to include stress fibers that change cell shape in 3D CPM simulations. However, up to this point we predefined the position of the stress fiber before the simulation. Now, we will discuss different approaches to implement stress fiber growth and disaggregation in the CPM. The difficulty when implementing stress fiber growth in the CPM is that stress fibers form in regions of increased stress within the cell, but the stress distribution cannot be calculated in the framework of the CPM as it is lacking a description of elastic deformation. Therefore, we use different measures to guide stress fiber growth in the CPM and simulate a combination of transverse arcs and dorsal stress fibers.

We change the experimental system that we model, and describe a compartmentalized cell attached to four adhesive sites inspired by the stimuli-responsive structures in

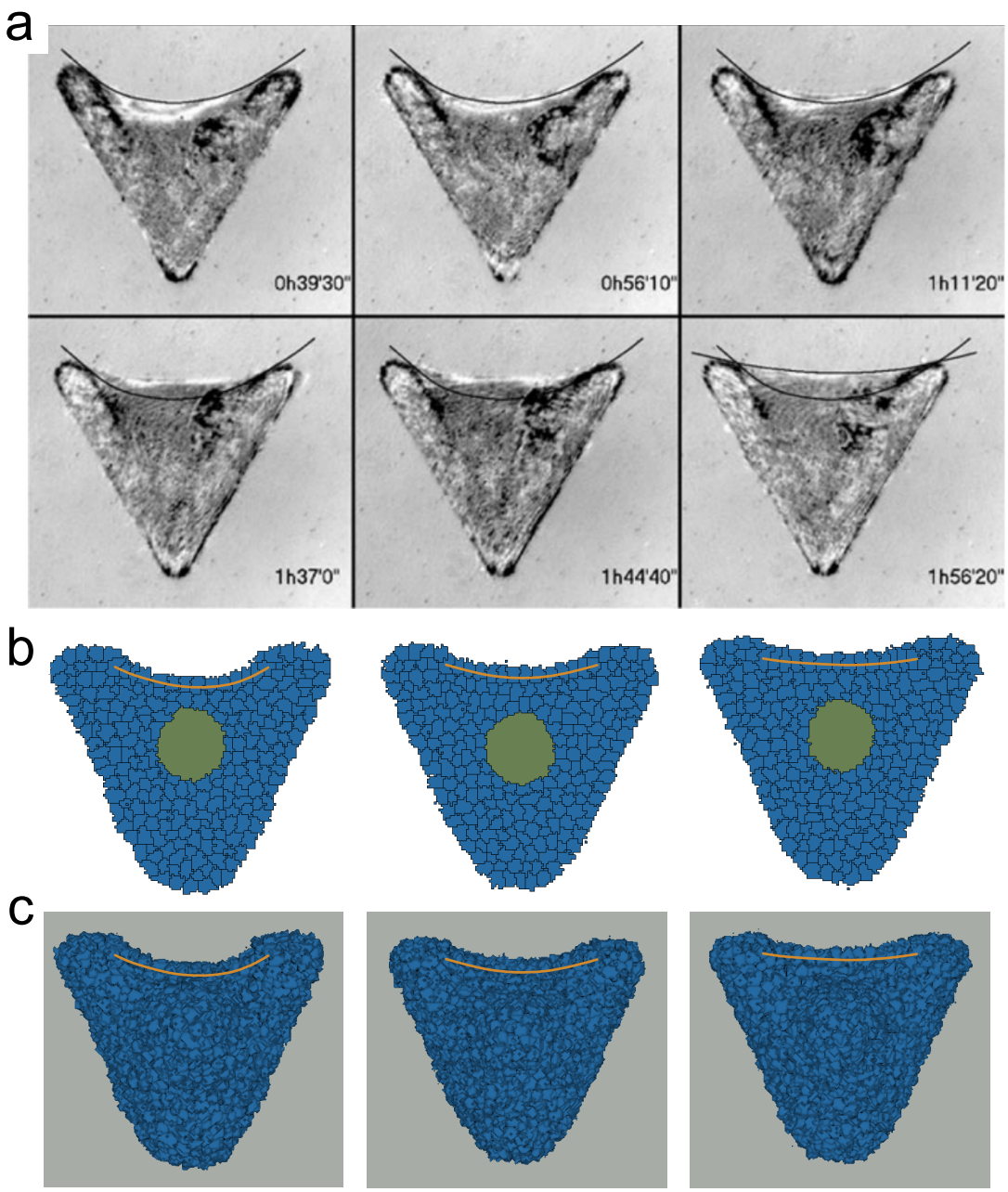

Figure 5.10: **Cell reinforcement on micropatterns.** **a**) Time lapse of cell reinforcement on a V-shaped micropattern. Arcs are drawn to guide the eye. **b**) Cross section images from the 3D simulation of a cell with stress fiber (orange) on a V-shaped micropattern. **c**) Images of the 3D shapes of simulated cells with line tension on micropatterns. b,c) Snapshots from the simulation at MCS 0, 100, 1000 (left to right). Parameters for the simulation can be found in A.3.
a) Reproduced with permission [96], 2006, Wiley.

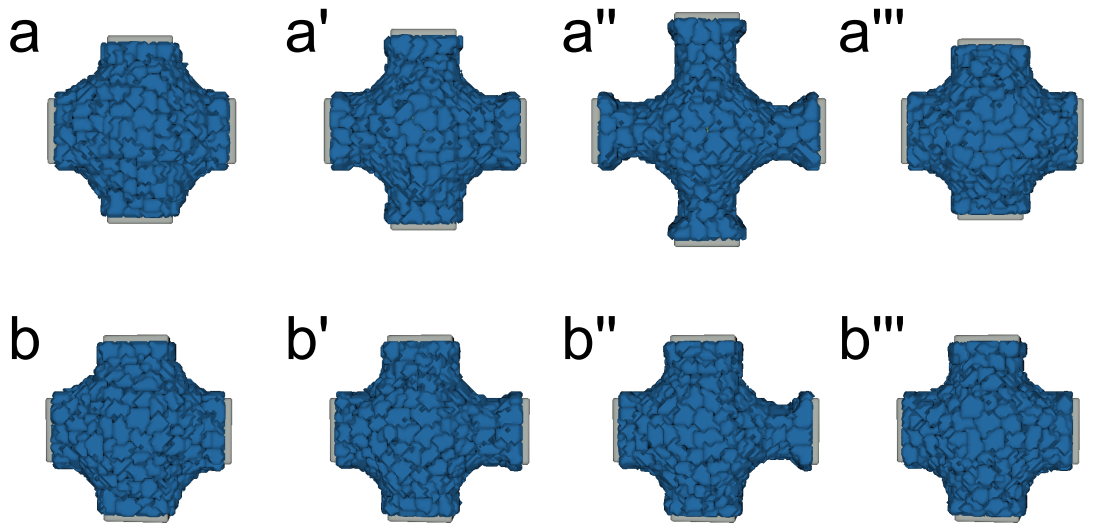

Figure 5.11: **3D cell stretching simulation.** Top view of the symmetric (**a-a‴**) and asymmetric (**b-b‴**) 3D cell stretching simulations. In symmetric simulations, all adhesive sites are moved. In asymmetric simulations, only the adhesive site on the right is moved. Cytoplasm compartments are depicted in blue and adhesive sites in gray. **a,b**) Initial configuration of the symmetric (a) and asymmetric (b) cell stretching simulation. **a′, b′**) Snapshot of the symmetric (a′) and asymmetric (b′) cell stretching simulation after 110 MCS. **a″,b″**) Snapshot of the symmetric (a″) and asymmetric (b″) cell stretching simulation after 410 MCS. **a‴,b‴**) Snapshot of the symmetric (a‴) and asymmetric (b‴) cell stretching simulation after 810 MCS. Parameters for the simulation can be found in A.4.

[185], compare Fig. 3.2f,f′). This microscaffold was chosen because the cell stretching due to the expanding host-guest hydrogel exerts stress on the cell and leads to the formation of stress fibers. Indeed, cytoskeletal reorganisation is observed in U2OS and NIH 3T3 cells immediately after cell stretching and stress fibers form along the cell contour and in the cell center. Additionally, Hippler and colleagues observed that stress fibers form predominantly in stretched regions after asymmetric stretches, where only one adhesive site is deflected [185].

The initial configuration of the simulation is a single cell modeled as a cluster with nucleus and compartmentalized cytoplasm attached to four adhesive sites, see Fig. 5.11a,b). The displacement of the scaffold is modeled effectively by changing the position of the adhesive sites after a predefined number of MCS. To replicate the experiment, the adhesive sites move outwards after every 50 MCS after the first 100 MCS and up to 450 MCS. Then, the adhesive sites retract invards every 50 MCS between MCS 450-800. This leads to significant cell stretching, compare Fig. 5.11.

After the retraction phase, the cell shape reverts to a configuration similar to the cells initial shape or a shape that closely resembles it. This phenomenon is observed for cells in the experiment and underscores that the cell can effectively adapt their force machinery and respond to changes in its microenvironment while maintaining its overall structural integrity.

In our simulation, stress fibers grow from adhesive sites throughout the cytoplasm compartments, where each compartment can have no more than one stress fiber anchored to its center of mass. Stress fibers can grow towards each other and combine at a cytoplasm compartment. As we cannot explicitly simulate the stress distribution in the cell, we take either the pressure inside the compartment or the reduced volume of the compartment as an indirect measure of how much stress the compartment experiences. Stress fibers disaggregate in our simulation if their length is much larger than their end-to-end distance. Every 10 MCS, stress fibers are modified. If a compartment is neighboring the adhesive site and does not have a stress fiber yet, the probability for a new stress fiber to start is $p_{\text{start}} = 0.2$. The stress fiber then grows every 10 MCS to neighboring compartments until it reaches a cytoplasm compartment neighboring another adhesive site, where the stress fiber is considered complete and the growth is stopped. After every growth period, the algorithm checks all stress fibers and deletes them with a probability depending on the ratio between end-to-end distance d and length ℓ of the stress fiber. The end-to-end distance is the Euclidean distance between the center of mass of the first and last compartments of the stress fiber. We use a Hill-equation with

$$p_{\text{delete}} = \frac{K^H}{K^H + (d/\ell)^H}, \tag{5.4}$$

where $H = 10$ defines the steepness of the curve and $K = 0.6$ is chosen such that stress fibers with $\frac{d}{\ell} = 0.6$ are have a probability of $p_{\text{delete}} = 0.5$ to be deleted. Stress fibers are always deleted instantly and completely.

As a first strategy, we approximated the stress distribution inside the simulated cell with the pressure inside the cytoplasm compartment. The pressure is proportional to the difference between the volume and the target volume of the compartment. Stress fibers then extend to the neighboring compartment with the highest pressure which does not yet have a stress fiber. Snapshots of the simulation can be seen in Fig. 5.12a,b). For the symmetric cell stretching experiment (Fig. 5.12a), we expect stress fibers forming along the invaginated arcs spanning between adhesive sites. After only 140 MCS, stress fibers form along two of the four invaginated arcs. They are not deleted throughout the simulation and remain at the same position during

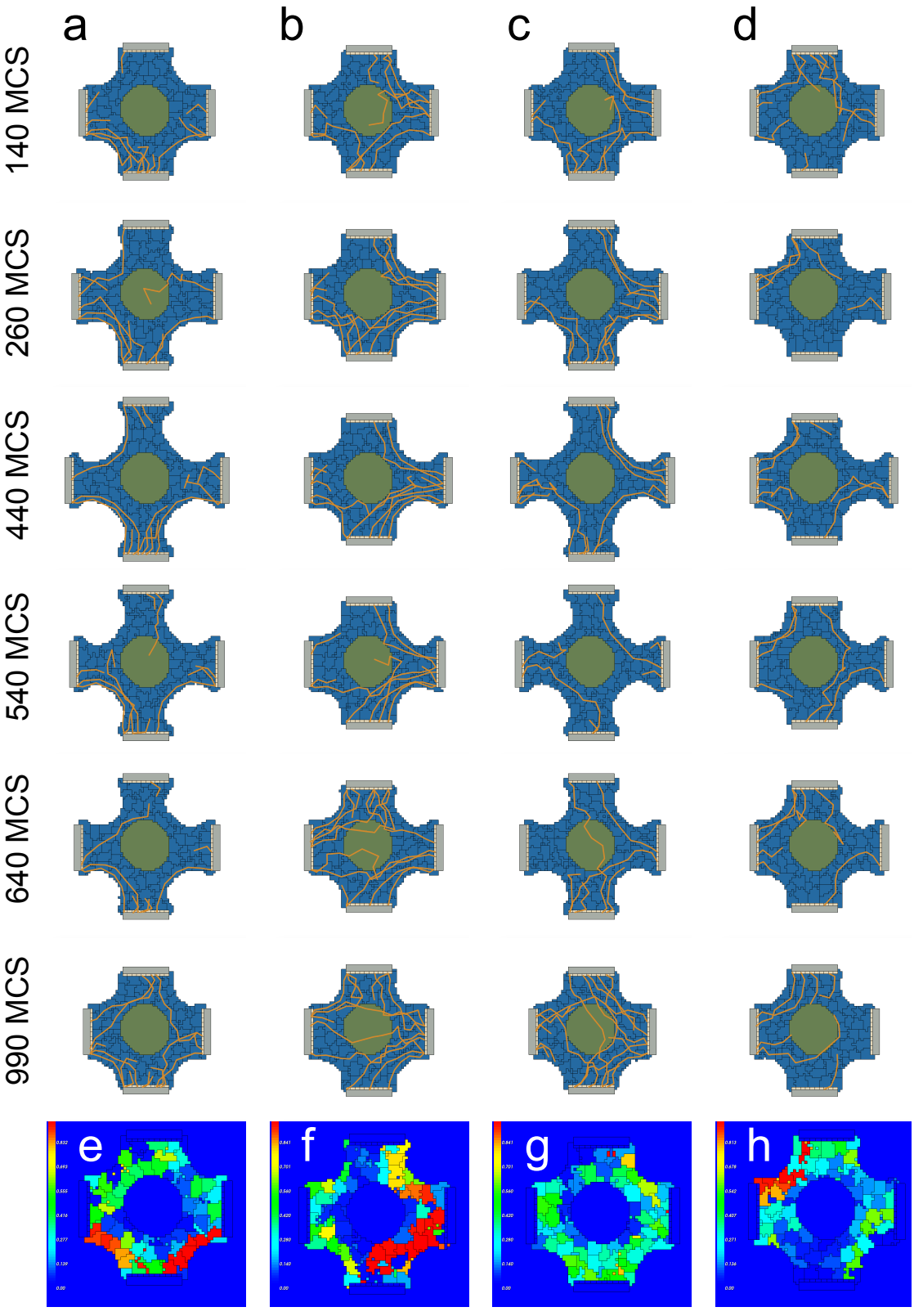
a
b
c
d
140 MCS
260 MCS
440 MCS
540 MCS
640 MCS
990 MCS
e
f
g
h

Figure 5.12: **Cross section images of cell stretching simulations.** Cytoplasm compartments are depicted in blue, the nucleus in green, stress fibers in orange and adhesive and non-adhesive parts of the scaffold in beige and gray. Stress fibers are projected onto the 2D plane. **a**) Snapshots of the symmetric stretching simulation, stress fibers extend to the neighboring cytoplasm compartment with the highest pressure. **b**) Snapshots of the asymmetric stretching simulation, stress fibers extend to the neighboring cytoplasm compartment with the highest pressure. **c**) Snapshots of the symmetric stretching simulation, stress fibers extend to the neighboring cytoplasm compartment with the lowest reduced volume. **d**) Snapshots of the asymmetric stretching simulation, stress fibers extend to the neighboring cytoplasm compartment with the lowest reduced volume. **e**) Stress fiber density after 1000 MCS symmetric stretching simulation. Stress fiber growth is pressure-dependent. **f**) Stress fiber density after 1000 MCS asymmetric stretching simulation. Stress fiber growth is pressure-dependent. **g**) Stress fiber density after 1000 MCS symmetric stretching simulation. Stress fiber growth is reduced volume-dependent. **h**) Stress fiber density after 1000 MCS asymmetric stretching simulation. Stress fiber growth is reduced volume-dependent. Parameters for the simulations can be found in A.4.

cell stretching (0-449 MCS) and relaxation (450-1000 MCS). Additionally, we observe stress fiber growth throughout the rest of the cell volume, but here stress fibers are deleted frequently. This can also be seen in the stress fiber density in the compartments at the end of the simulation. The stress fiber density is the number of MCS a stress fiber is present in the compartment divided by the total number of MCS, and the result can be seen in Fig. 5.12e). The density is high in areas with lasting stress fibers, whereas areas with frequent growth and deletion have lower stress fiber densities.

We performed a similar simulation, but with asymmetric cell stretching by altering the position of a single adhesive site, see Fig. 5.11b-b‴) and Fig. 5.12b). In this case, we see a notable increase of stress fibers at the stretched regions of the cell. This observation is further supported by the stress fiber density post simulation in Fig. 5.12f), which is similar to the experimental findings. Furthermore, we observe that stress fibers present in the stretched areas have an increased lifetime compared to those in other regions of the cell.

As we see increased stress fiber density along the invaginated arcs of stretched cells during asymmetric stretching, but no homogeneous distribution of stress fiber density in the symmetric stretching, we implemented a second strategy to model stress fiber growth in our simulation and used the reduced volume of the compartments as a measure of their deformation and a substitute for stress distribution inside the cell. The reduced volume v is a measure of deformation of the cytoplasmic compartments,

as it quantifies how much a shape differs from a perfect sphere. It is given by

$$v = \frac{V}{\frac{4\pi}{3}R_0^3}, \tag{5.5}$$

where V is the volume of the cell and R_0 is computed from the surface area A of the cell as $A = 4\pi R_0^2$. A reduced volume of 1 indicates a perfect sphere, while all other shapes have a lower reduced volume. Stress fiber initialization and deaggregation assumtions were not changed, the probability to start a new stress fiber is given by $p_{\text{start}} = 0.2$ and the probability to delete a stress fiber remains, compare Eq. 5.4. We again simulated symmetric and asymmetric extension and retraction of the microstructure, see Fig. 5.12c,d).

For the symmetric cell stretching, we now find a more homogeneous distribution of stress fibers throughout the cell, see Fig. 5.12c,g). The homogeneity within the cell is as expected, however, contrary to our expectations, we did not observe an increase in stress fibers at the invaginated arcs, despite these regions being known to experience high stress levels in the experiment. This leads us to the conclusion that the reduced volume of the compartments is not a good substitute for the stress distribution inside the cell.

For the asymmetric stretching experiment, a discrepancy between our simulation and the experimental result is evident: there is no increase in stress fiber density at the stretched area, see Fig. 5.12d,h). This significant difference suggests that our current model with stress fiber growth in compartments with low reduced volume might not capture the relevant aspects of stress fiber growth. Additionally, there could be other factors or mechanisms at play in the experimental setting that are not adequately accounted for in our simulation.

In conclusion, our model, while providing valuable insights, encountered challenges in accurately predicting stress fiber density during both symmetric and asymmetric stretching scenarios. Stress fiber dynamics involve intricate biological processes influenced by a myriad of factors, such as actin binding proteins and external mechanical stimuli. Although the introduction of cytoplasm compartments enabled us to effectively simulate cell shape changes driven by stress fibers, specifically when initializing stress fibers at the beginning of the simulation, it is important to acknowledge that our model does not fully capture stress fiber growth and dynamics. Specifically stress fiber movement in retrograde flow, which is observed during cell spreading, is difficult to replicate in our model.

Moreover, stress fibers play crucial roles as sensors and transmitters of external forces acting on the cell. Unfortunately, due to the pseudo-energy terms inherent

in the CPM, we were unable to incorporate this important aspect into our model. However, this limitation highlights the complexity of stress fiber behavior and their role in cell shape changes and the need for further research to account for these intricate processes.

For a successful cell-scale CPM with stress fibers, one therefore needs the stress distribution inside the cell to accurately model stress fiber growth and rearrangement. This could be achieved by coupling the CPM with a finite element model that calculates the stress distribution inside the cell from the deformation changes modeled with the CPM. To account for stress fiber dynamics, for example due to retrograde flow, one could change the compartmentalization of the cell: instead of equally sized compartments, the cell could be modeled by a large compartment and several small compartments that act as anchorage points for stress fibers. Then, the stress fiber growing between small compartments could move the small compartments throughout the cytosol. Despite these challenges, our study lays the foundation for future investigations into stress fiber dynamics and their influence on cell mechanics. By understanding the complex interplay between stress fibers and various internal and external factors, we can advance our comprehension of cellular responses to mechanical cues, potentially leading to new insights into cell behavior and tissue mechanics.

5.4 Discussion

In this chapter, we overcame the limitations of 2D models for cells on micropatterns and implemented a 3D CPM for single cells on structured environments. With this model, we can predict the complete cell shape instead of a 2D projection. We were able to model cell shapes and dynamics during cell spreading and reinforcement. Here, the correct choice of neighbor order N was important to obtain the characteristic invaginated arcs.

Additionally, we investigated the effect of the nucleus and found minimal differences in the cell shape, where cells with explicit nucleus representation were more spherical and had a reduced surface area. For the spreading dynamics, we found similar cell shapes during spreading, such as invaginated arcs between adhesive sites. Cell trajectories during spreading were similar with and without explicit nucleus representation, but cells without nucleus reached the steady state faster.

Finally, we added stress fibers to our model by compartmentalizing the cell cytosplasm in our simulations. When we predefine the position of the stress fibers, we can reproduce the experimentally observed reinforcement of cells on micropatterns.

However, modeling stress fiber growth and disaggregation is more challenging as there is no measure for stress in the CPM.

6 Modeling cell shape in 3D structured environments*

Cell shape plays a fundamental role in many biological processes, including migration, division and morphogenesis, and thus modeling cell morphology is essential to predict and control the behavior of cells in complex environments. While there is a variety of two-dimensional models and experimental data for the shape of cells on flat substrates, it is less clear which shape model best predicts three-dimensional cell shape in structured environments. In Chapter 5, we developed models to describe 3D cell shape on micropatterns. In this chapter, we focus on several modeling approaches for cell shape in 3D structured environments. Additionally, we use 3D experimental data of cells in structured environments to test the validity of our models and to compare the different modeling approaches. In contrast to the philosophy of the vertex model often used for epithelial sheets and described in Section 4.2, we find that models based only on cortical tension as a constant geometrical surface tension are not sufficient to describe the shape of single cells in 3D. Therefore, we employ different variants of the CPM, where a target area is prescribed by an elastic constraint or the area energy is described with a linear surface tension. By comparing the simulated shapes to experimental images of cells in structures manufactured with DLW, we can identify parameters that accurately model the 3D cell shape.

Modeling cell shape in structured environments plays an important role in increasing and validating our understanding of the underlying mechanisms governing cell behavior. Analytical 2D cell shape models have been developed to predict cell shape on micropatterned environments [19, 301] using line and surface tensions as discussed in Section 4.1.1, and the notion that the contractile actin cortex is responsible for the 3D cell shape is wide-spread [29, 31]. 3D models have relied on different approaches, including neural networks [364] and learned probability distributions [365] to predict cell shapes. Here, we employ energy-based descriptions to model cell shape in well-defined environments and compare different surface energy descriptions. Our approach provides a robust framework for modeling complex 3D cell shapes and

*This chapter is based on Link, R., Jaggy, M., Bastmeyer, M., & Schwarz, U. S. (2023). Modelling Cell Shape in 3D Structured Environments: A Quantitative Comparison with Experiments. *bioRxiv*, 2023.08.07.552225. https://doi.org/10.1101/2023.08.07.552225 [363].

has the potential to improve our understanding of the fundamental principles that govern cell behavior in structured environments.

6.1 Single cells in 3D laser nanoprinted structures

6.1.1 3D structures for cell adhesion

Structured environments were manufactured using 3D DLW [366], a method we introduced in Section 3.1.3. In this technique, a photopolymerizable resist is excited with a femtosecond-pulsed laser. The resist only polymerizes after a two-photon adsorption, and because the probability for a two-photon polymerization is only in the focal voxel of the laser high enough, complex structures can be printed with micrometer precision.

The fabricated structures consisted of L-shaped, rectangular, V-shaped and triangular shaped patterns, see Fig. 6.1a-a‴,b-b‴) with 15 µm high anti-adhesive columns connected by biofunctionalized cross struts of 5 µm width, providing a suitable platform for cell adhesion in 3D. These geometries were selected to resemble the shapes of 2D micropatterns, which are well characterized in terms of 2D cell shapes [43], while eliminating the apico-basal polarity observed in cells on substrates.

To functionalize the structures, they were first rinsed with 70% ethanol (Carl Roth) and then dried for 30 min under UV light. Thereafter, the structures were overcoated with 200 µg/ml poly-L-lysine (Sigma-Aldrich) dissolved in PBS for 1 h at room temperature and then washed three times with PBS. This was followed by incubation with 10 µg/ml fibronectin in PBS for 1 h at room temperature. The functionalized structures can be seen in Fig. 6.1c-c‴). After washing again three times with PBS, the structures were either used directly or stored for a maximum of two days at 4°C.

6.1.2 Cell culture

NIH/3T3 embryonic mouse fibroblast cells were cultured at standard conditions (saturated humidity, 37°C, 5% CO_2) in serum containing medium and passaged three times per week to avoid contact inhibition. During passaging, cells were first rinsed twice with pre-warmed PBS and then incubated with 250 µL, 5% trypsin / 10 mM EDTA (Invitrogen) at 37°C for 3 min to allow cells to detach from the substrate. The cell suspension was taken up in 5 ml of pre-warmed DMEM (Invitrogen) containing 10% fetal calf serum (FCS, PAA Laboratories). The serum in the medium provides saturation of trypsin. The cells were then centrifuged at 1000 rpm for 5 min.

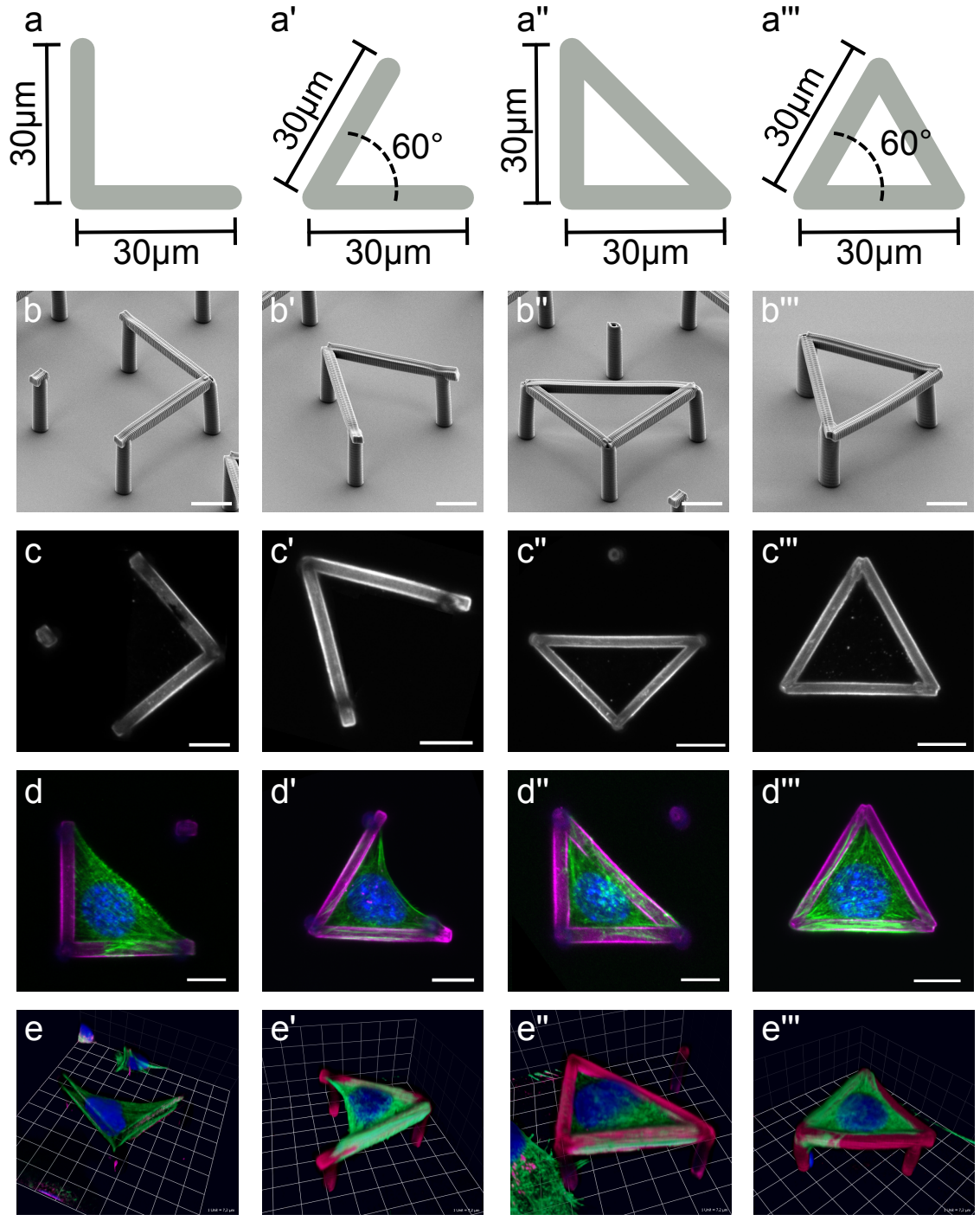
a
a'
a''
a'''
30µm
30µm
30µm
30µm
60°
30µm
30µm
60°
30µm
30µm
b
b'
b''
b'''
c
c'
c''
c'''
d
d'
d''
d'''
e
e'
e''
e'''

Figure 6.1: **Overview of the structures used in this chapter. a-a‴**) Dimensions of the 3D structures, top view. Shown in gray is the contact area ("cross struts") for the cells in the L-shaped (a), V-shaped (a′), right triangle-shaped (a″) and equilateral triangle-shaped (a‴) structures. The width of the struts is 5 µm. The supporting columns (not depicted) have a height of 15 µm. The angles not shown are 90°and 45°. **b-b‴**) Scanning electron microscope images of the 3D structures. **c-c‴**) Fluorescence imaging of the structures after fibronectin coating and immunohistochemical staining. **d-d‴**) NIH/3T3 cells were transferred into the fibronectin-coated structures using a micromanipulator, fixed after 3-6 h, and stained immunohistochemically (fibronectin = magenta, self-fluorescence of columns = blue, DAPI = blue, actin = green). **e-e‴**) 3D reconstruction of the cells in 3D structures. The cells adhere to the cross struts, using the entire strut as the adhesion surface. Scaffold not depicted in e). Scale bar: 10 µm.

The supernatant was removed and the cell pellet resuspended in 5-10 ml of medium. Depending on the desired dilution, a certain volume was transferred to new cell culture flasks with pre-prepared tempered medium. The usual division ratios for NIH/3T3 cells is between 1:10 and 1:20.

After structure functionalization with fibronectin, NIH/3T3 mouse embryonal fibroblasts were seeded on the structures using a micromanipulator (aureka, aura optik GmbH) with an attached hydraulic manual microinjector (CellTram, Eppendorf). Cells were added to a 4°C CO_2 buffered F12- imaging medium (0.76 g F12 nutrient mixture (Invitrogen), 50 ml water, 25mM HEPES (Carl Roth), 1% Pen/Strep (Sigma-Aldrich), 200mM L-glutamine (Life Technologies), 10% FCS). A portion of this cell suspension was pipetted over the glass plate containing the structures, which was also coated with a F12 imaging medium (4°C) and clamped in a magnetic holder. The unheated medium reduced premature adhesion of the cells to the substrate bottom and to the glass capillary of the microinjector. The individual cells were then aspirated to a glass capillary via the microinjector by creating a negative pressure. The capillary was then conveyed over the desired structure using the micromanipulator and the cell was transferred. After all structures were occupied, the temperature was raised to 37°C to accelerate adhesion of the cells to the structures.

Protein staining was performed immunologically on fixed samples in a humidity chamber. Cells were fixed at room temperature for 10 min with 37°C tempered 4% PFA (Sigma-Aldrich) in PBS. This was followed by permeabilization of the cell membrane by washing three times with 0.1% TritonX-100 (Carl Roth) in PBS for 5 min, followed by incubation with anti-fibronectin (BD Transduction Laboratories, 1:500) for 1 h at room temperature or at 4°C. All antibodies and staining substances were diluted in 1% BSA (Bovine Serum Albumin) in PBS. This was followed by three

wash steps for 5 min each with PBS. The fluorescent secondary antibodies anti mouse AF 647 (Life Technologies, 1:400) as well as DAPI (Roth, 1:2000) and fluorescently coupled phalloidin AF 488 (Life Technologies, 1:200) were then applied for 1 h at room temperature. After another wash step with PBS, the samples were embedded in 1% n-propyl gallate (Sigma-Aldrich) in Mowiol (Hoechst) and stored at 4°C.

3D images of the cells were taken on the LSM 510 Meta (Zeiss) and the Axio Imager.Z1 with ApoTome (Zeiss) at 37°C. The 3D shapes were extracted from the actin, DAPI and fibronectin staining as triangulated meshes using Imaris (Bitplane). The experiments were executed by Mona Jaggy in the group of Martin Bastmeyer at KIT.

6.1.3 Characterization of experimentally observed shapes

The shapes of $n = 6$ cells in L-shaped or square-shaped structures spanning between two fibronectin coated cross struts were obtained experimentally. An exemplary cell can be seen in Fig. 6.1d,e). Visual inspection of the extracted cell shapes revealed remarkable similarity across all cells. Notably, the cells bridged along the free area between the beams, forming invaginated arcs - a well-established phenomenon observed for cells on both 2D microstructured surfaces and 3D structures [5, 152] and found in our simulations in Chapter 5. In some cases, we observe w-shaped invaginations due to the nucleus. Similarly, the shapes of $n = 7$ cells in V-shaped structures were obtained, see Fig. 6.1d′,e′), where we again observe invaginated arcs. In this case, the nucleus does not interfere the formation of the arc and thus we do not observe w-shaped arcs. Additionally, we obtained the shapes of $n = 3$ cells in right triangle structures, see Fig. 6.1d″,e″) and of $n = 4$ cells in equilateral triangle structures, see Fig. 6.1d‴,e‴). In these structures, the cells also adhere to the additional cross strut as compared to the L-shaped structure or the V-shaped structure respectively. In these cases, we do not find invaginated arcs as the cells fill the volume between the cross struts.

6.2 3D spherical harmonics analysis

To analyze and quantitatively compare 3D cell shapes obtained from experiments and simulations, we employ a 3D spherical harmonics analysis. Spherical harmonics form a complete set of orthonormal functions and can be used as an orthonormal basis for describing 3D shapes. This approach enables precise, translation-invariant, scale-invariant, and rotation-invariant description of 3D shapes and has been previously used to analyze biological shapes [367–371].

Following the approach in [370], we first convert the boundary shapes for simulated and experimentally observed cell shapes from Cartesian coordinates to spherical coordinates, exploiting the fact that all our shapes are star-shaped and thus can be mapped bijectively to the unit sphere. We then sample the data on a regular grid and use the Driscoll and Healy sampling theorem [372] implemented in pyshtools (version 4.10) [373] to calculate the spherical harmonics:

$$Y_l^m(\theta,\phi) = k_{l,m} P_l^m(\cos\theta) e^{im\phi}, \tag{6.1}$$

where l and m are the degree and order respectively. $k_{l,m}$ is the normalization and P_l^m are the associated Legendre polynomials. The spherical harmonics as defined in Eq. 6.1 define an orthonormal basis, thus any scalar function $f(\theta,\phi)$ on a sphere can be expressed as a sum of the spherical harmonics:

$$f(\theta,\phi) = \sum_{l=0}^{\infty} \sum_{m=-l}^{l} \hat{f}(l,m) Y_l^m(\theta,\phi). \tag{6.2}$$

Here, $\hat{f}(l,m)$ are the harmonic coefficients given by

$$\hat{f}(l,m) = k_{l,m} \int_0^{\pi} \int_0^{2\pi} e^{-im\phi} f(\theta,\phi) P_l^m(\cos\theta) \sin\theta \, d\phi \, d\theta. \tag{6.3}$$

We normalize the harmonic coefficients $\hat{f}(l,m)$ with respect to the first-order ellipsoid $\hat{f}(0,0)$ and use the normalized coefficients $\hat{f}_n(l,m)$ to calculate the rotation-invariant frequency spectrum $F(l)$ as a quantitative shape measure

$$F(l) = \sum_{m=-l}^{l} \hat{f}_n^2(l,m). \tag{6.4}$$

Now, we can calculate a measure for the difference $\Delta_{l_{\max}}$ between two shapes a and b from the corresponding frequency spectra:

$$\Delta_{l_{\max}}(a,b) = \sqrt{\sum_{l=0}^{l_{\max}} (F_a(l) - F_b(l))^2}. \tag{6.5}$$

In the subsequent analysis, we will use the first 30 degrees of the respective frequency spectra to compare shapes (Δ_{30}).

6.3 Modeling cell shape as CMC surfaces

The actin cortex is a network of actin filaments and myosin motors positioned beneath the cell membrane, which contracts the cortex and influences cell shape, as discussed in Section 2. Assuming constant tension throughout the cortex, cell shapes can be characterized as fixed-volume objects that minimize their surface area, representing an approach that does not consider mechanobiological systems inside the cell. This approach is applicable to cells in suspension, which tend to be spherical in shape. For cells on adhesive stripes, their shapes can be described as a wetting process governed by surface tensions [374]. However, a quantitative comparison between experimentally observed cell shapes and shapes obtained from the described minimal surface model has not yet been conducted to our knowledge.

Surface minimization under volume constraints leads to surfaces with constant mean curvature (CMC) [375]. To assess the validity of the isotropically contracting actin cortex imposing the shape of cells in structured environments, we perform a comparison between experimentally observed cell shapes and minimized surfaces with the same volume. The discrepancy between the observed and minimized cell shapes provides a measure of the degree to which factors beyond the actin cortex contribute to cell shape in such environments.

We employed Imaris to extract the experimentally observed shapes, and combined surface of cytoplasm and nucleus for the purpose of surface minimization, see Fig. 6.2a-a‴). To obtain the minimized surfaces, we fixed vertices of the triangulated cell shape close to the structures and used SurfaceEvolver (Version 2.70) [376] to minimize the shapes under a constant volume constraint. Upon visual inspection, we found significant differences between the experimentally observed cell shapes and the resulting minimal energy shapes for the L- and V-shaped structures, indicating that minimizing area under a volume constraint is insufficient for accurately describing cell shape in these cases. The observed cells in the scaffolds stretch between adhesive areas and maintain a roughly constant thickness, while the minimal energy surfaces form more sphere-like shapes with two thinly stretched extensions attached to the scaffold due to the imposed boundary conditions. This finding is unsurprising since spheres have the lowest surface-to-volume ratio, thus the surfaces are becoming sphere-like to minimize their surface area. For cells in the L-shaped and square scaffolds, this results in a w-type invagination. On the other hand, for cells in triangular shaped structures adhering to all three cross struts, the difference between the experimentally obtained and minimized surfaces is smaller. The surfaces are smoother, but cell-scale surface changes are not found.

Landmark values of the surfaces before and after minimization quantify the shape

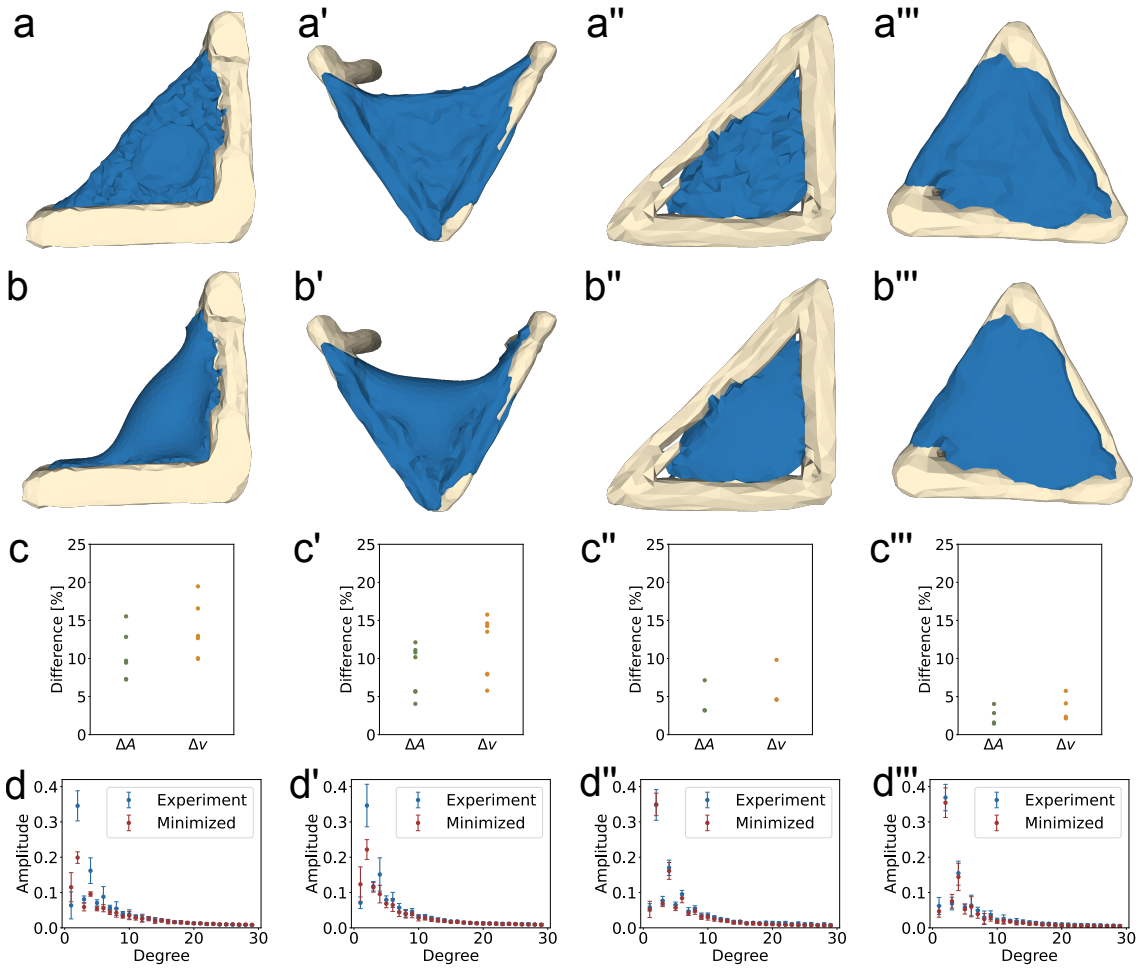

Figure 6.2: **Comparison between experimentally obtained cell shapes and their minimized surfaces. a-a‴**) The surfaces of the cells in structured environments. To minimize the cell surface, the cytoplasm and nucleus surface reconstruction were united to the cell surface. **b-b‴**) Minimized surfaces in the 3D structures. Mesh points attached to the structure were fixed during minimization. **c-c‴**) Area (ΔA) and reduced volume (Δv) differences between the experimentally observed and minimized surfaces. **d-d‴**) Frequency spectrum of the experimentally observed (blue) and minimized (red) surfaces. d) $\Delta_{30} = 0.175$. d′) $\Delta_{30} = 0.148$. d″) $\Delta_{30} = 0.026$. d‴) $\Delta_{30} = 0.031$.

differences. We compare the surface area reduction ΔA and the changes in reduced volume Δv. The differences in area and reduced volume are illustrated in Fig. 6.2c-c‴). For cells in the L-shaped structures, the surface area was reduced by (10±3)% during the minimization process on average, for the V-shaped structures the reduction was (9±3) %. Much smaller reductions were found for cells in triangular structures, cell area in the right angle triangle was reduced on average by (5±2) % and in equilateral triangles the difference is (2±1) %.

For the reduced volume v, we find similar differences. After minimization, the reduced volume of cells in L-shaped structures differed by an average of (14±3) % when compared to the reduced volume before minimization. For cells in V-shaped structures, this difference was (11±4) %, whereas for cells in right angle triangles, the average difference of Δv was found to be (6±2) % and for cells in equilateral triangles (4±1) %.

These significant variations for cells that form invaginated arcs underscore the notion that 3D cell shape in structured environments is more complex than a surface that has been minimized under a volume constraint.

To quantify these differences further, we subsequently computed the spherical harmonics coefficients of the obtained experimental and minimized shapes. To ensure that small surface fluctuations are not included in the analysis, a cutoff was applied after $l_{\max} = 30$.

The frequency spectrum of the spherical harmonics for experimentally observed and minimized shapes can be seen in Fig. 6.2d-d‴). The dipole moment of the spherical harmonics, represented by the amplitude of the first degree in the frequency spectrum, exhibits a low value. This result is anticipated, given the observed cell shape's lack of symmetry with respect to a single axis. On the other hand, the second degree of the frequency spectrum displays the highest amplitude across all observed cell shapes, corresponding to the quadrupole moment that characterizes a distribution with two perpendicular axes of symmetry. Additionally, the fourth spherical harmonic also has a pronounced peak in the frequency spectrum, representing a six-axis symmetric distribution.

With the spherical harmonics analysis of the minimized structures, we were able to quantify the difference between experimentally observed shapes and what we would expect from minimal surfaces. The difference between the average experimentally observed and minimized amplitude is $\Delta_{30} = 0.175$ for cells in L-shaped structures. For cells in V-shaped structures, we find $\Delta_{30} = 0.148$. In both cases, there is a large difference in the low degrees of the frequency spectrum. This is expected as we obtain a more spherical shape after minimization. The amplitude of the first degree

of the frequency spectrum for the minimized shapes is larger than the experimental amplitude, while the amplitudes of the second and forth degrees, which are prominent in the experimental shapes, are lower. This is as expected because of the increased sphericity of the minimized shapes. When comparing the experimentally observed cell shapes to the minimized shapes in triangular structures, the difference is much smaller; for cells in the right angle triangles, we find $\Delta_{30} = 0.026$, and for cells in equilateral triangles we find $\Delta_{30} = 0.031$. Both values are much lower than for structures with invaginated arcs, highlighting that the quality of cell shape prediction with constant mean curvature depends on the structured environment.

Together, these findings show that 3D cell shape in structured environments is not always adequately described by minimized surfaces, leading to the conclusion that a constant surface tension due to a contractile actin cortex is not enough to describe cell shape, especially for cells with invaginated arcs.

6.4 Modeling cell shape with the CPM

Similar to the simulations in Chapter 5, we employ the generalized cell types *Cytosol*, *Nucleus*, *Adhesive* and *Nonadhesive* to describe single cells in the 3D structures described Section 6.1. As we now have 3D experimental data to compare our simulations with, we use two different approaches to describe the system with the CPM.

Choosing the appropriate Hamiltonian to describe biological systems has been a longstanding question in the field. Early formulations of the Hamiltonian included an elastic volume constraint and interaction energies. In order to more accurately model cell behavior, an elastic surface constraint was added. Additionally, the nucleus can be modeled explicitly as a compartmentalized cell with an elastic constraint to ensure that the nucleus is close to the cell center of mass:

$$\begin{aligned}\mathcal{H} = &\sum_{\sigma} \lambda_{V_\tau} \cdot (V(\sigma) - V_{T_\tau})^2 + \sum_{\text{Cell, Nucleus}} \lambda_{A_\tau}(A(\sigma) - A_{T_\tau})^2 \\ &+ \sum_{<\mathbf{x},\mathbf{x'}>_N} J_{\tau(\sigma(\mathbf{x})),\tau(\sigma(\mathbf{x'}))}(1 - \delta(\sigma(\mathbf{x}), \sigma(\mathbf{x'})) \\ &+ \lambda_N(\mathbf{x}_{\text{Cell}} - \mathbf{x}_{\text{Nucleus}})^2.\end{aligned} \tag{6.6}$$

Here, the first two terms are the elastic volume and surface energies for the generalized cell types "cytoplasm" and "nucleus", where the strength of the constraints is given by λ_{V_τ} and λ_{A_τ} respectively and the target volume and area are given by V_{T_τ} and A_{T_τ}. These parameters depend on the cell type τ. The inclusion of an elastic

volume constraint in the Hamiltonian is motivated by the constant volumes of cell compartments in biological systems, and the need to model dynamics with some flexibility to avoid "lattice freezing" while ensuring that the simulated cells do not disappear, which would reduce the energy of the system but does not align with biological reality. Conversely, the elastic area constraint is not strictly required for the simulation, but its inclusion provides an additional constraint that allows more flexibility in the parameter selection of the interaction energies J [377]. The third term in the Hamiltonian represents the interaction energy at cell interfaces. It is computed by summing over all voxels $\mathbf{x}, \mathbf{x'}$ within the neighborhood N, which for $N = 1$ are the 6 directly adjacent voxels, for $N = 2$ it includes the 8 diagonally adjacent voxels and so on. If the voxels $\mathbf{x}, \mathbf{x'}$ belong to different generalized cells σ, their interaction energy J is added to the total energy of the system. The value of J can be positive or negative, and depends on the cell types of the neighboring voxels. To ensure that the nucleus remains inside the cell, an elastic constraint with strength λ_N is added between the cell center of mass $\mathbf{x}_{\text{Cell}}$ and the center of mass of the nucleus $\mathbf{x}_{\text{Nucleus}}$.

Instead of the elastic area constraint that follows from the assumption that the cell surface is constant throughout the experiment, one can describe the surface with a linear area term, which follows from the assumption that increasing the cell surface always costs energy [298, 313]:

$$\begin{aligned}\mathcal{H} = &\sum_{\sigma} \lambda_{V_\tau}(V(\sigma) - V_{T_\tau})^2 + \lambda_{A_{\text{Cell}}} A(\text{Cell}) + \lambda_{A_{\text{Nucleus}}}(A(\text{Nucleus}) - A_{T_{\text{Nucleus}}})^2 \\ &+ \sum_{<\mathbf{x},\mathbf{x'}>_N} J_{\tau(\sigma(\mathbf{x})),\tau(\sigma(\mathbf{x'}))}(1 - \delta(\sigma(\mathbf{x}), \sigma(\mathbf{x'})) \\ &+ \lambda_N(\mathbf{x}_{\text{Cell}} - \mathbf{x}_{\text{Nucleus}})^2.\end{aligned} \tag{6.7}$$

Here, the volume, interaction and nucleus surface and centering energy terms are similar to Eq. 6.6, but the elastic area energy term of the cell is replaced with a linear area energy, where the strength is determined by $\lambda_{A_{\text{Cell}}}$. Note that here, $\lambda_{A_{\text{Cell}}}$ has different dimensions compared to Eq. 6.6.

The static cell shapes used for further analysis are obtained by averaging over the last 500 MCS of the 2000 MCS simulation.

The cellular Potts model can be used to simulate the behavior of cells in complex geometries, such as the scaffolds used in the experiments described above. By tuning the parameters of the model, it is possible to simulate cell shapes that are similar to those observed experimentally. Parameters influencing the cell shape are the

surface energy strength λ_{A_τ}, which represents the energy required to change the cell surface area, as well as the interaction energy between the cytoplasm and the medium $J_{\text{cytoplasm,medium}}$, which represents the energy required to move a cell in the surrounding medium. The neighbor order N is a parameter that determines the extent of the interactions between neighboring voxels. Choosing an appropriate neighbor order is crucial in cellular Potts model simulations, as it defines how much of the surrounding affects the cell, while ensuring that the neighborhood remains smaller than the cell [353], as we discussed in Chapter 5.

Other parameters do not change the cell shape as long as their value is chosen within a reasonable range. The volume parameters λ_{V_τ} and V_{T_τ} are used to ensure that the volume of the cytoplasm and the nucleus stay close to the target volume V_{T_τ} throughout the simulation, however changing these parameters within an appropriate range does not change the cell shape. The interaction parameters between cytoplasm and scaffold, as well as cytoplasm and nucleus, are chosen to ensure the cytoplasm adheres to the scaffold and the nucleus stays inside the cytoplasm. The simulation temperature is fixed at $T = 100$ throughout the simulations. All parameters used in the simulation can be found in Table A.5.

In the following, we will discuss the relevant CPM parameters and their effect on cell shape. We focus on cells in L-shaped structures in an effort to improve the shape predictions obtained from surface area minimization. We will optimize the parameters for cells in L-shaped structures and use the parameters to simulate cells in V-shaped and triangular structures.

6.4.1 Impact of the neighbor order on cell shape

In Fig. 6.3, the measure of shape difference Δ_{30}, as introduced in Eq. 6.5, between the experimentally observed cell shapes and the cell shapes simulated with the elastic area Hamiltonian (Eq. 6.6) for varying neighbor order N and interaction energy $J_{\text{medium,cytoplasm}}$ can be seen. Remarkably, for a large parameter range of $J_{\text{medium,cytoplasm}}$ and intermediate neighbor order N, significantly lower values of Δ_{30} are found compared to the constant mean curvature shapes discussed in the previous section.

The neighbor order parameter has the most significant effect on cell shape, see Fig. 6.3. When only the nearest neighbors are considered in the calculation of the interaction energy ($N = 1$), then the cell partially detaches from the scaffold due to a reduced energy gain from cytoplasm-scaffold interactions. Additionally, both the cytoplasm and nucleus become more spherical.

For intermediate neighbor orders, $4 \leq N \leq 10$, the simulated cell shapes resemble

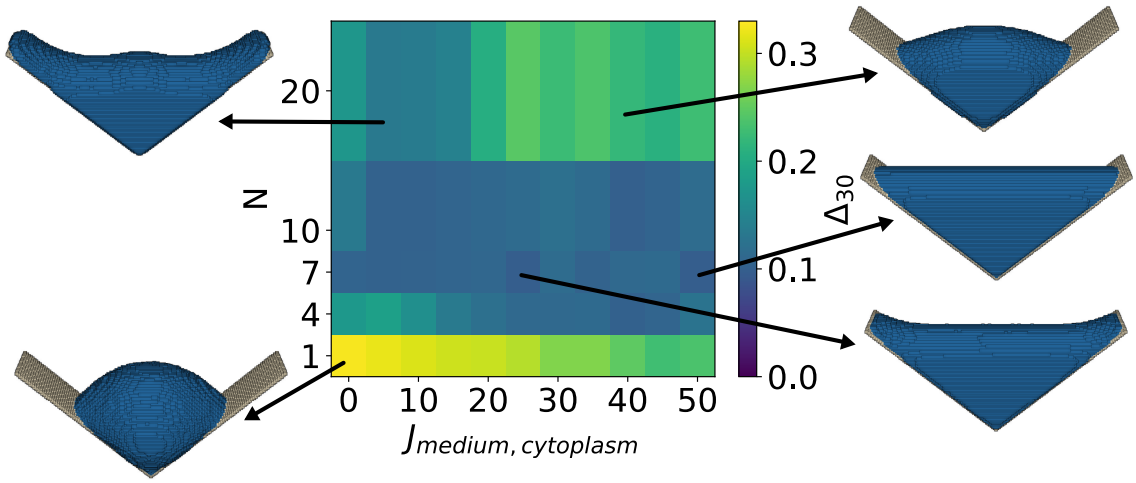

Figure 6.3: **Cell shape difference Δ_{30} as a function of neighbor order and interaction energy.** The neighbor order N defines the set of neighboring lattice sites that interact with a given lattice site, and the interaction energy $J_{\text{medium,cytoplasm}}$ defines the interaction strength between the cytoplasm and the surrounding medium. Simulated cell shapes for exemplary parameter choices are presented. The minimum cell shape difference $\Delta_{30} = 0.097$ is found for $N = 7$ and $J_{\text{medium,cytoplasm}} = 50$, the corresponding cell shape is depicted on the bottom right. Parameters used in the simulation can be found in Table A.5.

the experimentally observed shapes for a large parameter range of the interaction energy $J_{\text{medium,cytoplasm}}$, leading to low values of Δ_{30}, with the minimum being at $\Delta_{30} = 0.097$, for $J_{\text{medium,cytoplasm}} = 50$ and $N = 7$.

Increasing the neighbor order further to $N = 20$ results in shapes that deviate more from the experimentally observed cell shapes. When the interaction energy $J_{\text{medium,cytoplasm}}$ is low, the shape becomes w-shaped and resembles that of minimized surfaces because the energy gain from cytoplasm-scaffold interactions is large due to the high neighbor order. At the same time, the remaining cytoplasm volume reduces its energy by becoming spherical, leading to a w-shape. However, when the interaction energy $J_{\text{medium,cytoplasm}}$ is sufficiently increased, the cost of a less spherical shape becomes higher than the gain from the cytoplasm-scaffold interaction, resulting in more spherical shapes and increasing the value of Δ_{30} again.

As the minimum of Δ_{30} is reached for $N = 7$, we fix the neighbor order to this value in the following simulations.

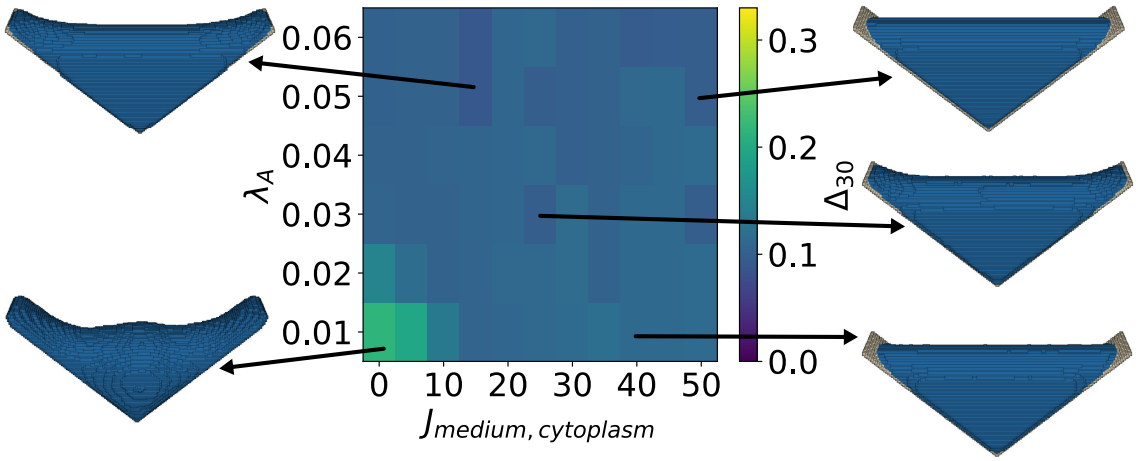

Figure 6.4: **Cell shape difference Δ_{30} with elastic area energy (Eq. 6.6).** Difference between the experimentally observed cell shapes and simulated cell shapes as a function of surface energy constraint λ_A and interaction energy $J_{\text{medium,cytoplasm}}$. Simulated cell shapes for exemplary parameter choices are presented. The minimum cell shape difference $\Delta_{30} = 0.090$ is found for $J_{\text{medium,cytoplasm}} = 15$ and $\lambda_A = 0.05$, the corresponding simulated cell is depicted on the top left. Parameters used in the simulation can be found in Table A.5.

6.4.2 Linear vs. elastic surface area energy

One of the longstanding questions in cellular Potts type simulations is the selection of the appropriate Hamiltonian. Specifically, when it comes to surface area, the two commonly used Hamiltonians are either based on the assumption that the surface of a cell is approximately constant, thus describing the area energy with an elastic constraint, see Eq. 6.6, or that increasing surface area always costs energy for the cell, leading to a linear area energy, see Eq. 6.7. Comparing simulated cells with experimentally observed cell shapes allows for the direct comparison between the two approaches. Cell shapes simulated with either Hamiltonian, shown in Fig.6.4 for elastic area energy and in Fig.6.5 for linear area energy, closely resemble the experimentally observed cell shapes for a wide range of parameter values, vastly outperforming the minimized cell shapes.

The cell shapes obtained with the elastic area Hamiltonian (see Eq. 6.6 and Fig. 6.4) are visually close to the experimentally observed cell shapes for a large parameter range. The minimum $\Delta_{30} = 0.090$ is found for $J_{\text{medium,cytoplasm}} = 15$ and $\lambda_A = 0.05$. Similar cell shapes are obtained for a large parameter range. Increasing the interaction energy $J_{\text{medium,cytoplasm}}$ reduces the interface between cytoplasm and the medium, resulting in partially occupied scaffolds. For a low elastic area constraint λ_A and

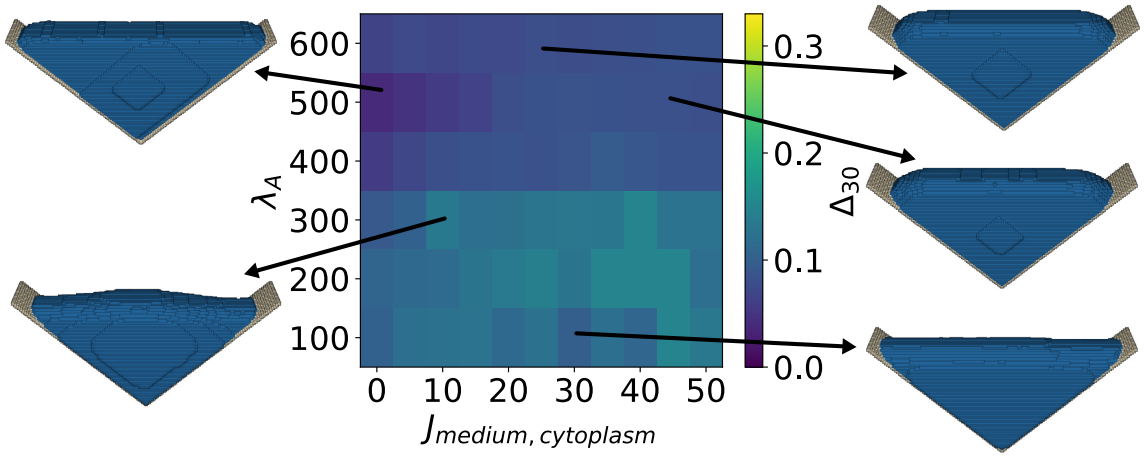

Figure 6.5: **Cell shape difference Δ_{30} with linear area energy (Eq. 6.7).** Difference between the experimentally observed cell shapes and simulated cell shapes as a function of surface energy constraint λ_A and interaction energy $J_{\text{medium,cytoplasm}}$. Simulated cell shapes for exemplary parameter choices are presented. The minimum cell shape difference $\Delta_{30} = 0.039$ is found for $J_{\text{medium,cytoplasm}} = 0$ and $\lambda_A = 500$, the corresponding simulated cell is depicted on the top left. Parameters used in the simulation can be found in Table A.5.

interaction energy $J_{\text{medium,cytoplasm}} = 0$, the simulated cell shape visually differs from the experimentally observed cells and resembles a w-shape again.

The minimum found with the linear area Hamiltonian in Eq. 6.7 is even smaller, with $\Delta_{30} = 0.039$ for $J_{\text{medium,cytoplasm}} = 0$ and $\lambda_A = 500$, see Fig. 6.5. The simulated cell shape that resembles the experiments best is triangular shaped and without invaginated arcs, however the thickness to length ratio of the cell closely resembles that of the experimentally observed shapes. Surprisingly, the simulated cell shape resembles the experimentally observed shapes best when the interaction energy $J_{\text{medium,cytoplasm}} = 0$. For a cell that is surrounded by medium only, increasing $J_{\text{medium,cytoplasm}}$ has a similar effect to a linear area constraint, as the surface of the cell corresponds to the interaction area between cell and medium. In the case of structured environments, the interaction energy only acts on part of the cell surface, while the whole cell surface is relevant for the area energy. For the linear area Hamiltonian, the scaffold is always only partially covered as increasing the cytoplasm surface area always costs energy.

It is surprising that the surface corresponding best to the experiments is found for the linear area Hamiltonian simulation, as this is the simulation with the fewest parameters, specifically there are less parameters compared to the elastic area Hamiltonian, where the target surface area of the cell is predefined according to its

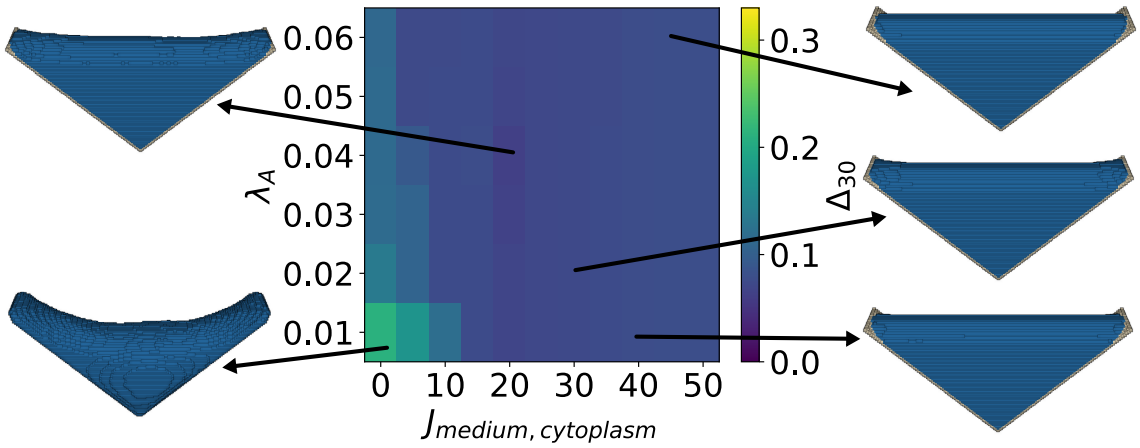

Figure 6.6: **Cell shape difference Δ_{30} with elastic area energy (Eq. 6.6) without nucleus.** Difference between the experimentally observed cell shapes and simulated cell shapes without nucleus as a function of surface energy constraint λ_A and interaction energy $J_{\text{medium,cytoplasm}}$. Simulated cell shapes for exemplary parameter choices are presented. The minimum cell shape difference $\Delta_{30} = 0.063$ is found for $J_{\text{medium,cytoplasm}} = 20$ and $\lambda_A = 0.04$, the corresponding simulated cell is depicted on the top left. Parameters used in the simulation can be found in Table A.5.

experimental value.

6.4.3 Influence of the nucleus on cell shape

To determine the influence of the nucleus on the cell shape, we compare simulated cell shapes without a nucleus, which can be seen in Fig. 6.6 and Fig. 6.7, with the previous simulation results, where we represented the nucleus as a cellular compartment with an elastic volume and area constraint, interaction energies and a nucleus centering constraint.

Notably, the simulation without explicit representation of a nucleus results in simulated shapes that are closer to the experimentally observed shapes for the elastic area constraint, compare Fig. 6.4 and Fig. 6.6. Visually, a difference can be seen for low elastic area constraint λ_a and interaction energy $J_{\text{medium,cytoplasm}}$, where the removal of the nucleus leads to an invaginated arc instead of a w-shaped spanning. In most other cases, the reduction of Δ_{30} is due to a thickness increase of the cell which was prevented previously due to the high interaction energy penalty between the nucleus and the medium $J_{\text{medium,nucleus}}$.

Similarly, Δ_{30} is below 0.1 for all tested parameters in the simulation without nucleus and with linear area energy, see Fig. 6.7. The minimum $\Delta_{30} = 0.060$ is

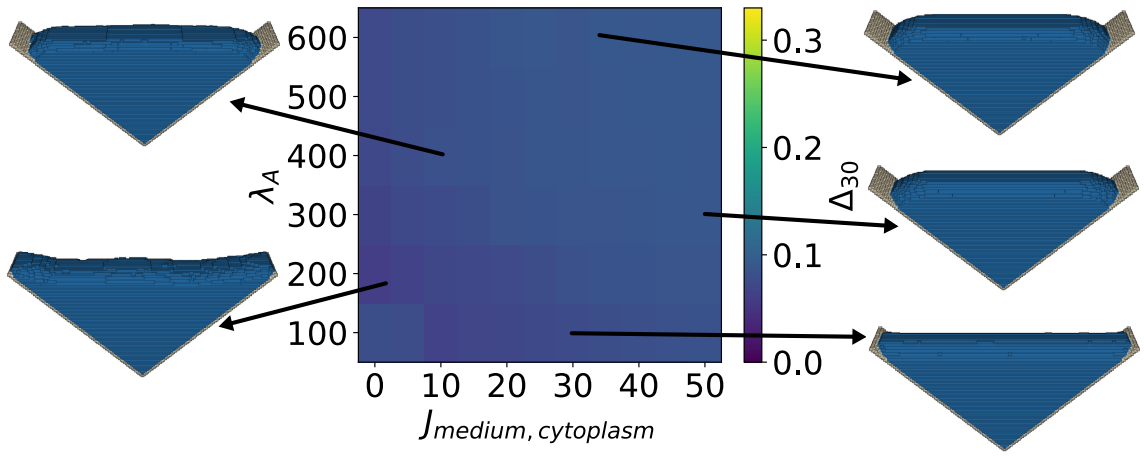

Figure 6.7: **Cell shape difference Δ_{30} with linear area energy (Eq. 6.7) without nucleus.** Difference between the experimentally observed cell shapes and simulated cell shapes without nucleus as a function of surface energy constraint λ_A and interaction energy $J_{\text{medium,cytoplasm}}$. Simulated cell shapes for exemplary parameter choices are presented. The minimum cell shape difference $\Delta_{30} = 0.060$ is found for $J_{\text{medium,cytoplasm}} = 0$ and $\lambda_A = 200$, the corresponding simulated cell is depicted on the bottom left. Parameters used in the simulation can be found in Table A.5.

found for $J_{\text{medium,cytoplasm}} = 0$, and $\lambda_A = 200$. Here, we find an invaginated arc and full adhesion to the scaffold. In accordance with the simulations with nucleus, we find that the simulated shape best corresponding to the experiment is found for $J_{\text{medium,cytoplasm}} = 0$. Increasing both the interaction energy and the area constraint leads to partial uncovering of the scaffold and evaginated arcs.

The small difference between simulated cell shapes with and without nucleus lead us to the conclusion that for cells in L-shaped structured environments, the cytoskeleton deforms the spherical nucleus such that it is not a determining factor for the overall cell shape, even though it is much stiffer than the cytoplasm.

6.4.4 Application to different environment geometries

Cells with nuclei in V-shaped, right angle and equilateral triangle structures were simulated with the parameter set that performed best for the L-shaped structure (linear area Hamiltionian Eq. 6.7, $\lambda_{\text{A}} = 500$, $J_{\text{medium,cytoplasm}} = 0$), see Fig. 6.8. For the right angle triangular structure, we find good agreement between the experimentally observed shapes and the simulation with $\Delta_{30} = 0.053$. However, for the equilateral triangle and the V-shaped structure, which differ more from the L-shaped structure than the isosceles right triangle, we find $\Delta_{30} = 0.141$ and $\Delta_{30} = 0.136$.

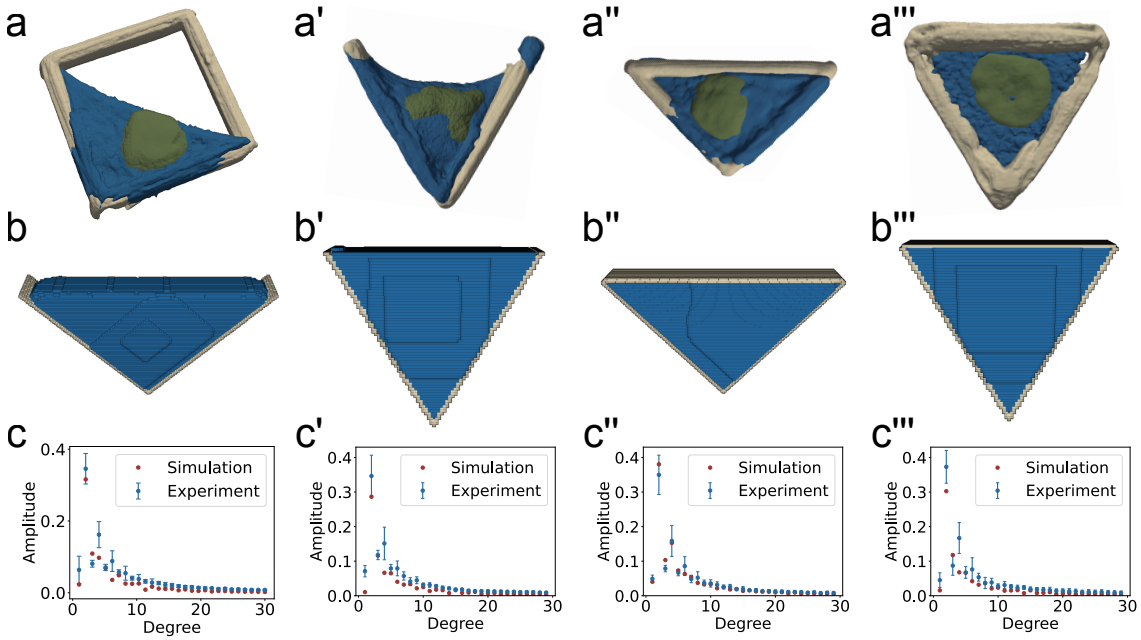

Figure 6.8: **Experimental and simulated cell shapes in different environment geometries and corresponding frequency spectra.** **a-a‴**) Reconstruction of the experimental data from cells in L-shaped, V-shaped, right-angle triangular and equilateral triangular shaped structures. **b-b‴**) Simulated cell shapes in structured environments. **c-c‴**) Frequency spectra of the experimental and simulated cell shapes. c) $\Delta_{30} = 0.039$, c′) $\Delta_{30} = 0.136$, c″) $\Delta_{30} = 0.053$, c‴) $\Delta_{30} = 0.141$. Parameters used in the simulation can be found in Table A.5.

These differences show that it is difficult to find universal parameters for the CPM that accurately predict cell shape in different structured environments.

6.5 Discussion

Due to recent technical advances, an increasing number of experimental data is three-dimensional. This adds to the need for 3D single cell models to explain and predict cell shape. In this chapter, we compared different approaches to describe cell shape in 3D. We used surface minimization and the CPM to investigate how much simulated shape predictions differ from experimentally observed cell shapes in precisely defined environments. We find that the predicted constant mean curvature shapes agree well with experimentally observed shapes if the cell does not form invaginated arcs and stress fibers. Larger differences were found for cell shapes in L- and V-shaped structures.

Better cell shape prediction was possible with the CPM, independent of the Hamiltonian choice and specific parameter values. Invaginated arcs form without explicitly simulating stress fibers and the high quadrupole moment in the spherical

harmonics is correctly predicted. There are multiple factors that contribute to the better performance of CPM simulations compared to surface minimization models. By selecting the neighbor order in the CPM, one can define how local the interaction energy is. This influences to which extent the surface minimization can occur, or may even facilitate surface extension between two general cell types, if the interaction energy is negative. A cell described by a Hamiltonian with volume, area, interaction and nucleus centering energies leads to more complex shapes that better resemble experimental results.

Even though CPM simulations better capture experimental cell shapes, it should be noted that there are some systematic differences between the simulated and experimental shapes. For instance, cells in experiments have more variability in their shapes and attach only partially to the structures compared to the smooth shapes predicted by the CPM. Additionally, the reconstruction of cell shape in experiments using actin staining is only an approximation, and may introduce some degree of error in the obtained cell shapes. Actin stress fibers often span between adhesive sites, however their impact has not been accounted for in the simulations and could be included in the future using the methods described in Section 5.3.

The best agreement between experimental and simulated cell shape was found with the linear area Hamiltonian, despite the fact that less parameters are used in this simulation. The effect of the nucleus on cell shape is negligible in this setting, as the nucleus is strongly deformed by the cytoskeleton. In the future, these results could be used for rational scaffold design which can then be implemented with additive manufacturing methods like the 3D laser nanoprinting used here.

7 Modeling optic vesicle evagination in organoids

7.1 Optic cup formation in vivo and in vitro

The development of the vertebrate eye is a remarkable process that involves the precise orchestration of cellular events leading to the formation of a complex 3D structure, which is essential for vision. One critical stage in eye development is the formation of the optic cup, which evaginates from the prospective brain tissue and later gives rise to the retina, the light-sensitive tissue which is responsible for capturing light signals and transmitting visual information to the brain [378]. Understanding the mechanisms underlying optic cup formation is crucial for understanding the process of eye development.

In vivo, optic cup formation occurs during early embryonic development, at the same time as the salivary gland and the lung. The successful evagination of the optic vesicle requires patterning and cell reorganization, processes where many regulatory networks such as Wnt are important [379]. The optic vesicle invaginates to form a bilayered structure known as the optic cup, see Fig. 7.1. The outer layer of the optic cup eventually differentiates into the retina pigmented epithelium (RPE), while the inner layer gives rise to the neural retina. The mechanical processes that lead to the optic cup evagination are not yet understood.

To better understand the mechanical processes behind the optic cup formation and provide a more accessible experimental system, researchers have developed three-dimensional organoid models of optic cup formation [380]. As discussed in Section 3.3, organoids are self-organizing structures derived from stem cells and can mimic the complexity and organization of specific tissues. Eikaru and colleagues managed to grow organoids that show remarkable self-organization by differentiating pluripotent stem cells into optic vesicle-like structures that subsequently invaginate and develop into an optic cup-like structure. The organoids are in 3D suspension culture with ECM components such as Matrigel [381], which are little external cues compared to the in vivo system, where much more extrinsic input is given to the developing eye, compare Fig. 7.1.

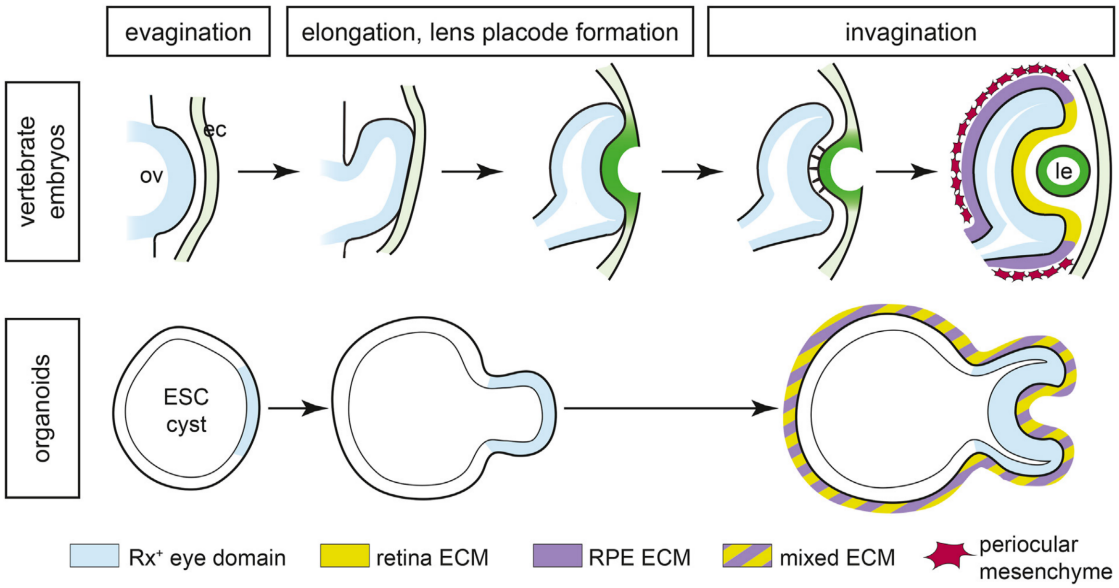

Figure 7.1: **Optic cup morphogenesis in vertebrate embryos and organoids.** In vertebrate embryos, Rx cells (blue) form the evaginating vesicle. Then, the optic vesicle folds due to cell shape changes and external cues and the surface ectoderm (light green) gives rise to the lens (dark green). In organoids, the evagination and invagination processes were observed, where the only extrinsic cue was the mixed ECM (yellow, purple). Reproduced with permission [378], 2021, Elsevier.

Optic cup organoids offer several advantages for studying eye development. They provide a controlled and reproducible system to investigate the cellular and molecular mechanisms underlying optic cup formation. Researchers can manipulate various signaling pathways, gene expression patterns, and the local microenvironment to better understand the processes involved in optic cup morphogenesis.

7.2 Optic vesicle morphogenesis in medaka retinal organoids

To better understand the optic cup formation, Zilova and colleagues were the first group to derive organoids from medaka and zebrafish primary embryonic pluripotent cells [382]. Fish organoids allow for high throughput experiments, as optic vesicle formation and the onset of retina differentiation are observed within 4 days of culture. Similar to mouse and human retinal organoids, cells were placed in U-shaped low adhesive wells in suspension with low serum concentration. Laminin-rich Matrigel was added after 1 day, when the cells had already formed aggregates. Then, starting on day 2, neuroepithelial structures and lumens inside the aggregate formed. Because

of this complex internal structure, the aggregates are then considered to be organoids.

The transcription factor Rx3 is the earliest known retina-specific gene that is expressed, and in Rx3-null mutants the optic vesicle does not develop. It is therefore used to visualize the onset of retinal differentiation with a transgenic reporter line, that leads to the expression of green fluorescent protein (GFP) under the control of the Rx3 regulatory elements. Compared to the embryo, the onset of Rx3 expression is 2-3 h later in the organoid, which is the time it takes for the cells to aggregate. However, when cell aggregation was prevented by gentle rocking, GFP-expressing clusters were observed after 24 h. Even isolated single primary pluripotent stem cells expressed GFP, leading to the conclusion that the onset of Rx3 expression is genetically timed and independent of external cues. Cells express Rx3 even in the absence of Matrigel, while the neuroepithelial structures only form in the presence of Matrigel [382].

To investigate the optic vesicle formation, Zilova and colleagues focused on medaka organoids. In large organoids (aggregates with 1000-2000 cells), a continuous layer of neuroepithelium forms at the periphery of the organoid, but no optic vesicles form, see Fig. 7.2a). On the other hand, in small organoids derived from aggregates of less than 1000 cells, 1-4 optic vesicle-like domains form, compare Fig. 7.2a-c), with a similar average size but greater variance compared to the optic vesicles in medaka embryos. In these small organoids, cells differentiated to retinal and RPE lines in regions of the optic vesicle and a general neuronal marker as well as a forebrain marker were expressed in non-retinal domain regions of the organoid. With life imaging, Zilova and colleagues observed cells as freely diffusive particles until 34 h after aggregation, when Rx3-expressing cells moved from their random position inside the aggregate with an estimated speed of 0.413-0.479 µm/ min towards optic vesicle-forming regions. Life images of the optic vesicle formation can be seen in Fig. 7.2d). At the same time, about 49% of cells that are initially located at the cell periphery move towards the center of the organoid [382].

In the absence of Matrigel, Rx3-expressing cells move towards the aggergate surface but do not form optic vesicles. The main component of Matrigel is the ECM protein laminin-1, which has been shown to be important for cell polarization and epithelial organization in optic vesicle morphology in zebrafish. Indeed, after knockout of laminin-1 and in laminin mutants, eye field cells have a rounded and unstable cell shape [383].

Recently, Lucie Zilova and Venera Weinhardt focused on the Rx3-expressing cell distribution in different sized organoids, see Fig. 7.2e). As discussed in [382], Rx3-expressing cells are distributed randomly in organoids derived with less than 1000

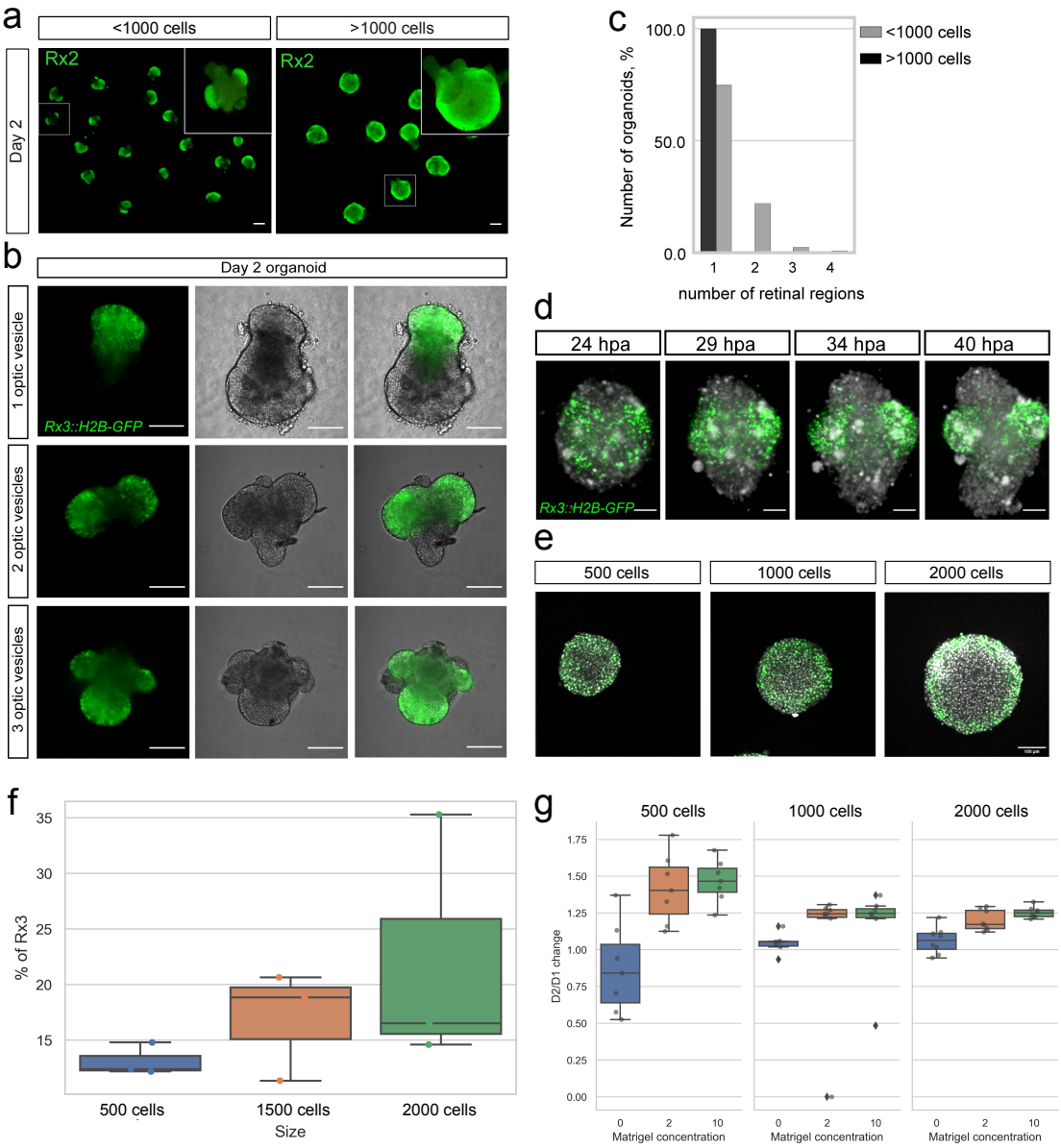

Figure 7.2: **Experimental results of optic vesicle formation in medaka organoids.** **a**) Fluorescence image of day 2 organoids from aggregations with <1000 cells and >1000 cells. Optic vesicles only form for small organoids (<1000 cells). **b**) Fluorescence and bright field images and their overlay of small organoids on day 2 forming 1-3 optic vesicles. **c**) Percentage of organoids that form 1-4 individual retinal regions (large organoids: n=35, small organoids: n=123). **d**) In vivo time-lapse images from 24-40 h post aggregation of optic vesicle-like structure formation. **e**) Rx3-expressing cell distribution in organoids derived from aggregates with 500, 1000 and 2000 cells. **f**) Percentage of Rx3-expressing cells in organoids derived from aggregates with 500, 1500 and 2000 cells. **g**) Organoid volume change between day 1 and day 2 post aggregation depending on Matrigel amount added at day 1 for organoids derived from aggregates with 500, 1000 and 2000 cells. Scale bars: 100 µm.
Images a-d) Reproduced with permission [382], 2021, eLife. Images e-g) courtesy of Venera Weinhardt.

cells. Surprisingly, in large organoids derived from 2000 cells, Rx3-expressing cells are predominantly found at the periphery of the organoid, indicating that there is an external cue suppressing retina differentiation for cells at the center of the organoid. We speculate that this distribution could be a result of the increased pressure at the organoid center or due to reduced access to nutrients. At the same time, even though Rx3-expressing cells are only found at the periphery of the organoid, the fraction of Rx3-expressing cells is increasing with the organoid size, see Fig. 7.2f).

Additionally, Lucie Zilova and Venera Weinhardt varied the concentration of Matrigel that is added to the organoids after 1 day, see Fig. 7.2g). While the addition of Matrigel is necessary for organoid growth independent of their size, in agreement with [382], the amount of Matrigel added does not seem to affect the growth of the organoids of different sizes.

7.3 Simulating vesicle formation in organoids

7.3.1 Differential adhesion model with ECM interaction

The CPM was invented to describe cell sorting [16, 329], an important process reminiscent of immiscible liquids that occurs for example during epithelial-mesenchymal transitions in developing embryos. Cells of different types separate similar to immiscible liquids due to different surface and interfacial tensions, which arise from different expression levels of cell adhesion molecules and the dynamic rearrangement of cell-cell contacts [384]. The differential adhesion hypothesis states that the self-organization of tissue is primarily driven by differences in the adhesive properties between cells rather than specific molecular signaling pathways, which is why the CPM is a great method to model such processes.

It is currently not known what leads to the retina cell sorting in embryos and organoids, and processes beyond tension differences might play an important role. Active migration and cell signaling could be important during retina cell sorting. However, we know from experiments that the sorting process is successful independent of Matrigel presence, but vesicle evagination is only observed in organoids suspended in Matrigel. Additionally, there is experimental evidence that Rx3-expressing cells interact with the Matrigel protein laminin [383]. Together, this leads us to an extended differential adhesion model that includes Matrigel as an non-cellular environment with cell type-specific interaction energies to describe the observed phenomena during organoid morphogenesis.

The most important parameters for the CPM simulation of the optic cup morphogenesis are therefore the interaction energies between the different generalized cell

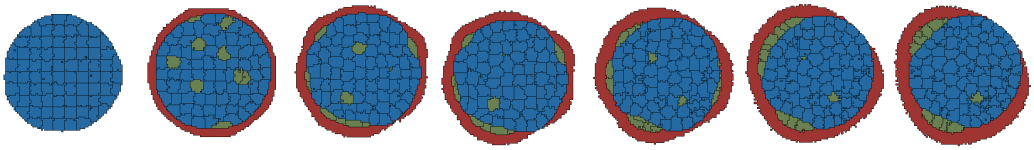

Figure 7.3: **Simulated optic vesicle evagination in an aggregate with 500 cells.** Cross section snapshots at 90 MCS, 110 MCS, 200 MCS, 400 MCS, 900 MCS, 1400 MCS, 1980 MCS. Simulation parameters can be found in Table A.6.

types *Retina*, *Other* and *Matrigel*. Following differential adhesion simulations [329], the interaction energy $J_{\text{other, other}}$ is the lowest to ensure condensing of these cells at the center of the organoid. For the Matrigel-Rx3-cells interaction that leads to the formation of optic vesicles, their interaction energy $J_{\text{retina, matrigel}}$ is lower than the interaction energy between other cells and the Matrigel $J_{\text{other, matrigel}}$, which has the same value as the interaction energy between Rx3-cells and other organoid cells $J_{\text{retina, other}}$. All interaction energy values can be found in Table A.6.

The Hamiltonian used for the optic vesicle morphogenesis has therefore the following terms:

$$\begin{aligned}\mathcal{H} = &\sum_{\sigma} \lambda_{V_\tau} \cdot (V(\sigma) - V_{T_\tau})^2 + \sum_{\sigma} \lambda_{A_\tau} \cdot (A(\sigma) - A_{T_\tau})^2 \\ &+ \sum_{<\mathbf{x},\mathbf{x'}>_N} J_{\tau(\sigma(\mathbf{x})),\tau(\sigma(\mathbf{x'}))}(1 - \delta(\sigma(\mathbf{x}), \sigma(\mathbf{x'})).\end{aligned} \tag{7.1}$$

Here, the first two terms are the elastic volume and surface energies, where the strength of the constraints is given by λ_{V_τ} and λ_{A_τ} respectively and the target volume and area are given by V_{T_τ} and A_{T_τ}. These parameters depend on the cell type τ. The last term describes the interaction energies between the generalized cell types for voxels up to neighbor order N.

The simulation runs for 2000 MCS, and the cells in the aggregate are initialized as identical cubes of cell type *Other* within a predefined radius, see Fig. 7.3. During the first 100 MCS, the system equilibrates and becomes spherical. Then, 15% of the cells become *Retina* cells. For small organoids (<1000 cells), the cells are chosen randomly, but neighboring cells of *Retina* cells are prevented from changing to *Retina* cells as well, leading to the checkerboard initialization that is observed in experiments. For large organoids, all cells that are at the periphery of the organoid become *Retina* cells. At the same time step as the cell type change, Matrigel is added to the simulation as a layer enclosing the organoid. Matrigel is modeled as a generalized cell type with target volume and target surface area given by the initial volume and surface area.

Then, the system evolves for 1900 MCS and the final shape of the organoid can be analyzed.

7.3.2 Influence of Matrigel on optic vesicle evagination

To simulate the optic vesicle formation, we use the Hamiltonian in Eq. 7.1 and simulate cell aggregates with 500 and 1000 cells with different amounts of Matrigel. The results can be seen in Fig. 7.4 as 2D cross sections and 3D images, as well as histograms with the number of retinal regions found in the simulated organoids from 10 simulations each. We consider more than 10 neighboring *Retina* cells a retinal region.

We know from experiments, that cell aggregates grown in suspension in absence of Matrigel do not form optic vesicles, and in our simulation we find similar distributions, see Fig. 7.4. Most *Retina* cells in aggregates with 500 and 1000 cells move towards the aggregate surface, but do not cluster together to form retinal regions. We do not find complete sorting, as some *Retina* cells remain close to the aggregate center. The few retinal regions found in these aggregates are at the center of the aggregate and not at its periphery. At the end of the simulation, the aggregates are remarkably spherical and we do not observe the typical shapes of organoids with optic vesicles.

In contrast, we find shapes that resemble those of organoids with optic vesicles if we simulate the aggregates with a layer of Matrigel with a volume V_{M} of 30% of the organoid volume V_{O}, compare Fig. 7.4. In simulations with *Matrigel*, we increase the interaction energy $J_{\mathrm{retina,\ medium}}$ to ensure *Retina* cells adhere to *Matrigel*. Especially for small organoids with 500 cells, we find 2-4 retinal regions in the organoids, while organoids with 1000 cells form up to 5 retinal regions. Not all *Retina* cells move to the organoid periphery, but compared to the simulation without Matrigel, the *Retina* cells inside the organoid are fewer. *Retina* cells in the retinal regions become elongated and polarized, similar to what is observed experimentally. A significant difference between the simulated organoids and the experiments is the absence of simulated organoids with one retinal region.

From the experimental results presented in Fig. 7.2g), we know that presence of Matrigel is relevant for organoid development, however the amount of Matrigel seems to be irrelevant for organoid growth. It is currently unclear if the amount of Matrigel present has other effects on organoids, such as the number of retinal regions per organoid. In our simulations, we implement that the surrounding Matrigel layer leads to optic vesicle formation because the interaction energy $J_{\mathrm{retina,\ matrigel}}$ is lower than $J_{\mathrm{other,\ matrigel}}$ and $J_{\mathrm{other,\ retina}}$. We therefore tried reducing the number of retinal regions by increasing the amount of Matrigel in the simulation.

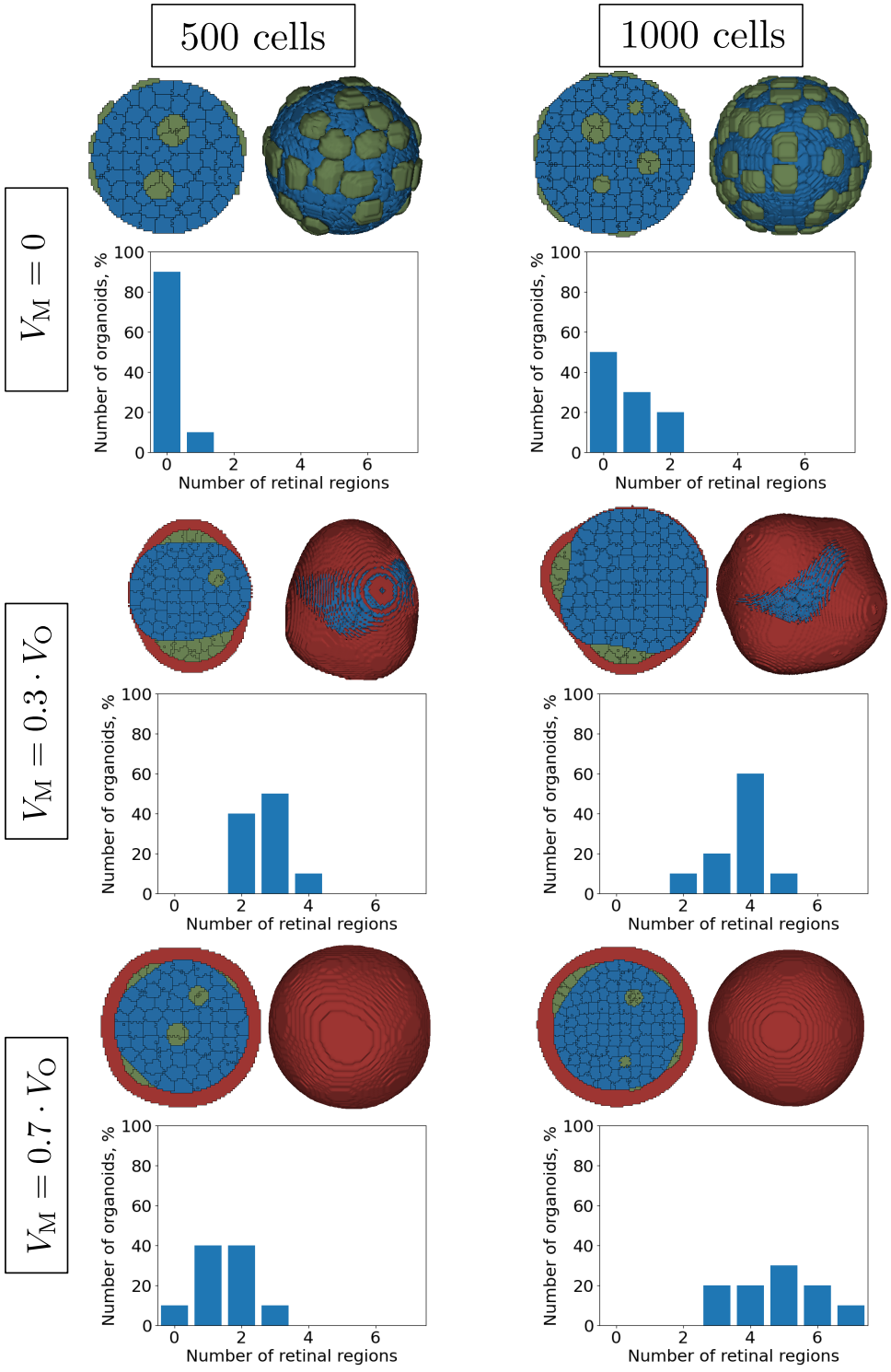

Figure 7.4: **Simulation results for small organoids with 500 and 1000 cells with different amounts of Matrigel.** *Retina* cells are depicted in green, *Other* cells in blue and *Matrigel* in red. Each histogram shows the number of retinal regions, which are defined as clusters of more than 10 *Retina* cells, for 10 simulations. Simulation parameters can be found in Table A.6.

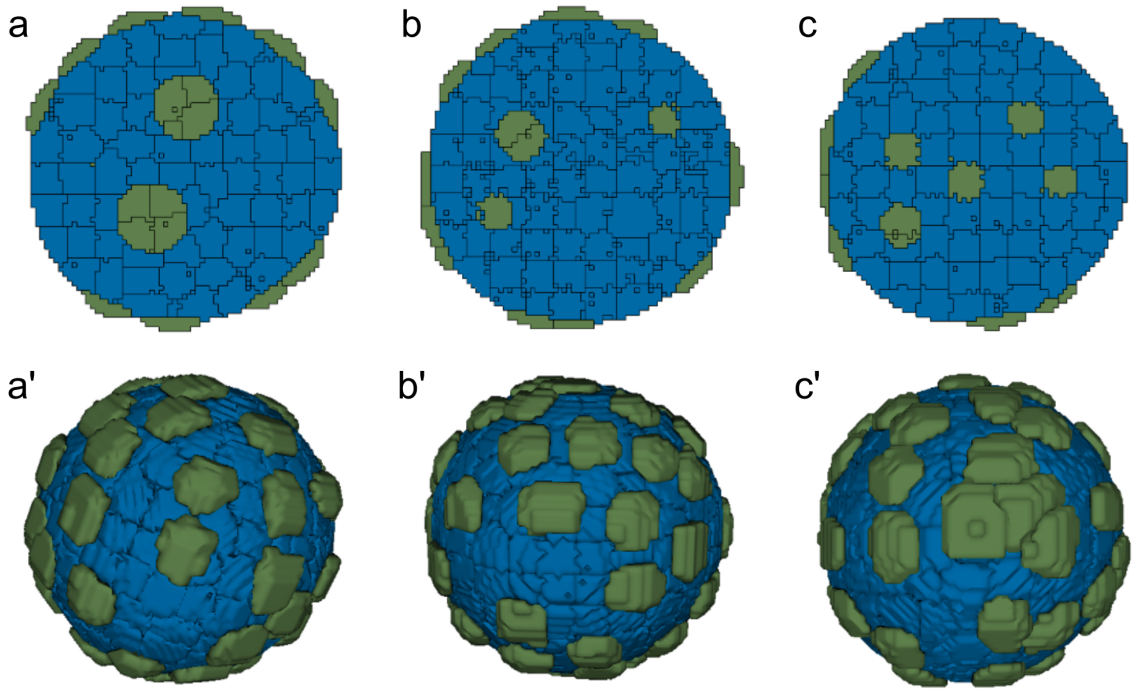

Figure 7.5: **2D cross-section and 3D images of simulations with 500 cells without Matrigel under increasing pressure. a,a′**) Simulation with no pressure. **b,b′**) Simulation with low pressure. **c,c′**) Simulation with high pressure. All simulation parameters can be found in Table A.7.

For organoids with 500 cells, we find a reduced number of retinal regions when increasing the Matrigel volume, however for organoids with 1000 cells, the number of retinal regions increases with the increased Matrigel volume, see Fig. 7.4. However, the observed organoid shapes are again more spherical, due to the surrounding Matrigel layer. Here, the Matrigel layer is remains a thick layer and does not break into smaller parts shielding the retinal regions on the organoid periphery as observed for organoids with smaller volume. Additionally, the sorting process is again incomplete, with clusters of *Retina* cells forming on the inside of the organoid.

7.3.3 Influence of pressure on optic vesicle evagination

To ensure that the observed vesicle evagination is due to the different interaction energies in the CPM simulation and not due to pressure of the Matrigel layer, we simulate organoids without the addition of Matrigel for different pressures exerted on the aggregates with 500 cells. The results can be seen in Fig. 7.5.

For simulations with no pressure, see Fig. 7.5a,a′), we obtain spherical organoids which are partially sorted, compare also Fig. 7.4. Most *Retina* cells move towards the organoid surface but do not form optic vesicles. *Retina* cells inside the organoid

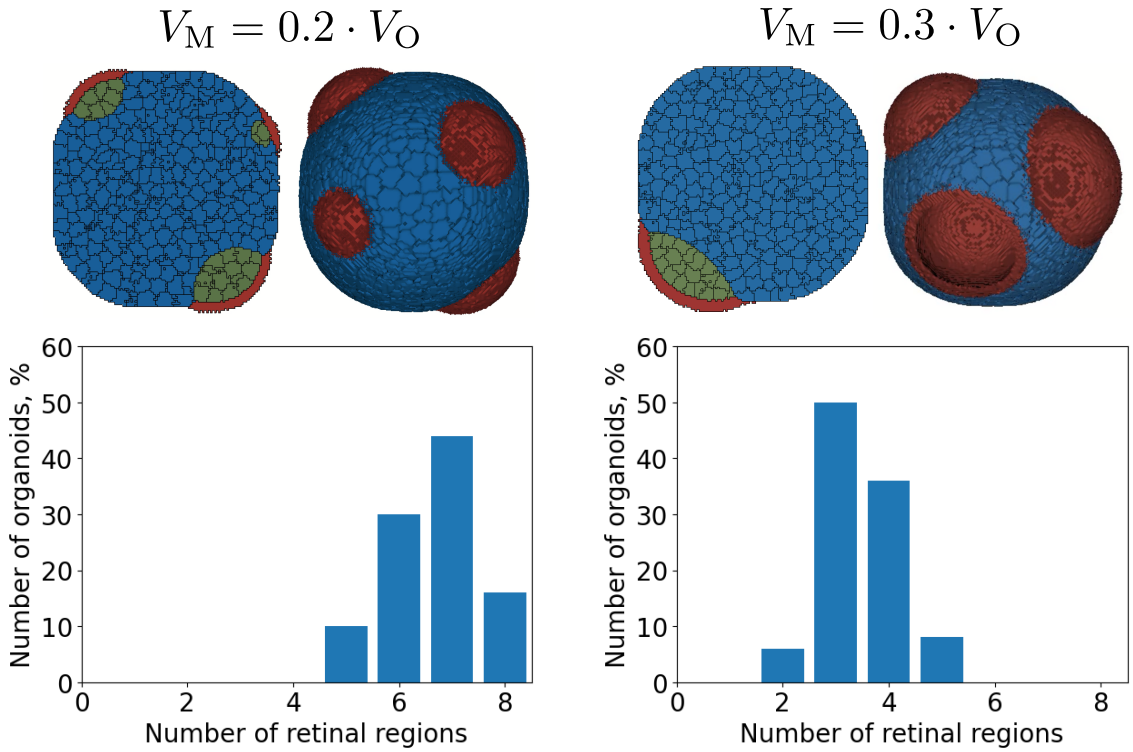

Figure 7.6: **Simulation results for optic vesicle evagination in organoids initially 500 cells and with cell division for different Matrigel volume V_M.** 2D cross section and 3D view of the simulated organoid shape, as well as histograms with the number of retinal regions found in 50 simulated organoids each. Parameters for the simulation can be found in Table A.6.

form small clusters.

When we introduce a low pressure in the simulation, see Fig. 7.5b,b′), the final organoid shapes are similar to the previous results. We obtain spherical cell aggregates with most *Retina* cells at the organoid surface, and again we do not find optic vesicles at the surface. Due to the increased pressure, the remaining *Retina* cells on the inside of the aggregate form less clusters.

Increasing the pressure further leads to mainly single *Retina* cells on the inside of the organoid, while the shape of the organoid remains spherical and the *Retina* cells on the surface do not form optic vesicles, compare Fig. 7.5c,c′).

Thus we can conclude that the optic vesicle evagination in our simulation is due to different adhesion energies and not due to pressure on the aggregate.

7.3.4 Influence of cell division on optic vesicle evagination

Cells in the developing organoid divide, and to understand this effect on organoid shape, Venera Weinhardt estimates that cells divide 2-3 times during the first 24 h

in suspension. We implement division in our simulation by dividing cells randomly during the first 800 MCS. Cell divides along a random axis, and the daughter cells inhibit the cell type of the mother cell and divide again after 800 MCS. Therefore, the total number of cells changes from 500 at initialization to around 1250 after 2000 MCS.

Results from the simulations with division as well as histograms with the number of retinal regions found in the simulated organoids are shown in Fig. 7.6. In both cases, there are no *Retina* cells inside the organoid. We attribute this increased mobility to the implemented cell division as it forces regular rearrangements inside the organoid.

Another difference to previous simulations is that here, increasing the *Matrigel* volume leads to fewer retinal regions in the simulated organoid. It is not yet known if changing the Matrigel amount changes the distribution of observed retinal regions in organoids, only that a change in Matrigel amount does not affect organoid growth significantly, compare Fig. 7.2f). For both amounts of *Matrigel* volume, we find a larger number of vesicles than what is observed experimentally. When we initialize the *Matrigel* with a thicker layer and a higher volume, the simulated organoid shapes change drastically as there is no symmetry breaking of the layer and the organoid remains spherical, which is not expected to happen in experiments. As an improvement to the simulation, one could increase the *Matrigel* volume over time as a method to describe Rx3-expressing cells recruiting Matrigel from the suspension.

7.3.5 Neuroepithelial layer in large organoids

In Fig. 7.2a), we can see a distinct difference between retina organoid shapes developed from aggregates with less than 1000 cells and with more than 1000 cells. Large organoids do not form optic vesicles, but develop a continuous layer of Rx3-expressing cells at the organoid periphery. We do not observe this phenotype by increasing the number of cells in our simulations.

However, we observe an additional difference in the experiments between large and small organoids: the distribution of Rx3-expressing cells is continuous throughout small aggregates with less than 1000 cells, while for large aggregates with 2000 cells, the Rx3-expressing cells are only found at the periphery of the organoid, compare Fig. 7.2e).

This experimental observation can be implemented in our model by restricting the cells that can become *Retina* cells. However, changing the simulation to allow *Retina* cell initialization if the distance between the cell center of mass and the organoid center is larger than 80% of the organoid radius still leads to symmetry

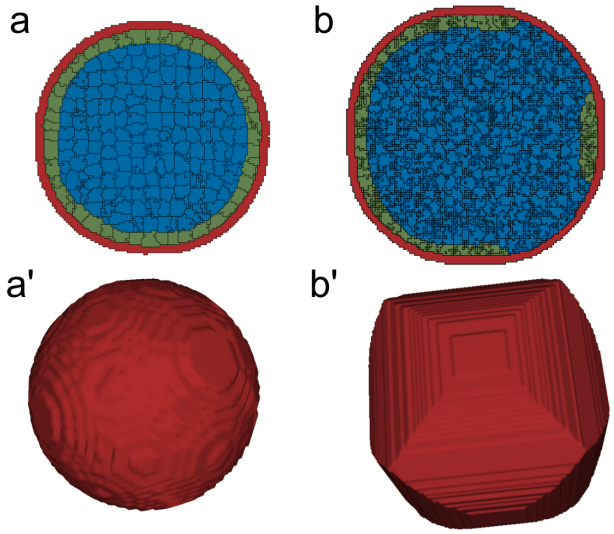

Figure 7.7: **Simulation results for large organoids with 1500 cells with *Retina* cells initialized at the periphery. a,a′**) 2D and 3D results of the simulation without cell division. **b,b′**) 2D and 3D results of the simulation with cell divison. Parameters for the simulation can be found in Table A.6.

breaking and subsequent vesicle formation in the simulated organoid. But after initializing all cells at the periphery of the organoid to become *Retina* cells, we observe the neuroepithelial layer throughout the simulation, see Fig. 7.7a,a′). Even when including cell differentiation to the simulation as described previously, the spherical shape and neuroepithelial layer is still observed, see Fig. 7.7b,b′). However in this case, cell volumes decrease due to the pressure from the surrounding *Matrigel* layer with constant volume, which we do not expect in experiments.

7.4 Discussion

Organoids offer a powerful and versatile platform for studying development and morphogenesis. Their ability to recapitulate tissue complexity in controlled experimental systems bridges the gap between in vitro and in vivo approaches and makes them excellent models to study tissue development and organization. Zilova and colleagues [382] derived retina organoids from medaka fish and observed different morphologies depending on the initial number of cells in the aggregates. Small organoids with less than 1000 cells form between one and four optic vesicle regions, while large aggregates with more than 1000 cells evolve into a single retina, with a neuroepithelial layer on the periphery of the organoid.

The CPM is a great simulation framework to describe emergent properties from

local cell interactions, and by including the cell-Matrigel interaction we were able to reproduce several experimental observations with our model. In small organoids, most simulated *Retina* cells move towards the periphery and form the observed retinal regions in the presence of *Matrigel*. In the absence of *Matrigel* and with a reduced interaction energy $J_{\text{retina, medium}}$, the *Retina* cells move towards the aggregate surface, but do not form optic vesicle clusters. We confirmed that this morphological difference is due to the interaction energies and not due the the increased pressure of the *Matrigel*. Then, we included cell division, which improves cell sorting due to cell rearrangements. In this case, increasing the *Matrigel* volume leads to fewer retinal regions in the simulated organoid. For large organoids, we can reproduce the observed neuroepithelial layer when initializing all cells at the surface as *Retina* cells. It was shown experimentally that the distribution of retina cells in the organoid depends on its size.

We expect that our simulations could be improved to predict the experimentally observed distribution of retinal regions per organoid by increasing the amount of *Matrigel* continuously during the simulation. The simulated Matrigel would represent the Matrigel accumulated by the organoid, not the total Matrigel volume in the experiment, which is most likely a fibrous network throughout the suspension.

The influence of Matrigel on organoid morphogenesis is complex and poorly understood [381], and it is unclear whether the adhesive effect is as prominent as hypothesized in this model. In general, it is difficult to measure adhesion in experiments, as it depends on many factors such as the amount and lifetime of cell-cell contacts and interfacial tensions of the cells. However in this specific case, we would expect an accumulation of Matrigel in the retinal regions, which could be observed experimentally by visualizing Matrigel.

8 Conclusion

The aim of this work was to model cell shape in structured environments. We placed special emphasis on intracellular structures such as the nucleus and stress fibers, and their effect of cell shape, as well as the geometry of the structured environments. Additionally, we modeled shape changes in fish retina organoids.

In **Chapter 2**, we introduced the structures relevant for cell mechanics, specifically the cytoskeletal proteins actin, microtubules, and intermediate filaments, as well as the nucleus and focal adhesion complexes. Additionally, we emphasized the importance of cell shape for various biological processes such as cell function, motility and division; which can in turn be influenced by the physical microenvironment of the cell.

In **Chapter 3**, we described cell experiments in 2D and 3D structured environments that highlight the importance of mechanical factors such as the local microenvironment topography and geometry as well as the substrate stiffness for cell shape and fate. For single cell experiments, the research focuses on internal cell organization, cell shape changes, force generation and migration. For cell collectives, cell-cell adhesion and emerging phenomena such as supracells are investigated. These larger structures have the ability to change their own shape collectively by folding and they can even change their local environment. Lastly, we discussed exciting new possibilities that arise from combining organoid culture with biofabrication or bioprinting techniques. Organoids mimic complex features of organs or tissue architecture and functionality, but currently their use is limited due to heterogeneity and low reproducibility. Combining organoids with well-designed structured environments can help to control cellular growth and behavior in the future.

Chapter 4 complements the experiments described in the previous chapter with an overview of models to describe single cells, cell collectives and organoids in 2D and 3D structured environments. Single cell models shed light on cellular decision-making processes and the impact of microenvironmental cues. Such models enable the exploration of diverse scenarios and aid in the prediction of cellular responses to different stimuli. Cell collective models capture the dynamics of cellular interactions within multicellular systems, revealing emergent properties that arise from cellular cooperation and coordination. These models are instrumental in deciphering the

underlying principles such as tissue morphogenesis. Organoid modeling that explicitly includes the environment is a challenging undertaking. Organoid models, combined with advanced imaging techniques, can help to uncover the spatial and temporal dynamics of tissue development. Then, we focused on the CPM and described how to model 3D cell shape in structured environments. We introduced the cellular Potts framework and its origins in statistical physics as well as its advantages and limitations in describing biological systems. Due to the pseudo-energy formalism, the CPM is a versatile method to model dynamical changes as well as the emergent behavior due to local interactions with the microenvironment. In particular, it can bridge the scale from molecular level to tissue level by integrating information from different scales. Finally, we outlined the code architecture of CompuCell3D, which is the open source software used throughout this work.

In **Chapter 5**, we used the CPM to describe cell shape on structured environments. First, we investigated the role of the nucleus in cell morphology on 2D micropatterned surfaces. We compared simulations with a stiff nuclear compartment at the center of the cell with simulations without explicit nucleus representation, but the same cell volume. We found similar overall morphologies in both cases, with cells with nucleus being slightly more spherical, thus reducing the surface area of the cell. During the spreading process, the trajectories of the center of mass are similar for cells with and without nucleus. However, cells with nucleus reach the steady-state configuration later than cells without explicit nucleus representation due to the stiff nucleus at the rear of the cell and an increased number of MCS necessary to reach the final position. The projected cell morphology during spreading is comparable to experimental results, however the subsequent shape reinforcement can only be modeled with explicit stress fiber representation. Initializing the stress fibers at the beginning of the simulation leads to cell shape changes similar to what is observed experimentally. Implementing stress fiber growth in the 3D CPM is challenging, because there is no measure of stress. We approximated stress with compartmental pressure and reduced volume, and while we did see some stress fiber growth at the invaginated arcs, similar to what is observed experimentally, many processes such as stress fiber interactions and dynamics are not included in our current model.

In the future, the 3D CPM for cell spreading on micropatterns could be compared to 3D experimental data for spreading dynamics and trajectories to confirm or modify the parameter choices. The stress fiber model could be extended to include an additional finite element model to describe the stress inside the compartments, which could be assumed to be linear elastic materials, which are deformed according to compartment shape changes in the CPM.

In **Chapter 6**, we utilized 3D structures manufactured with DLW for precisely controlled conditions to quantify cellular shapes in structured environments experimentally. First, we compared the shapes of single mesenchymal NIH/3T3 cells in structured environments with minimized surfaces under a volume constraint. We found that these shapes differ significantly for cells with invaginated arcs, highlighting the importance of accurately modeling cell shapes in complex environments. To address this issue, we employed two different approaches using the CPM with elastic or linear area energies. Our simulations showed that the Hamiltonian with linear area energy outperformed the elastic area constraint in accurately modeling the shapes of cells in structured environments. Surprisingly, we also found that explicitly modeling the nucleus did not necessarily improve the accuracy of the simulated cell shapes, leading us to the conclusion that the actin cytoskeleton deforms the nucleus significantly in these structures. Overall, our study provides insights into effective methods for modeling cellular shapes in complex environments.

In the future, it would be interesting to place cells in more complex microstructures, to analyze if there are structures in which the nucleus significantly influences cell shape. Additionally, our results can be used to design structures for 3D laser nanoprinting that lead to predefined cell deformations.

In **Chapter 7**, we model the optic cup evagination in fish retina organoids. It was observed experimentally, that the final organoid shape depends on the number of cells in the initial aggregate and on the presence of Matrigel, a secretion product that contains ECM components. With the assignment of interaction energies between the different cell types, it is possible to simulate the process of organoid formation. Similar to the experimental results, we found retinal regions in organoids surrounded by Matrigel, and no retinal regions in the absence of Matrigel. However, the number of retinal regions per organoid differs from experimental results. Additionally, it was observed that large organoids form a single neuroepithelial layer on their surface instead of distinct retinal regions. This observation can only be modeled by initializing the layer at the surface. In this case, it did not break into retinal regions but remained a layer on the surface of the organoid.

In the future, it would be very interesting to visualize the Matrigel in the organoid experiments. Our model is based on differences in interaction energies, while many other processes such as signaling could also be involved in optic cup evagination. Additionally, one could closely monitor organoid morphologies for different amounts of Matrigel, to test if this influences the number of retinal regions. Both experiments could elucidate how large the effect of adhesion is for optic cup formation in organoids.

A Appendix

A.1 Parameters for simulations

In this section, we present the parameters used for the simulations presented throughout this thesis.

Parameter	Symbol	Value
Simulation Temperature	T	1000
Monte Carlo Steps	MCS	2000
Cytoplasm Target Volume	V_{T}(cytoplasm)	60000
Cytoplasm Volume Constraint	λ_V(cytoplasm)	1.0
Nucleus Target Volume	V_{T}(nucleus)	8000
Nucleus Volume Constraint	λ_V(nucleus)	1.0
Cell Target Surface	A_{T}(cell)	20000
Cell Surface Constraint	λ_A(cell)	0.1
Nucleus Target Surface	A_{T}(nucleus)	2500
Nucleus Surface Constraint	λ_A(nucleus)	0.1
Nucleus Centering Constraint	λ_{C}	2000
External Interaction Energy Medium-Medium	J^{ext}(medium,medium)	1.0
External Interaction Energy Medium-Cytoplasm	J^{ext}(medium,cytoplasm)	8.0
External Interaction Energy Medium-Nucleus	J^{ext}(medium,nucleus)	100.0
External Interaction Energy Medium-Adhesive	J^{ext}(medium,adhesive)	1.0
External Interaction Energy Medium-Nonadhesive	J^{ext}(medium,nonadhesive)	1.0
External Interaction Energy Cytoplasm-Cytoplasm	J^{ext}(cytoplasm,cytoplasm)	10.0
External Interaction Energy Cytoplasm-Nucleus	J^{ext}(cytoplasm,nucleus)	100.0
External Interaction Energy Cytoplasm-Adhesive	J^{ext}(cytoplasm,adhesive)	-40.0
External Interaction Energy Cytoplasm-Nonadhesive	J^{ext}(cytoplasm,nonadhesive)	-1.0
External Interaction Energy Nucleus-Nucleus	J^{ext}(nucleus,nucleus)	100.0
External Interaction Energy Nucleus-Adhesive	J^{ext}(nucleus,adhesive)	6.0
External Interaction Energy Nucleus-Nonadhesive	J^{ext}(nucleus,nonadhesive)	6.0
Internal Interaction Energy Cytoplasm-Cytoplasm	J^{int}(cytoplasm,cytoplasm)	10.0
Internal Interaction Energy Cytoplasm-Nucleus	J^{int}(cytoplasm,nucleus)	5.0
Internal Interaction Energy Nucleus-Nucleus	J^{int}(nucleus,nucleus)	100.0
Neighbor Order	N	60

Table A.1: Parameters used in the simulation for Fig. 5.1, Fig. 5.2, Fig. 5.3 and Fig. 5.9.

Parameter	Symbol	Value
Simulation Temperature	T	1000
Monte Carlo Steps	MCS	2000
Cytoplasm Target Volume	V_{T}(cytoplasm)	60000
Cytoplasm Volume Constraint	λ_V(cytoplasm)	1.0
Nucleus Target Volume	V_{T}(nucleus)	8000
Nucleus Volume Constraint	λ_V(nucleus)	1.0
Cell Target Surface	A_{T}(cell)	20000
Cell Surface Constraint	λ_A(cell)	0.1
Nucleus Target Surface	A_{T}(nucleus)	2500
Nucleus Surface Constraint	λ_A(nucleus)	0.1
Nucleus Centering Constraint	λ_{C}	2000
External Interaction Energy Medium-Medium	J^{ext}(medium,medium)	1.0
External Interaction Energy Medium-Cytoplasm	J^{ext}(medium,cytoplasm)	8.0
External Interaction Energy Medium-Nucleus	J^{ext}(medium,nucleus)	100.0
External Interaction Energy Medium-Adhesive	J^{ext}(medium,adhesive)	1.0
External Interaction Energy Medium-Nonadhesive	J^{ext}(medium,nonadhesive)	1.0
External Interaction Energy Cytoplasm-Cytoplasm	J^{ext}(cytoplasm,cytoplasm)	10.0
External Interaction Energy Cytoplasm-Nucleus	J^{ext}(cytoplasm,nucleus)	100.0
External Interaction Energy Cytoplasm-Adhesive	J^{ext}(cytoplasm,adhesive)	-2000.0 (a) -300.0 (b) -80.0 (c) -40.0 (d) -40.0 (e) -40.0 (f)
External Interaction Energy Cytoplasm-Nonadhesive	J^{ext}(cytoplasm,nonadhesive)	-1.0
External Interaction Energy Nucleus-Nucleus	J^{ext}(nucleus,nucleus)	100.0
External Interaction Energy Nucleus-Adhesive	J^{ext}(nucleus,adhesive)	6.0
External Interaction Energy Nucleus-Nonadhesive	J^{ext}(nucleus,nonadhesive)	6.0
Internal Interaction Energy Cytoplasm-Cytoplasm	J^{int}(cytoplasm,cytoplasm)	10.0
Internal Interaction Energy Cytoplasm-Nucleus	J^{int}(cytoplasm,nucleus)	6.0
Internal Interaction Energy Nucleus-Nucleus	J^{int}(nucleus,nucleus)	100.0
Neighbor Order	N	1 (a) 4 (b) 10 (c) 30 (d) 60 (e) 100 (f)

Table A.2: Parameters used in the simulation for Fig. 5.8.

Parameter	Symbol	Value
Simulation Temperature	T	800
Monte Carlo Steps	MCS	1000
Cytoplasm Target Volume	V_{T}(cytoplasm)	152
Cytoplasm Volume Constraint	λ_V(cytoplasm)	100.0
Nucleus Target Volume	V_{T}(nucleus)	8000
Nucleus Volume Constraint	λ_V(nucleus)	1.0
Cell Target Surface	A_{T}(cell)	20000
Cell Surface Constraint	λ_A(cell)	0.1
Cytoplasm Target Surface	A_{T}(cytoplasm)	200
Cytoplasm Surface Constraint	λ_A(cytoplasm)	3.0
Nucleus Target Surface	A_{T}(nucleus)	2500
Nucleus Surface Constraint	λ_A(nucleus)	0.1
Nucleus Centering Constraint	λ_{C}	2000
Line Tension Strength	λ_{SF}	$5 \cdot 10^5$
External Interaction Energy Medium-Medium	J^{ext}(medium,medium)	1.0
External Interaction Energy Medium-Cytoplasm	J^{ext}(medium,cytoplasm)	8.0
External Interaction Energy Medium-Nucleus	J^{ext}(medium,nucleus)	100.0
External Interaction Energy Medium-Adhesive	J^{ext}(medium,adhesive)	1.0
External Interaction Energy Medium-Nonadhesive	J^{ext}(medium,nonadhesive)	1.0
External Interaction Energy Cytoplasm-Cytoplasm	J^{ext}(cytoplasm,cytoplasm)	10.0
External Interaction Energy Cytoplasm-Nucleus	J^{ext}(cytoplasm,nucleus)	100.0
External Interaction Energy Cytoplasm-Adhesive	J^{ext}(cytoplasm,adhesive)	-60.0
External Interaction Energy Cytoplasm-Nonadhesive	J^{ext}(cytoplasm,nonadhesive)	-1.0
External Interaction Energy Nucleus-Nucleus	J^{ext}(nucleus,nucleus)	100.0
External Interaction Energy Nucleus-Adhesive	J^{ext}(nucleus,adhesive)	10.0
External Interaction Energy Nucleus-Nonadhesive	J^{ext}(nucleus,nonadhesive)	10.0
Internal Interaction Energy Cytoplasm-Cytoplasm	J^{int}(cytoplasm,cytoplasm)	1.0
Internal Interaction Energy Cytoplasm-Nucleus	J^{int}(cytoplasm,nucleus)	3.0
Internal Interaction Energy Nucleus-Nucleus	J^{int}(nucleus,nucleus)	100.0
Neighbor Order	N	60

Table A.3: Parameters used in the simulation for Fig. 5.10.

Parameter	Symbol	Value
Simulation Temperature	T	70
Monte Carlo Steps	MCS	1000
Cytoplasm Target Volume	V_{T}(cytoplasm)	125
Cytoplasm Volume Constraint	λ_V(cytoplasm)	2.0
Nucleus Target Volume	V_{T}(nucleus)	4000
Nucleus Volume Constraint	λ_V(nucleus)	20.0
Cell Target Surface	A_{T}(cell)	4874
Cell Surface Constraint	λ_A(cell)	0.001
Cytoplasm Target Surface	A_{T}(cytoplasm)	25
Cytoplasm Surface Constraint	λ_A(cytoplasm)	0.1
Nucleus Target Surface	A_{T}(nucleus)	1219
Nucleus Surface Constraint	λ_A(nucleus)	0.001
Line Tension Strength	λ_{SF}	$5 \cdot 10^5$
External Interaction Energy Medium-Medium	J^{ext}(medium,medium)	1.0
External Interaction Energy Medium-Cytoplasm	J^{ext}(medium,cytoplasm)	20.0
External Interaction Energy Medium-Nucleus	J^{ext}(medium,nucleus)	1000.0
External Interaction Energy Medium-Adhesive	J^{ext}(medium,adhesive)	1.0
External Interaction Energy Medium-Nonadhesive	J^{ext}(medium,nonadhesive)	1.0
External Interaction Energy Cytoplasm-Cytoplasm	J^{ext}(cytoplasm,cytoplasm)	1.0
External Interaction Energy Cytoplasm-Nucleus	J^{ext}(cytoplasm,nucleus)	100.0
External Interaction Energy Cytoplasm-Adhesive	J^{ext}(cytoplasm,adhesive)	-500.0
External Interaction Energy Cytoplasm-Nonadhesive	J^{ext}(cytoplasm,nonadhesive)	100.0
External Interaction Energy Nucleus-Nucleus	J^{ext}(nucleus,nucleus)	100.0
External Interaction Energy Nucleus-Adhesive	J^{ext}(nucleus,adhesive)	10.0
External Interaction Energy Nucleus-Nonadhesive	J^{ext}(nucleus,nonadhesive)	100.0
Internal Interaction Energy Cytoplasm-Cytoplasm	J^{int}(cytoplasm,cytoplasm)	0.1
Internal Interaction Energy Cytoplasm-Nucleus	J^{int}(cytoplasm,nucleus)	0.1
Internal Interaction Energy Nucleus-Nucleus	J^{int}(nucleus,nucleus)	100.0
Neighbor Order	N	7

Table A.4: Parameters used in the simulation for Fig. 5.11 and Fig. 5.12.

Parameter	Symbol	Value
Simulation Temperature	T	100
Monte Carlo Steps	MCS	2000
Cytoplasm Target Volume	V_{T}(cytoplasm)	36789
Cytoplasm Volume Constraint	λ_V(cytoplasm)	0.1
Nucleus Target Volume	V_{T}(retina)	10890
Nucleus Volume Constraint	λ_V(retina)	1.0
Interaction Energy Medium-Medium	J^{ext}(medium,medium)	0.0
Interaction Energy Medium-Nucleus	J^{ext}(medium,other)	80.0
Interaction Energy Cytoplasm-Nucleus	J^{ext}(cytoplasm,nucleus)	5.0
Interaction Energy Cytoplasm-Adhesive	J^{ext}(cytoplasm,adhesive)	4.0
Interaction Energy Nucleus-Adhesive	J^{ext}(nucleus,adhesive)	11.0
Neighbor Order	N	7
Nucleus Centering Constraint	λ_{N}	100

Table A.5: Parameters used in the simulation in Chapter 6.

Parameter	Symbol	Value
Simulation Temperature	T	70
Monte Carlo Steps	MCS	2000
Other Target Volume	V_{T}(other)	350
Other Volume Constraint	λ_V(other)	70
Retina Target Volume	V_{T}(retina)	350
Retina Volume Constraint	λ_V(retina)	70
Matrigel Volume Constraint	λ_V(matrigel)	100
Other Target Surface	A_{T}(other)	450
Other Surface Constraint	λ_A(other)	20
Retina Target Surface	A_{T}(retina)	450
Retina Surface Constraint	λ_A(retina)	20
Matrigel Surface Constraint	λ_A(matrigel)	30
Interaction Energy Medium-Medium	J^{ext}(medium,medium)	1.0
Interaction Energy Medium-Retina	J^{ext}(medium,retina)	4.0 (w/o matrigel) 32.0 (with matrigel)
Interaction Energy Medium-Other	J^{ext}(medium,other)	16.0
Interaction Energy Medium-Matrigel	J^{ext}(medium,matrigel)	5.0
Interaction Energy Retina-Retina	J^{ext}(retina,retina)	4.0
Interaction Energy Retina-Other	J^{ext}(retina,other)	11.0
Interaction Energy Retina-Matrigel	J^{ext}(retina,matrigel)	6.0
Interaction Energy Other-Other	J^{ext}(other,other)	2.0
Interaction Energy Other-Matrigel	J^{ext}(other,matrigel)	11.0
Neighbor Order	N	50

Table A.6: Parameters used in the simulation for Fig. 7.3, Fig. 7.4, Fig. 7.6 and Fig. 7.7.

Parameter	Symbol	Value
Simulation Temperature	T	70
Monte Carlo Steps	MCS	2000
Other Target Volume	V_{T}(other)	350
Other Volume Constraint	λ_V(other)	70
Retina Target Volume	V_{T}(retina)	350
Retina Volume Constraint	λ_V(retina)	70
Matrigel Volume Constraint	λ_V(matrigel)	100
Other Target Surface	A_{T}(other)	450
Other Surface Constraint	λ_A(other)	20
Retina Target Surface	A_{T}(retina)	450
Retina Surface Constraint	λ_A(retina)	20
Matrigel Surface Constraint	λ_A(matrigel)	30
Pressure Constraint	λ_V(organoid)	0.0 (a,a′) 5.0 (b,b′) 20.0 (c,c′)
Interaction Energy Medium-Medium	J^{ext}(medium,medium)	1.0
Interaction Energy Medium-Retina	J^{ext}(medium,retina)	4.0
Interaction Energy Medium-Other	J^{ext}(medium,other)	16.0
Interaction Energy Medium-Matrigel	J^{ext}(medium,matrigel)	5.0
Interaction Energy Retina-Retina	J^{ext}(retina,retina)	4.0
Interaction Energy Retina-Other	J^{ext}(retina,other)	11.0
Interaction Energy Retina-Matrigel	J^{ext}(retina,matrigel)	6.0
Interaction Energy Other-Other	J^{ext}(other,other)	2.0
Interaction Energy Other-Matrigel	J^{ext}(other,matrigel)	11.0
Neighbor Order	N	50

Table A.7: Parameters used in the simulation for Fig. 7.5.

A.2 List of Abbreviations

CC3D CompuCell3D

CMC constant mean curvature

CPM cellular Potts model

DLW direct laser writing

ECM extracellular matrix

FEM finite element method

GFP green fluorescent protein

MCS Monte Carlo step

MTOC microtubule organizing center

PAA polyacrylamide

PDMS polydimethylsiloxane

RPE retina pigmented epithelium

TAZ transcription regulator 1

TFM traction force microscopy

YAP yes-associated protein 1

A.3 List of Figures

A.4 List of Publications

The following table contains a list of the manuscripts which have been prepared during the course of this thesis.

Rabea Link, Ulrich S. Schwarz **Simulating 3D cell shape with the Cellular Potts Model** *Mechanobiology: Methods and Protocols, Springer, 2023.*	Chapter 4
Rabea Link, Kai Weißenbruch, Motumu Tanaka, Martin Bastmeyer, Ulrich S. Schwarz **Cell Shape and Forces in Elastic and Structured Environments: From Single Cells to Organoids** *Advanced Functional Materials, 2302145. Wiley, (2023)*	Chapter 2 & 3
Rabea Link, Mona Jaggy, Martin Bastmeyer, Ulrich S. Schwarz **Modelling Cell Shape in 3D Structured Environments: A Quantitative Comparison with Experiments** *In preparation, https://doi.org/10.1101/2023.08.07.552225*	Chapter 6

B References

1. Heisenberg, C.-P. P. & Bellaïche, Y. Forces in Tissue Morphogenesis and Patterning. *Cell* **153,** 948–962. ISSN: 0092-8674 (2013).
2. Iskratsch, T., Wolfenson, H. & Sheetz, M. P. Appreciating force and shape — the rise of mechanotransduction in cell biology. *Nature Reviews Molecular Cell Biology* **15,** 825–833. ISSN: 1471-0080 (2014).
3. Eyckmans, J., Boudou, T., Yu, X. & Chen, C. S. A Hitchhiker's Guide to Mechanobiology. *Developmental Cell* **21,** 35–47. ISSN: 15345807 (2011).
4. Paluch, E. & Heisenberg, C.-P. Biology and Physics of Cell Shape Changes in Development. *Current Biology* **19,** R790–R799. ISSN: 0960-9822 (2009).
5. Théry, M. *et al.* Anisotropy of cell adhesive microenvironment governs cell internal organization and orientation of polarity. *Proceedings of the National Academy of Sciences of the United States of America* **103,** 19771–19776. ISSN: 00278424 (2006).
6. Minc, N., Burgess, D. & Chang, F. Influence of cell geometry on division-plane positioning. *Cell* **144,** 414–426. ISSN: 00928674 (2011).
7. Watt, F. M., Jordant, P. W. & O'neillt, C. H. Cell shape controls terminal differentiation of human epidermal keratinocytes. *Proceedings of the National Academy of Sciences* **85,** 5576–5580. ISSN: 0027-8424 (1988).
8. Sawyer, J. M. *et al.* Apical constriction: A cell shape change that can drive morphogenesis. *Developmental Biology* **341,** 5–19. ISSN: 0012-1606 (2010).
9. Lye, C. M. *et al.* Mechanical Coupling between Endoderm Invagination and Axis Extension in Drosophila. *PLOS Biology* **13,** e1002292. ISSN: 1545-7885 (2015).
10. Link, R., Weißenbruch, K., Tanaka, M., Bastmeyer, M. & Schwarz, U. S. Cell Shape and Forces in Elastic and Structured Environments: From Single Cells to Organoids. *Advanced Functional Materials,* 2302145. ISSN: 1616-3028 (2023).
11. Fletcher, D. A. & Mullins, R. D. Cell mechanics and the cytoskeleton. eng. *Nature* **463,** 485–492. ISSN: 1476-4687 (2010).

12. Lorenz, C. & Köster, S. Multiscale architecture: Mechanics of composite cytoskeletal networks. *Biophysics Reviews* **3,** 031304 (2022).

13. Stricker, J., Falzone, T. & Gardel, M. L. Mechanics of the F-actin cytoskeleton. *Journal of Biomechanics* **43,** 9–14. ISSN: 0021-9290 (2010).

14. Geiger, B., Spatz, J. P. & Bershadsky, A. D. Environmental sensing through focal adhesions. *Nature Reviews Molecular Cell Biology* **10,** 21–33. ISSN: 1471-0080 (2009).

15. Mishra, Y. G. & Manavathi, B. Focal adhesion dynamics in cellular function and disease. *Cellular Signalling* **85,** 110046. ISSN: 0898-6568 (2021).

16. Graner, F. & Glazier, J. A. Simulation of biological cell sorting using a two-dimensional extended Potts model. *Phys. Rev. Lett.* **69,** 2013–2016 (1992).

17. Marée, A. F. & Hogeweg, P. How amoeboids self-organize into a fruiting body: multicellular coordination in Dictyostelium discoideum. *Proceedings of the National Academy of Sciences of the United States of America* **98,** 3879–83 (2001).

18. Gradeci, D. *et al.* Cell-scale biophysical determinants of cell competition in epithelia. *eLife* **10.** ISSN: 2050-084X (2021).

19. Albert, P. J. & Schwarz, U. S. Dynamics of cell shape and forces on micropatterned substrates predicted by a cellular Potts model. *Biophysical journal* **106,** 2340–2352. ISSN: 15420086 (2014).

20. Scianna, M. & Preziosi, L. A cellular Potts model simulating cell migration on and in matrix environments. *Mathematical Biosciences and Engineering* **10,** 235–261 (2013).

21. Savill, N & Hogeweg, P. Modelling morphogenesis: from single cells to crawling slugs. *Journal of Theoretical Biology,* 229–235 (1997).

22. Szabó, A. & Merks, R. M. H. Cellular potts modeling of tumor growth, tumor invasion, and tumor evolution. *Frontiers in oncology* **3,** 87. ISSN: 2234-943X (2013).

23. Scianna, M. An extended Cellular Potts Model analyzing a wound healing assay. *Computers in Biology and Medicine* **62,** 33–54 (2015).

24. Tsingos, E., Bakker, B. H., Keijzer, K. A., Hupkes, H. J. & Merks, R. M. Hybrid cellular Potts and bead-spring modeling of cells in fibrous extracellular matrix. *Biophysical Journal* **122,** 2609–2622. ISSN: 0006-3495 (2023).

25. Singer, S. J. & Nicolson, G. L. The Fluid Mosaic Model of the Structure of Cell Membranes. *Science* **175,** 720–731. ISSN: 00368075 (1972).

26. Kelkar, M., Bohec, P. & Charras, G. Mechanics of the cellular actin cortex: From signalling to shape change. *Current Opinion in Cell Biology* **66,** 69–78. ISSN: 18790410 (2020).

27. Bray, D. & White, J. G. Cortical flow in animal cells. *Science* **239,** 883–888. ISSN: 00368075 (1988).

28. Salbreux, G., Charras, G. & Paluch, E. Actin cortex mechanics and cellular morphogenesis. *Trends in Cell Biology* **22,** 536–545. ISSN: 0962-8924 (2012).

29. Chugh, P. *et al.* Actin cortex architecture regulates cell surface tension Europe PMC Funders Group. *Nat Cell Biol* **19,** 689–697 (2017).

30. Chugh, P. & Paluch, E. K. The actin cortex at a glance. *Journal of Cell Science* **131.** ISSN: 14779137 (2018).

31. Svitkina, T. M. Actin Cell Cortex: Structure and Molecular Organization. *Trends in Cell Biology* **30,** 556–565. ISSN: 0962-8924 (2020).

32. Wortel, I. M. *et al.* Local actin dynamics couple speed and persistence in a Cellular Potts Model of cell migration. *Biophysical Journal* **120,** 2609–2622. ISSN: 0006-3495 (2021).

33. Pellegrin, S., Mellor, H., Barry, P, Andrews, P & Jester, J. V. Actin stress fibres. *Journal of cell science* **120,** 3491–9 (2007).

34. Kassianidou, E. & Kumar, S. A biomechanical perspective on stress fiber structure and function. *Biochimica et Biophysica Acta (BBA) - Molecular Cell Research* **1853,** 3065–3074 (2015).

35. Kassianidou, E. *et al.* Extracellular Matrix Geometry and Initial Adhesive Position Determine Stress Fiber Network Organization during Cell Spreading. *Cell Reports* **27,** 1897–1909.e4. ISSN: 22111247 (2019).

36. *Molecular biology of the cell* 6. ed. (ed Alberts, B.) (Garland Science, New York, NY, 2015).

37. Brouhard, G. J. & Rice, L. M. Microtubule dynamics: an interplay of biochemistry and mechanics. *Nature Reviews Molecular Cell Biology* **19,** 451–463. ISSN: 1471-0080 (2018).

38. Qin, Z., Buehler, M. J. & Kreplak, L. A multi-scale approach to understand the mechanobiology of intermediate filaments. *Journal of Biomechanics* **43,** 15–22. ISSN: 0021-9290 (2010).

39. Lammerding, J. in *Comprehensive Physiology* 783–807 (John Wiley & Sons, Inc., Hoboken, NJ, USA, 2011).

40. Maniotis, A. J., Chen, C. S. & Ingber, D. E. Demonstration of mechanical connections between integrins, cytoskeletal filaments, and nucleoplasm that stabilize nuclear structure. *Proceedings of the National Academy of Sciences of the United States of America* **94,** 849–854. ISSN: 00278424 (1997).

41. Kirby, T. J. & Lammerding, J. Emerging views of the nucleus as a cellular mechanosensor. *Nature Cell Biology* **20,** 373–381. ISSN: 1476-4679 (2018).

42. Elosegui-Artola, A. *et al.* Force Triggers YAP Nuclear Entry by Regulating Transport across Nuclear Pores. *Cell* **171,** 1397–1410.e14. ISSN: 10974172 (2017).

43. Jimenez, A. J. *et al.* Acto-myosin network geometry defines centrosome position. *Current Biology* **31,** 1206–1220.e5. ISSN: 0960-9822 (2021).

44. Legerstee, K. & Houtsmuller, A. B. A Layered View on Focal Adhesions. *Biology 2021, Vol. 10, Page 1189* **10,** 1189. ISSN: 2079-7737 (2021).

45. Luxenburg, C. & Zaidel-Bar, R. From cell shape to cell fate via the cytoskeleton — Insights from the epidermis. *Experimental Cell Research* **378,** 232–237. ISSN: 0014-4827 (2019).

46. Coles, C. H. & Bradke, F. Coordinating neuronal actin-microtubule dynamics. *Current biology* **25,** R677–R691. ISSN: 1879-0445 (2015).

47. Diez-Silva, M., Dao, M., Han, J., Lim, C. T. & Suresh, S. Shape and Biomechanical Characteristics of Human Red Blood Cells in Health and Disease. *MRS Bulletin* **35,** 382–388. ISSN: 1938-1425 (2010).

48. Braga, V. Epithelial Cell Shape: Cadherins and Small GTPases. *Experimental Cell Research* **261,** 83–90. ISSN: 0014-4827 (2000).

49. Bodor, D. L., Pönisch, W., Endres, R. G. & Paluch, E. K. Of Cell Shapes and Motion: The Physical Basis of Animal Cell Migration. *Developmental Cell* **52,** 550–562. ISSN: 1534-5807 (2020).

50. Chen, C. S., Mrksich, M, Huang, S, Whitesides, G. M. & Ingber, D. E. Geometric control of cell life and death. *Science* **276,** 1425–1428. ISSN: 0036-8075 (1997).

51. James, J., Goluch, E. D., Hu, H., Liu, C. & Mrksich, M. Subcellular curvature at the perimeter of micropatterned cells influences lamellipodial distribution and cell polarity. *Cell Motility and the Cytoskeleton* **65,** 841–852. ISSN: 08861544 (2008).

52. Mitrossilis, D. *et al.* Single-cell response to stiffness exhibits muscle-like behavior. *Proceedings of the National Academy of Sciences of the United States of America* **106,** 18243–18248. ISSN: 00278424 (2009).

53. Pieuchot, L. *et al.* Curvotaxis directs cell migration through cell-scale curvature landscapes. *Nature Communications* **9,** 1–13. ISSN: 2041-1723 (2018).

54. Zhou, F. *et al.* Quasi-periodic migration of single cells on short microlanes (2020).

55. Isomursu, A. *et al.* Directed cell migration towards softer environments. *Nature Materials* **21,** 1081–1090. ISSN: 1476-4660 (2022).

56. Pentinmikko, N *et al.* Cellular shape reinforces niche to stem cell signaling in the small intestine. *Sci Adv* **8,** eabm1847. ISSN: 2375-2548 (Electronic) 2375-2548 (Linking) (2022).

57. Wang, Y *et al.* A microengineered collagen scaffold for generating a polarized crypt-villus architecture of human small intestinal epithelium. *Biomaterials* **128,** 44–55 (2017).

58. Yi, B, Xu, Q & Liu, W. An overview of substrate stiffness guided cellular response and its applications in tissue regeneration. *Bioact Mater* **15,** 82–102 (2022).

59. Ng, M. R., Besser, A, Danuser, G & Brugge, J. S. Substrate stiffness regulates cadherin-dependent collective migration through myosin-II contractility. *J Cell Biol* **199,** 545–563. ISSN: 1540-8140 (2012).

60. Jiang, Y *et al.* Targeting extracellular matrix stiffness and mechanotransducers to improve cancer therapy. *J Hematol Oncol* **15,** 34. ISSN: 1756-8722 (2022).

61. Balcioglu, H. E. *et al.* A subtle relationship between substrate stiffness and collective migration of cell clusters. *Soft Matter* **16,** 1825–1839. ISSN: 1744-6848 (2020).

62. Eroshenko, N, Ramachandran, R, Yadavalli, V. K. & Rao, R. R. Effect of substrate stiffness on early human embryonic stem cell differentiation. *J Biol Eng* **7,** 7. ISSN: 1754-1611 (Print) 1754-1611 (Electronic) 1754-1611 (Linking) (2013).

63. Cao, H *et al.* Substrate stiffness regulates differentiation of induced pluripotent stem cells into heart valve endothelial cells. *Acta Biomater* **143,** 115–126. ISSN: 1878-7568 (Electronic) 1742-7061 (Linking) (2022).

64. Ruprecht, V. *et al.* How cells respond to environmental cues - insights from bio-functionalized substrates. *Journal of cell science* **130,** 51–61. ISSN: 1477-9137 (2017).

65. Dupont, S. *et al.* Role of YAP/TAZ in mechanotransduction. *Nature* **474,** 179–183. ISSN: 1476-4687 (2011).

66. Oliver, T., Jacobson, K. & Dembo, M. Traction forces in locomoting cells. *Cell Motility and the Cytoskeleton* **31,** 225–240. ISSN: 1097-0169 (1995).

67. Dembo, M. & Wang, Y. L. Stresses at the Cell-to-Substrate Interface during Locomotion of Fibroblasts. *Biophysical Journal* **76,** 2307–2316. ISSN: 0006-3495 (1999).

68. Pelham, R. J. & Wang, Y. L. Cell locomotion and focal adhesions are regulated by substrate flexibility. *Proceedings of the National Academy of Sciences* **94,** 13661–13665. ISSN: 00278424 (1997).

69. Engler, A. J., Sen, S., Sweeney, H. L. & Discher, D. E. Matrix elasticity directs stem cell lineage specification. *Cell* **126,** 677–689. ISSN: 0092-8674 (Print) (2006).

70. McBeath, R., Pirone, D. M., Nelson, C. M., Bhadriraju, K. & Chen, C. S. Cell Shape, Cytoskeletal Tension, and RhoA Regulate Stem Cell Lineage Commitment. *Developmental Cell* **6,** 483–495. ISSN: 1534-5807 (2004).

71. Andreu, I. *et al.* Mechanical force application to the nucleus regulates nucleocytoplasmic transport. *Nature Cell Biology* **24,** 896–905. ISSN: 1476-4679 (2022).

72. Sunyer, R. *et al.* Collective cell durotaxis emerges from long-range intercellular force transmission. *Science* **353,** 1157–1161 (2016).

73. Garreta, E. *et al.* Rethinking organoid technology through bioengineering. *Nat Mater* **20,** 145–155. ISSN: 1476-4660 (2021).

74. Hofer, M. & Lutolf, M. P. Engineering organoids. *Nature Review Materals* **6,** 402–420 (2021).

75. Huisken, J., Swoger, J., Bene, F. D., Wittbrodt, J. & Stelzer, E. H. Optical sectioning deep inside live embryos by selective plane illumination microscopy. *Science* **305,** 1007–1009. ISSN: 00368075 (2004).

76. Pampaloni, F., Reynaud, E. G. & Stelzer, E. H. The third dimension bridges the gap between cell culture and live tissue. *Nature Reviews Molecular Cell Biology* **8,** 839–845. ISSN: 1471-0080 (2007).

77. Li, D. *et al.* Extended-resolution structured illumination imaging of endocytic and cytoskeletal dynamics. *Science* **349.** ISSN: 10959203 (2015).

78. Campàs, O. *et al.* Quantifying cell-generated mechanical forces within living embryonic tissues. *Nature Methods* **11,** 183–189. ISSN: 1548-7105 (2013).

79. Wu, P. H. *et al.* A comparison of methods to assess cell mechanical properties. *Nature Methods* **15,** 491–498. ISSN: 1548-7105 (2018).

80. Oakes, P. W. *et al.* Optogenetic control of RhoA reveals zyxin-mediated elasticity of stress fibres. *Nature Communications* **8,** 15817. ISSN: 2041-1723 (2017).

81. Klein, F. *et al.* Two-component polymer scaffolds for controlled three-dimensional cell culture. *Advanced Materials* **23,** 1341–1345. ISSN: 09359648 (2011).

82. Hippler, M. *et al.* 3D Scaffolds to Study Basic Cell Biology. *Advanced Materials* **31,** 1808110. ISSN: 09359648 (2019).

83. Karzbrun, E. *et al.* Human neural tube morphogenesis in vitro by geometric constraints. *Nature* **599,** 268–272. ISSN: 1476-4687 (2021).

84. Gjorevski, N. *et al.* Tissue geometry drives deterministic organoid patterning. *Science* **375.** ISSN: 10959203 (2022).

85. Niethammer, P. Components and Mechanisms of Nuclear Mechanotransduction. *Annual Review of Cell and Developmental Biology* **37,** 233–256. ISSN: 15308995 (2021).

86. Schwarz, U. S. Soft matters in cell adhesion: rigidity sensing on soft elastic substrates. *Soft Matter* **3,** 263–266. ISSN: 1744-6848 (2007).

87. Lomakin, A. J. *et al.* The nucleus acts as a ruler tailoring cell responses to spatial constraints. *Science* **370.** ISSN: 10959203 (2020).

88. Renkawitz, J. *et al.* Nuclear positioning facilitates amoeboid migration along the path of least resistance. *Nature* **568,** 546–550. ISSN: 1476-4687 (2019).

89. Humphries, J. D., Chastney, M. R., Askari, J. A. & Humphries, M. J. Signal transduction via integrin adhesion complexes. *Current Opinion in Cell Biology* **56,** 14–21. ISSN: 0955-0674 (2019).

90. Discher, D. E., Janmey, P. & Wang, Y.-L. L. Tissue cells feel and respond to the stiffness of their substrate. eng. *Science* **310,** 1139–1143. ISSN: 1095-9203 (2005).

91. Théry, M. Micropatterning as a tool to decipher cell morphogenesis and functions. *Journal of Cell Science* **123,** 4201–4213. ISSN: 0021-9533 (2010).

92. Callens, S. J. P., Uyttendaele, R. J. C., Fratila-Apachitei, L. E. & Zadpoor, A. A. Substrate curvature as a cue to guide spatiotemporal cell and tissue organization. *Biomaterials* **232,** 119739 (2020).

93. Ladoux, B., Mège, R. M. & Trepat, X. Front-Rear Polarization by Mechanical Cues: From Single Cells to Tissues. *Trends in Cell Biology* **26,** 420–433. ISSN: 18793088 (2016).

94. Raab, M. *et al.* Crawling from soft to stiff matrix polarizes the cytoskeleton and phosphoregulates myosin-II heavy chain. *Journal of Cell Biology* **199,** 669–683. ISSN: 0021-9525 (2012).

95. Zemel, A., Rehfeldt, F., Brown, A. E., Discher, D. E. & Safran, S. A. Optimal matrix rigidity for stress fiber polarization in stem cells. *Nature physics* **6,** 468–473. ISSN: 1745-2473 (2010).

96. Théry, M., Pépin, A., Dressaire, E., Chen, Y. & Bornens, M. Cell Distribution of Stress Fibres in Response to the Geometry of the Adhesive Environment. *Cell Motil. Cytoskeleton* **63** (2006).

97. Califano, J. P. & Reinhart-King, C. A. Substrate stiffness and cell area predict cellular traction stresses in single cells and cells in contact. *Cellular and Molecular Bioengineering* **3,** 68–75. ISSN: 18655025 (2010).

98. Lo, C. M., Wang, H. B., Dembo, M. & Wang, Y. L. Cell Movement Is Guided by the Rigidity of the Substrate. *Biophysical Journal* **79,** 144–152. ISSN: 0006-3495 (2000).

99. DeForest, C. A. & Anseth, K. S. Advances in Bioactive Hydrogels to Probe and Direct Cell Fate (2012).

100. Missirlis, D. & Spatz, J. P. Combined effects of PEG hydrogel elasticity and cell-adhesive coating on fibroblast adhesion and persistent migration. *Biomacromolecules* **15,** 195–205. ISSN: 15257797 (2014).

101. Wang, W. *et al.* Protein diffusion in photopolymerized poly(ethylene glycol) hydrogel networks. *Biomedical Materials* **6,** 055006. ISSN: 1748-605X (2011).

102. Huang, G. *et al.* Engineering three-dimensional cell mechanical microenvironment with hydrogels. *Biofabrication* **4,** 042001. ISSN: 1758-5090 (2012).

103. Guvendiren, M. & Burdick, J. A. Engineering synthetic hydrogel microenvironments to instruct stem cells. *Current Opinion in Biotechnology* **24,** 841–846. ISSN: 0958-1669 (2013).

104. Li, D. *et al.* Astigmatic traction force microscopy (aTFM). *Nature Communications* **12,** 1–10. ISSN: 2041-1723 (2021).

105. Balaban, N. Q. *et al.* Force and focal adhesion assembly: a close relationship studied using elastic micropatterned substrates. *Nature Cell Biology* **3,** 466–472. ISSN: 1476-4679 (2001).

106. Moshayedi, P. *et al.* Mechanosensitivity of astrocytes on optimized polyacrylamide gels analyzed by quantitative morphometry. *J. Phys.: Condens. Matter* **22,** 194114–194125 (2010).

107. Charrier, E. E. *et al.* A novel method to make viscoelastic polyacrylamide gels for cell culture and traction force microscopy. *APL Bioengineering* **4.** ISSN: 24732877 (2020).

108. Gutierrez, E. *et al.* High Refractive Index Silicone Gels for Simultaneous Total Internal Reflection Fluorescence and Traction Force Microscopy of Adherent Cells. *PLOS ONE* **6,** e23807. ISSN: 1932-6203 (2011).

109. Heinrichs, V. *et al.* Chemically defined, ultrasoft PDMS elastomers with selectable elasticity for mechanobiology. *PLOS ONE* **13,** e0195180. ISSN: 1932-6203 (2018).

110. Nelson, C. M. *et al.* Emergent patterns of growth controlled by multicellular form and mechanics. *Proc Natl Acad Sci U S A* **102,** 11594–11599. ISSN: 0027-8424 (2005).

111. Wen, J. H. *et al.* Interplay of matrix stiffness and protein tethering in stem cell differentiation. *Nature Materials* **13,** 979–987. ISSN: 1476-4660 (2014).

112. Falconnet, D., Csucs, G., Michelle Grandin, H. & Textor, M. Surface engineering approaches to micropattern surfaces for cell-based assays. *Biomaterials* **27,** 3044–3063. ISSN: 0142-9612 (2006).

113. Mrksich, M *et al.* Controlling cell attachment on contoured surfaces with self-assembled monolayers of alkanethiolates on gold. *Proc Natl Acad Sci U S A* **93,** 10775–10778 (1996).

114. Gauthier, N. C., Fardin, M. A., Roca-Cusachs, P. & Sheetz, M. P. Temporary increase in plasma membrane tension coordinates the activation of exocytosis and contraction during cell spreading. *Proceedings of the National Academy of Sciences of the United States of America* **108,** 14467–14472. ISSN: 00278424 (2011).

115. Hotulainen, P. & Lappalainen, P. Stress fibers are generated by two distinct actin assembly mechanisms in motile cells. *Journal of Cell Biology* **173,** 383–394. ISSN: 00219525 (2006).

116. Jalal, S. *et al.* Actin cytoskeleton self-organization in single epithelial cells and fibroblasts under isotropic confinement. *Journal of Cell Science* **132.** ISSN: 14779137 (2019).

117. Tee, Y. H. *et al.* Cellular chirality arising from the self-organization of the actin cytoskeleton. *Nature Cell Biology* **17,** 445–457. ISSN: 1476-4679 (2015).

118. Maiuri, P. *et al.* The first World Cell Race. *Current biology* **22,** R673. ISSN: 09609822 (2012).

119. Maiuri, P. *et al.* Actin flows mediate a universal coupling between cell speed and cell persistence. *Cell* **161,** 374–386. ISSN: 10974172 (2015).

120. Autenrieth, T. J. *et al.* Actomyosin contractility and RhoGTPases affect cell-polarity and directional migration during haptotaxis. *Integrative biology : quantitative biosciences from nano to macro* **8,** 1067–1078. ISSN: 1757-9708 (2016).

121. Brückner, D. B. *et al.* Stochastic nonlinear dynamics of confined cell migration in two-state systems. *Nature Physics* **15,** 595–601. ISSN: 1745-2481 (2019).

122. Tan, J. L. *et al.* Cells lying on a bed of microneedles: an approach to isolate mechanical force. *Proceedings of the National Academy of Sciences of the United States of America* **100,** 1484–1489. ISSN: 0027-8424 (2003).

123. Rape, A. D., Guo, W. H. & Wang, Y. L. The regulation of traction force in relation to cell shape and focal adhesions. *Biomaterials* **32,** 2043–2051. ISSN: 01429612 (2011).

124. Tseng, Q. *et al.* A new micropatterning method of soft substrates reveals that different tumorigenic signals can promote or reduce cell contraction levels. *Lab on a Chip* **11,** 2231–2240. ISSN: 14730189 (2011).

125. Schwarz, U. S. & Soiné, J. R. Traction force microscopy on soft elastic substrates: A guide to recent computational advances. *Biochimica et Biophysica Acta - Molecular Cell Research* **1853,** 3095–3104. ISSN: 18792596. eprint: 1506.02394 (2015).

126. Vignaud, T. *et al.* Stress fibres are embedded in a contractile cortical network. *Nature Materials* **20,** 410–420. ISSN: 1476-4660 (2020).

127. Gupta, M. *et al.* Micropillar substrates: A tool for studying cell mechanobiology. *Methods in Cell Biology* **125,** 289–308. ISSN: 0091679X (2015).

128. Ganz, A. *et al.* Traction forces exerted through N-cadherin contacts. *Biology of the Cell* **98,** 721–730. ISSN: 1768-322X (2006).

129. Schoen, I., Hu, W., Klotzsch, E. & Vogel, V. Probing cellular traction forces by micropillar arrays: Contribution of substrate warping to pillar deflection. *Nano Letters* **10,** 1823–1830. ISSN: 15306984 (2010).

130. Hughes, J. H. & Kumar, S. Synthetic mechanobiology: Engineering cellular force generation and signaling. *Current Opinion in Biotechnology* **40,** 82–89. ISSN: 18790429 (2016).

131. Wittmann, T., Dema, A. & van Haren, J. Lights, cytoskeleton, action: Optogenetic control of cell dynamics. *Current Opinion in Cell Biology* **66,** 1–10. ISSN: 18790410 (2020).

132. Wu, Y. I. *et al.* A genetically encoded photoactivatable Rac controls the motility of living cells. *Nature* **461,** 104–108. ISSN: 1476-4687 (2009).

133. De Beco, S. *et al.* Optogenetic dissection of Rac1 and Cdc42 gradient shaping. *Nature Communications* **9,** 1–13. ISSN: 2041-1723 (2018).

134. Hennig, K. *et al.* Stick-slip dynamics of cell adhesion triggers spontaneous symmetry breaking and directional migration of mesenchymal cells on one-dimensional lines. *Science Advances* **6.** ISSN: 23752548 (2020).

135. Hadjitheodorou, A. *et al.* Directional reorientation of migrating neutrophils is limited by suppression of receptor input signaling at the cell rear through myosin II activity. *Nature Communications* **12,** 1–15. ISSN: 2041-1723 (2021).

136. Valon, L., Marín-Llauradó, A., Wyatt, T., Charras, G. & Trepat, X. Optogenetic control of cellular forces and mechanotransduction. *Nature Communications* **8,** 1–10. ISSN: 2041-1723 (2017).

137. Andersen, T. *et al.* Cell size and actin architecture determine force generation in optogenetically activated cells. *Biophysical Journal* **0.** ISSN: 0006-3495 (2023).

138. Dunn, G. A. & Heath, J. P. A new hypothesis of contact guidance in tissue cells. *Experimental Cell Research* **101,** 1–14. ISSN: 0014-4827 (1976).

139. Werner, M. *et al.* Surface Curvature Differentially Regulates Stem Cell Migration and Differentiation via Altered Attachment Morphology and Nuclear Deformation. *Advanced Science* **4,** 1600347. ISSN: 2198-3844 (2017).

140. Cukierman, E., Pankov, R., Stevens, D. R. & Yamada, K. M. Taking cell-matrix adhesions to the third dimension. *Science* **294,** 1708–1712. ISSN: 00368075 (2001).

141. Baker, B. M. & Chen, C. S. Deconstructing the third dimension-how 3D culture microenvironments alter cellular cues. *Journal of Cell Science* **125,** 3015–3024. ISSN: 00219533 (2012).

142. Chen, C. S. 3D Biomimetic Cultures: The Next Platform for Cell Biology. *Trends in Cell Biology* **26,** 798–800. ISSN: 0962-8924 (2016).

143. Young, J. L., Holle, A. W. & Spatz, J. P. Nanoscale and mechanical properties of the physiological cell–ECM microenvironment. *Experimental Cell Research* **343,** 3–6. ISSN: 0014-4827 (2016).

144. Grinnell, F. Fibroblast biology in three-dimensional collagen matrices. *Trends in Cell Biology* **13,** 264–269. ISSN: 0962-8924 (2003).

145. Yamada, K. M. & Sixt, M. Mechanisms of 3D cell migration. *Nature Reviews Molecular Cell Biology* **20,** 738–752. ISSN: 1471-0080 (2019).

146. Harunaga, J. S. & Yamada, K. M. Cell-matrix adhesions in 3D. *Matrix Biology* **30,** 363–368. ISSN: 0945-053X (2011).

147. Kutys, M. L. & Chen, C. S. Forces and mechanotransduction in 3D vascular biology. *Current Opinion in Cell Biology* **42,** 73–79. ISSN: 18790410 (2016).

148. Huang, G. *et al.* Functional and Biomimetic Materials for Engineering of the Three-Dimensional Cell Microenvironment. *Chemical Reviews* **117,** 12764–12850. ISSN: 15206890 (2017).

149. Velve-Casquillas, G., Le Berre, M., Piel, M. & Tran, P. T. Microfluidic tools for cell biological research. *Nano today* **5,** 28. ISSN: 17480132 (2010).

150. Vernerey, F. J., Lalitha Sridhar, S., Muralidharan, A. & Bryant, S. J. Mechanics of 3D Cell-Hydrogel Interactions: Experiments, Models, and Mechanisms. *Chemical Reviews* **121,** 11085–11148. ISSN: 15206890 (2021).

151. Weißenbruch, K. *et al.* Distinct roles of nonmuscle myosin ii isoforms for establishing tension and elasticity during cell morphodynamics. *eLife* **10.** ISSN: 2050084X (2021).

152. Brand, C. A. *et al.* Tension and Elasticity Contribute to Fibroblast Cell Shape in Three Dimensions. *Biophysical Journal* **113,** 770–774. ISSN: 15420086 (2017).

153. Hall, M. S. *et al.* Toward single cell traction microscopy within 3D collagen matrices. *Experimental Cell Research* **319,** 2396–2408. ISSN: 0014-4827 (2013).

154. Stowers, R. S., Allen, S. C., Suggs, L. J. & Anseth, K. S. Dynamic phototuning of 3D hydrogel stiffness. *Proceedings of the National Academy of Sciences of the United States of America* **112,** 1953–1958. ISSN: 10916490 (2015).

155. Lee, J. M. & Yeong, W. Y. Design and Printing Strategies in 3D Bioprinting of Cell-Hydrogels: A Review. *Advanced Healthcare Materials* **5,** 2856–2865. ISSN: 2192-2659 (2016).

156. Pataky, K. *et al.* Microdrop Printing of Hydrogel Bioinks into 3D Tissue-Like Geometries. *Advanced Materials* **24,** 391–396. ISSN: 1521-4095 (2012).

157. Tabdanov, E. D., Puram, V., Zhovmer, A. & Provenzano, P. P. Microtubule-Actomyosin Mechanical Cooperation during Contact Guidance Sensing. *Cell-Reports* **25,** 328–338.e5 (2018).

158. Tabdanov, E. D. *et al.* Engineering T cells to enhance 3D migration through structurally and mechanically complex tumor microenvironments. *Nature Communications* **12,** 1–17. ISSN: 2041-1723 (2021).

159. Sheets, K, Wang, J, Zhao, W, Kapania, R & Nain, A. S. Nanonet Force Microscopy for Measuring Cell Forces. *Biophys J* **111,** 197–207 (2016).

160. Bao, M., Xie, J., Piruska, A. & Huck, W. T. 3D microniches reveal the importance of cell size and shape. *Nature Communications* **8,** 1–12. ISSN: 2041-1723 (2017).

161. Sharma, Y. *et al.* Fabrication of conducting electrospun nanofibers scaffold for three-dimensional cells culture. *International Journal of Biological Macromolecules* **51,** 627–631 (2012).

162. Scheibel, T. Spider silks: Recombinant synthesis, assembly, spinning, and engineering of synthetic proteins. *Microbial Cell Factories* **3,** 1–10. ISSN: 14752859 (2004).

163. Lazaris, A. *et al.* Spider silk fibers spun from soluble recombinant silk produced in mammalian cells. *Science* **295,** 472–476. ISSN: 00368075 (2002).

164. Matthews, J. A., Wnek, G. E., Simpson, D. G. & Bowlin, G. L. Electrospinning of Collagen Nanofibers. *Biomacromolecules* **3,** 232–238. ISSN: 15257797 (2002).

165. Rho, K. S. *et al.* Electrospinning of collagen nanofibers: Effects on the behavior of normal human keratinocytes and early-stage wound healing. *Biomaterials* **27,** 1452–1461. ISSN: 0142-9612 (2006).

166. Huang, Z. M., Zhang, Y. Z., Ramakrishna, S. & Lim, C. T. Electrospinning and mechanical characterization of gelatin nanofibers. *Polymer* **45,** 5361–5368. ISSN: 0032-3861 (2004).

167. Li, M. *et al.* Electrospun protein fibers as matrices for tissue engineering. *Biomaterials* **26,** 5999–6008. ISSN: 0142-9612 (2005).

168. Nam, J, Johnson, J, Lannutti, J. J. & Agarwal, S. Modulation of embryonic mesenchymal progenitor cell differentiation via control over pure mechanical modulus in electrospun nanofibers. *Acta Biomater* **7,** 1516–1524. ISSN: 1878-7568 (2011).

169. Yu, L. *et al.* Low Cell-Matrix Adhesion Reveals Two Subtypes of Human Pluripotent Stem Cells. *Stem Cell Reports* **11,** 142–156. ISSN: 22136711 (2018).

170. Ma, Z., Kotaki, M., Inai, R. & Ramakrishna, S. Potential of nanofiber matrix as tissue-engineering scaffolds. *Tissue engineering* **11,** 101–109. ISSN: 1076-3279 (2005).

171. Kidoaki, S., Kwon, I. K. & Matsuda, T. Mesoscopic spatial designs of nano- and microfiber meshes for tissue-engineering matrix and scaffold based on newly devised multilayering and mixing electrospinning techniques. *Biomaterials* **26,** 37–46. ISSN: 0142-9612 (2005).

172. Smith, A. M., Banwell, E. F., Edwards, W. R., Pandya, M. J. & Woolfson, D. N. Engineering increased stability into self-assembled protein fibers. *Advanced Functional Materials* **16,** 1022–1030. ISSN: 1616-3028 (2006).

173. Bentele, T. *et al.* New Class of Crosslinker-Free Nanofiber Biomaterials from Hydra Nematocyst Proteins. *Scientific Reports 2019 9:1* **9,** 1–9. ISSN: 2045-2322 (2019).

174. Hayashi, K., Matsuda, M., Nakahata, M., Takashima, Y. & Tanaka, M. Stimulus-Responsive, Gelatin-Containing Supramolecular Nanofibers as Switchable 3D Microenvironments for Cells. *Polymers* **14,** 4407. ISSN: 20734360 (2022).

175. Bongiovanni Abel, S., Montini Ballarin, F. & Abraham, G. A. Combination of electrospinning with other techniques for the fabrication of 3D polymeric and composite nanofibrous scaffolds with improved cellular interactions. *Nanotechnology* **31,** 172002. ISSN: 0957-4484 (2020).

176. Pattanapiboon, W. & Nakmahachalasint, P. Design and implementation of three-dimensional electrospinning machine. *Electronics Letters* **57,** 799–801. ISSN: 1350911X (2021).

177. Nain, A. S. *et al.* Control of cell behavior by aligned micro/nanofibrous biomaterial scaffolds fabricated by spinneret-based tunable engineered parameters (STEP) technique. *Small* **4,** 1153–1159. ISSN: 16136810 (2008).

178. Jana, A. *et al.* Crosshatch nanofiber networks of tunable interfiber spacing induce plasticity in cell migration and cytoskeletal response. *FASEB Journal* **33,** 10618–10632. ISSN: 15306860 (2019).

179. Huang, D., Nakamura, Y., Ogata, A. & Kidoaki, S. Characterization of 3D matrix conditions for cancer cell migration with elasticity/porosity-independent tunable microfiber gels. *Polymer Journal* **52,** 333–344. ISSN: 0032-3896 (2020).

180. Greiner, A. M., Richter, B. & Bastmeyer, M. Micro-Engineered 3D Scaffolds for Cell Culture Studies. *Macromolecular Bioscience* **12,** 1301–1314. ISSN: 1616-5195 (2012).

181. Klein, F. *et al.* Elastic fully three-dimensional microstructure scaffolds for cell force measurements. *Advanced Materials* **22,** 868–871. ISSN: 09359648 (2010).

182. Greiner, A. M. *et al.* Cell type-specific adaptation of cellular and nuclear volume in micro-engineered 3D environments. *Biomaterials* **69,** 121–132. ISSN: 18785905 (2015).

183. Silbernagel, N. *et al.* Shaping the heart: Structural and functional maturation of iPSC-cardiomyocytes in 3D-micro-scaffolds. *Biomaterials* **227,** 119551. ISSN: 0142-9612 (2020).

184. Bertels, S. *et al.* Geometrically defined environments direct cell division rate and subcellular YAP localization in single mouse embryonic stem cells. *Scientific Reports* **11,** 1–12. ISSN: 2045-2322 (2021).

185. Hippler, M. *et al.* Mechanical stimulation of single cells by reversible host-guest interactions in 3D microscaffolds. *Science Advances* **6.** ISSN: 23752548 (2020).

186. Zinner, M, Lukonin, I & Liberali, P. Design principles of tissue organisation: How single cells coordinate across scales. *Curr Opin Cell Biol* **67,** 37–45. ISSN: 1879-0410 (2020).

187. Frantz, C, Stewart, K. M. & Weaver, V. M. The extracellular matrix at a glance. *J Cell Sci* **123,** 4195–4200. ISSN: 1477-9137 (2010).

188. Wen, Q & Janmey, P. A. Effects of non-linearity on cell-ECM interactions. *Exp Cell Res* **319,** 2481–2489. ISSN: 1090-2422 (2013).

189. Garcia, M. A., Nelson, W. J. & Chavez, N. Cell-Cell Junctions Organize Structural and Signaling Networks. *Cold Spring Harb Perspect Biol* **10.** ISSN: 1943-0264 (2018).

190. Bachmann, M, Kukkurainen, S, Hytonen, V. P. & Wehrle-Haller, B. Cell Adhesion by Integrins. *Physiol Rev* **99,** 1655–1699. ISSN: 1522-1210 (2019).

191. Charras, G & Yap, A. S. Tensile Forces and Mechanotransduction at Cell-Cell Junctions. *Curr Biol* **28,** R445–R457. ISSN: 1879-0445 (2018).

192. Parsons, J. T., Horwitz, A. R. & Schwartz, M. A. Cell adhesion: integrating cytoskeletal dynamics and cellular tension. *Nat Rev Mol Cell Biol* **11,** 633–643. ISSN: 1471-0080 (2010).

193. Chaudhuri, O, Cooper-White, J, Janmey, P. A., Mooney, D. J. & Shenoy, V. B. Effects of extracellular matrix viscoelasticity on cellular behaviour. *Nature* **584,** 535–546. ISSN: 1476-4687 (2020).

194. Bonakdar, N *et al.* Mechanical plasticity of cells. *Nat Mater* **15,** 1090–1094. ISSN: 1476-4660 (2016).

195. Hughes, A. J. *et al.* Engineered Tissue Folding by Mechanical Compaction of the Mesenchyme. *Dev Cell* **44,** 165–178 e6. ISSN: 1878-1551 (2018).

196. Tozluoglu, M *et al.* Planar Differential Growth Rates Initiate Precise Fold Positions in Complex Epithelia. *Dev Cell* **51,** 299–312 e4. ISSN: 1878-1551 (2019).

197. Shyer, A. E. *et al.* Villification: how the gut gets its villi. *Science* **342,** 212–218. ISSN: 1095-9203 (2013).

198. Nelson, C. M. On Buckling Morphogenesis. *J Biomech Eng* **138,** 21005. ISSN: 1528-8951 (2016).

199. Yevick, H. G., Miller, P. W., Dunkel, J & Martin, A. C. Structural Redundancy in Supracellular Actomyosin Networks Enables Robust Tissue Folding. *Dev Cell* **50,** 586–598 e3. ISSN: 1878-1551 (2019).

200. Shellard, A, Szabo, A, Trepat, X & Mayor, R. Supracellular contraction at the rear of neural crest cell groups drives collective chemotaxis. *Science* **362,** 339–343. ISSN: 1095-9203 (2018).

201. Roper, K. Supracellular actomyosin assemblies during development. *Bioarchitecture* **3,** 45–49. ISSN: 1949-100X (2013).

202. Lang, E *et al.* Mechanical coupling of supracellular stress amplification and tissue fluidization during exit from quiescence. *Proc Natl Acad Sci U S A* **119,** e2201328119. ISSN: 1091-6490 (2022).

203. Rogers, K. W. & Schier, A. F. Morphogen gradients: from generation to interpretation. *Annu Rev Cell Dev Biol* **27,** 377–407. ISSN: 1530-8995 (2011).

204. Lim, H. Y. G. *et al.* Keratins are asymmetrically inherited fate determinants in the mammalian embryo. *Nature* **585,** 404–409. ISSN: 1476-4687 (2020).

205. Chen, Q, Shi, J, Tao, Y & Zernicka-Goetz, M. Tracing the origin of heterogeneity and symmetry breaking in the early mammalian embryo. *Nat Commun* **9,** 1819. ISSN: 2041-1723 (2018).

206. Winer, J. P., Oake, S & Janmey, P. A. Non-linear elasticity of extracellular matrices enables contractile cells to communicate local position and orientation. *PLoS One* **4,** e6382. ISSN: 1932-6203 (2009).

207. Safdari, H *et al.* Noise-driven cell differentiation and the emergence of spatiotemporal patterns. *PLoS One* **15,** e0232060. ISSN: 1932-6203 (2020).

208. Huang, S. Non-genetic heterogeneity of cells in development: more than just noise. *Development* **136,** 3853–3862. ISSN: 1477-9129 (2009).

209. Schauer, A, Pinheiro, D, Hauschild, R & Heisenberg, C. P. Zebrafish embryonic explants undergo genetically encoded self-assembly. *Elife* **9.** ISSN: 2050-084X (2020).

210. Turner, D. A., Baillie-Johnson, P & Martinez Arias, A. Organoids and the genetically encoded self-assembly of embryonic stem cells. *Bioessays* **38,** 181–191. ISSN: 1521-1878 (2016).

211. Martinez-Ara, G *et al.* Optogenetic control of apical constriction induces synthetic morphogenesis in mammalian tissues. *Nat Commun* **13,** 5400. ISSN: 2041-1723 (2022).

212. Linde-Medina, M & Marcucio, R. Living tissues are more than cell clusters: The extracellular matrix as a driving force in morphogenesis. *Prog Biophys Mol Biol* **137,** 46–51. ISSN: 1873-1732 (2018).

213. Heller, E & Fuchs, E. Tissue patterning and cellular mechanics. *J Cell Biol* **211,** 219–231. ISSN: 1540-8140 (2015).

214. Shyer, A. E. *et al.* Emergent cellular self-organization and mechanosensation initiate follicle pattern in the avian skin. *Science* **357,** 811–815. ISSN: 1095-9203 (2017).

215. Palmquist, K. H. *et al.* Reciprocal cell-ECM dynamics generate supracellular fluidity underlying spontaneous follicle patterning. *Cell* **185,** 1960–1973 e11. ISSN: 1097-4172 (2022).

216. Cohen, R *et al.* Mechanical forces drive ordered patterning of hair cells in the mammalian inner ear. *Nat Commun* **11,** 5137. ISSN: 2041-1723 (2020).

217. Bonnans, C, Chou, J & Werb, Z. Remodelling the extracellular matrix in development and disease. *Nat Rev Mol Cell Biol* **15,** 786–801. ISSN: 1471-0080 (2014).

218. Poujade, M. *et al.* Collective migration of an epithelial monolayer in response to a model wound. *Proceedings of the National Academy of Sciences of the United States of America* **104,** 15988–15993. ISSN: 00278424 (2007).

219. Trepat, X. *et al.* Physical forces during collective cell migration. *Nature Physics* **5,** 426–430. ISSN: 1745-2481 (2009).

220. Tambe, D. T. *et al.* Monolayer Stress Microscopy: Limitations, Artifacts, and Accuracy of Recovered Intercellular Stresses. *PLOS ONE* **8,** e55172. ISSN: 1932-6203 (2013).

221. Tusan, C. G. *et al.* Collective Cell Behavior in Mechanosensing of Substrate Thickness. *Biophys J* **114,** 2743–2755. ISSN: 1542-0086 (2018).

222. Shellard, A & Mayor, R. Collective durotaxis along a self-generated stiffness gradient in vivo. *Nature* **600,** 690–694. ISSN: 1476-4687 (2021).

223. Clark, A. G. *et al.* Self-generated gradients steer collective migration on viscoelastic collagen networks. *Nat Mater* **21,** 1200–1210. ISSN: 1476-4660 (2022).

224. Van Helvert, S, Storm, C & Friedl, P. Mechanoreciprocity in cell migration. *Nat Cell Biol* **20,** 8–20. ISSN: 1476-4679 (2018).

225. Palamidessi, A *et al.* Unjamming overcomes kinetic and proliferation arrest in terminally differentiated cells and promotes collective motility of carcinoma. *Nat Mater* **18,** 1252–1263. ISSN: 1476-4660 (2019).

226. Marchant, C. L., Malmi-Kakkada, A. N., Espina, J. A. & Barriga, E. H. Cell clusters softening triggers collective cell migration in vivo. *Nat Mater* **21,** 1314–1323. ISSN: 1476-4660 (2022).

227. Ilina, O *et al.* Cell-cell adhesion and 3D matrix confinement determine jamming transitions in breast cancer invasion. *Nat Cell Biol* **22,** 1103–1115. ISSN: 1476-4679 (2020).

228. Paszek, M. J. *et al.* Tensional homeostasis and the malignant phenotype. *Cancer Cell* **8,** 241–254. ISSN: 1535-6108 (2005).

229. Chaudhuri, O *et al.* Extracellular matrix stiffness and composition jointly regulate the induction of malignant phenotypes in mammary epithelium. *Nat Mater* **13,** 970–978. ISSN: 1476-4660 (2014).

230. Fuhs, T. *et al.* Rigid tumours contain soft cancer cells. *Nature Physics* **18,** 1510–1519. ISSN: 1745-2481 (2022).

231. Wei, S. C. *et al.* Matrix stiffness drives epithelial-mesenchymal transition and tumour metastasis through a TWIST1-G3BP2 mechanotransduction pathway. *Nat Cell Biol* **17,** 678–688 (2015).

232. Tweedy, L *et al.* Seeing around corners: Cells solve mazes and respond at a distance using attractant breakdown. *Science* **369.** ISSN: 1095-9203 (2020).

233. Tweedy, L & Insall, R. H. Self-Generated Gradients Yield Exceptionally Robust Steering Cues. *Front Cell Dev Biol* **8,** 133. ISSN: 2296-634X (2020).

234. Todhunter, M. E. *et al.* Programmed synthesis of three-dimensional tissues. *Nat Methods* **12,** 975–981 (2015).

235. D'Arcangelo, E & McGuigan, A. P. Micropatterning strategies to engineer controlled cell and tissue architecture in vitro. *Biotechniques* **58,** 13–23 (2015).

236. Raghavan, S, Desai, R. A., Kwon, Y, Mrksich, M & Chen, C. S. Micropatterned dynamically adhesive substrates for cell migration. *Langmuir* **26,** 17733–17738 (2010).

237. Vishwakarma, M *et al.* Mechanical interactions among followers determine the emergence of leaders in migrating epithelial cell collectives. *Nat Commun* **9,** 3469 (2018).

238. Vazquez, K, Saraswathibhatla, A & Notbohm, J. Effect of substrate stiffness on friction in collective cell migration. *Sci Rep* **12,** 2474 (2022).

239. Anon, E *et al.* Cell crawling mediates collective cell migration to close undamaged epithelial gaps. *Proc Natl Acad Sci U S A* **109,** 10891–10896 (2012).

240. Vedula, S. R. *et al.* Emerging modes of collective cell migration induced by geometrical constraints. *Proc Natl Acad Sci U S A* **109,** 12974–12979 (2012).

241. Marel, A. K. *et al.* Flow and diffusion in channel-guided cell migration. *Biophys J* **107,** 1054–1064 (2014).

242. Peyret, G *et al.* Sustained Oscillations of Epithelial Cell Sheets. *Biophys J* **117,** 464–478 (2019).

243. Segerer, F. J., Thüroff, F., Piera Alberola, A., Frey, E. & Rädler, J. O. Emergence and Persistence of Collective Cell Migration on Small Circular Micropatterns. *Physical Review Letters* **114,** 228102. ISSN: 10797114. eprint: 1505.04643 (2015).

244. Costa, P., Blowes, L. M., Laly, A. C. & Connelly, J. T. Regulation of collective cell polarity and migration using dynamically adhesive micropatterned substrates. *Acta Biomater* **126,** 291–300. ISSN: 18787568 (2021).

245. Rausch, S. *et al.* Polarizing cytoskeletal tension to induce leader cell formation during collective cell migration. *Biointerphases* **8,** 32. ISSN: 1934-8630 (2013).

246. Gomez, E. W., Chen, Q. K., Gjorevski, N & Nelson, C. M. Tissue geometry patterns epithelial-mesenchymal transition via intercellular mechanotransduction. *J Cell Biochem* **110,** 44–51 (2010).

247. Saw, T. B. *et al.* Topological defects in epithelia govern cell death and extrusion. *Nature* **544,** 212–216. ISSN: 1476-4687 (2017).

248. Deforet, M, Hakim, V, Yevick, H. G., Duclos, G & Silberzan, P. Emergence of collective modes and tri-dimensional structures from epithelial confinement. *Nat Commun* **5,** 3747 (2014).

249. Latorre, E *et al.* Active superelasticity in three-dimensional epithelia of controlled shape. *Nature* **563,** 203–208. ISSN: 1476-4687 (2018).

250. Jain, I *et al.* Delineating cooperative effects of Notch and biomechanical signals on patterned liver differentiation. *Commun Biol* **5,** 1073 (2022).

251. Kaylan, K. B. *et al.* Spatial patterning of liver progenitor cell differentiation mediated by cellular contractility and Notch signaling. *Elife* **7** (2018).

252. Muncie, J. M. *et al.* Mechanical Tension Promotes Formation of Gastrulation-like Nodes and Patterns Mesoderm Specification in Human Embryonic Stem Cells. *Dev Cell* **55,** 679–694 e11 (2020).

253. Blonski, S *et al.* Direction of epithelial folding defines impact of mechanical forces on epithelial state. *Dev Cell* **56,** 3222–3234 e6 (2021).

254. Matejcic, M & Trepat, X. Buckling Up from the Bottom. *Dev Cell* **54,** 569–571. ISSN: 1878-1551 (2020).

255. Shigeta, K *et al.* Collective motion of epithelial cells along a wrinkled 3D-buckled hydrogel. *RSC Adv* **12,** 20174–20181 (2022).

256. Fabry, B *et al.* Scaling the microrheology of living cells. *Phys Rev Lett* **87,** 148102. ISSN: 0031-9007 (2001).

257. Lenormand, G, Millet, E, Fabry, B, Butler, J. P. & Fredberg, J. J. Linearity and time-scale invariance of the creep function in living cells. *J R Soc Interface* **1,** 91–97. ISSN: 1742-5689 (2004).

258. Desprat, N, Richert, A, Simeon, J & Asnacios, A. Creep function of a single living cell. *Biophys J* **88,** 2224–2233. ISSN: 0006-3495 (2005).

259. Weng, S, Shao, Y, Chen, W & Fu, J. Mechanosensitive subcellular rheostasis drives emergent single-cell mechanical homeostasis. *Nat Mater* **15,** 961–967. ISSN: 1476-4660 (2016).

260. Webster, K. D., Ng, W. P. & Fletcher, D. A. Tensional homeostasis in single fibroblasts. *Biophys J* **107,** 146–155. ISSN: 1542-0086 (2014).

261. Harris, A. R. *et al.* Characterizing the mechanics of cultured cell monolayers. *Proceedings of the National Academy of Sciences of the United States of America* **109,** 16449–16454. ISSN: 00278424 (2012).

262. Duque, J. *et al.* Fracture in Living Cell Monolayers. *bioRxiv,* 2023.01.05.522736 (2023).

263. Stopak, D & Harris, A. K. Connective tissue morphogenesis by fibroblast traction. I. Tissue culture observations. *Dev Biol* **90,** 383–398. ISSN: 0012-1606 (1982).

264. Bischofs, I. B., Klein, F., Lehnert, D., Bastmeyer, M. & Schwarz, U. S. Filamentous network mechanics and active contractility determine cell and tissue shape. *Biophysical Journal* **95,** 3488–3496. ISSN: 15420086 (2008).

265. Nelson, C. M., VanDuijn, M. M., Inman, J. L., Fletcher, D. A. & Bissell, M. J. Tissue geometry determines sites of mammary branching morphogenesis in organotypic cultures. *Science* **314,** 298–300. ISSN: 00368075 (2006).

266. Gjorevski, N & Nelson, C. M. Mapping of mechanical strains and stresses around quiescent engineered three-dimensional epithelial tissues. *Biophys J* **103,** 152–162 (2012).

267. Gjorevski, N, Piotrowski, A. S., Varner, V. D. & Nelson, C. M. Dynamic tensile forces drive collective cell migration through three-dimensional extracellular matrices. *Sci Rep* **5,** 11458 (2015).

268. Bidan, C. M. *et al.* Gradual conversion of cellular stress patterns into pre-stressed matrix architecture during in vitro tissue growth. *J R Soc Interface* **13** (2016).

269. Ilina, O, Bakker, G. J., Vasaturo, A, Hofmann, R. M. & Friedl, P. Two-photon laser-generated microtracks in 3D collagen lattices: principles of MMP-dependent and -independent collective cancer cell invasion. *Phys Biol* **8,** 15010 (2011).

270. Nikolaev, M *et al.* Homeostatic mini-intestines through scaffold-guided organoid morphogenesis. *Nature* **585,** 574–578 (2020).

271. Kollmannsberger, P, Bidan, C. M., Dunlop, J. W. C., Fratzl, P & Vogel, V. Tensile forces drive a reversible fibroblast-to-myofibroblast transition during tissue growth in engineered clefts. *Sci Adv* **4** (2018).

272. Xi, W., Sonam, S., Beng Saw, T., Ladoux, B. & Teck Lim, C. Emergent patterns of collective cell migration under tubular confinement. *Nature Communications* **8,** 1–15. ISSN: 2041-1723 (2017).

273. Mazalan, M. B., Ramlan, M. A. B., Shin, J. H. & Ohashi, T. Effect of Geometric Curvature on Collective Cell Migration in Tortuous Microchannel Devices. *Micromachines (Basel)* **11** (2020).

274. Zeng, M., Jin, S. & Ye, K. Tissue and Organ 3D Bioprinting. *SLAS Technology* **23,** 301–314 (2018).

275. Panda, S. *et al.* A focused review on three-dimensional bioprinting technology for artificial organ fabrication. *Biomaterials Science* **10,** 5054–5080. ISSN: 2047-4849 (2022).

276. Trushko, A *et al.* Buckling of an Epithelium Growing under Spherical Confinement. *Dev Cell* **54,** 655–668 e6. ISSN: 1878-1551 (2020).

277. Alessandri, K *et al.* A 3D printed microfluidic device for production of functionalized hydrogel microcapsules for culture and differentiation of human Neuronal Stem Cells (hNSC). *Lab Chip* **16,** 1593–1604. ISSN: 1473-0189 (2016).

278. Lemma, E. D., Spagnolo, B, De Vittorio, M & Pisanello, F. Studying Cell Mechanobiology in 3D: The Two-Photon Lithography Approach. *Trends Biotechnol* **37,** 358–372 (2019).

279. Fendler, C *et al.* Microscaffolds by Direct Laser Writing for Neurite Guidance Leading to Tailor-Made Neuronal Networks. *Adv Biosyst* **3,** e1800329 (2019).

280. Agrawal, L, Saidani, M, Guillaud, L & Terenzio, M. Development of 3D culture scaffolds for directional neuronal growth using 2-photon lithography. *Mater Sci Eng C Mater Biol Appl* **131,** 112502 (2021).

281. Sharaf, A *et al.* Two-Photon Polymerization of 2.5D and 3D Microstructures Fostering a Ramified Resting Phenotype in Primary Microglia. *Front Bioeng Biotechnol* **10,** 926642 (2022).

282. Barin, N *et al.* 3D-Engineered Scaffolds to Study Microtubes and Localization of Epidermal Growth Factor Receptor in Patient-Derived Glioma Cells. *Small* **18,** e2204485 (2022).

283. Greiner, A. M. *et al.* Multifunctional polymer scaffolds with adjustable pore size and chemoattractant gradients for studying cell matrix invasion. *Biomaterials* **35,** 611–619 (2014).

284. Hahn, V. *et al.* Two-step absorption instead of two-photon absorption in 3D nanoprinting. *Nature Photonics* **15,** 932–938 (2021).

285. Hahn, V. *et al.* Light-sheet 3D microprinting via two-colour two-step absorption. *Nature Photonics* **16,** 784–791 (2022).

286. Drost, J. & Clevers, H. Organoids in cancer research. *Nature Reviews Cancer* **18,** 407–418. ISSN: 1474-1768 (2018).

287. Clevers, H. The intestinal crypt, a prototype stem cell compartment. *Cell* **154,** 274. ISSN: 1097-4172 (2013).

288. Serra, D *et al.* Self-organization and symmetry breaking in intestinal organoid development. *Nature* **569,** 66–72. ISSN: 1476-4687 (2019).

289. Yang, Q *et al.* Cell fate coordinates mechano-osmotic forces in intestinal crypt formation. *Nat Cell Biol* **23,** 733–744 (2021).

290. Perez-Gonzalez, C *et al.* Mechanical compartmentalization of the intestinal organoid enables crypt folding and collective cell migration. *Nat Cell Biol* **23,** 745–757 (2021).

291. Phuong Le, A, Kim, J & Koehler, K. R. The mechanical forces that shape our senses. *Development* **149** (2022).

292. Campisi, M *et al.* 3D self-organized microvascular model of the human blood-brain barrier with endothelial cells, pericytes and astrocytes. *Biomaterials* **180,** 117–129 (2018).

293. Skylar-Scott, M. A. *et al.* Biomanufacturing of organ-specific tissues with high cellular density and embedded vascular channels. *Sci Adv* **5,** eaaw2459 (2019).

294. Homan, K. A. *et al.* Flow-enhanced vascularization and maturation of kidney organoids in vitro. *Nat Methods* **16,** 255–262 (2019).

295. Ching, T *et al.* Biomimetic Vasculatures by 3D-Printed Porous Molds. *Small* **18,** e2203426 (2022).

296. Blatchley, M. R. & Anseth, K. S. Middle-out methods for spatiotemporal tissue engineering of organoids. *Nature Reviews Bioengineering,* 1–17. ISSN: 2731-6092 (2023).

297. Hollingsworth, S. A. & Dror, R. O. Molecular Dynamics Simulation for All. *Neuron* **99,** 1129–1143. ISSN: 0896-6273 (2018).

298. Albert, P. J. & Schwarz, U. S. Modeling cell shape and dynamics on micropatterns. *Cell Adhesion & Migration* **10,** 516–528. ISSN: 19336926 (2016).

299. Schwarz, U. S. & Safran, S. A. Physics of adherent cells. *Reviews of Modern Physics* **85,** 1327–1381. ISSN: 00346861. eprint: 1309.2817 (2013).

300. Kollmannsberger, P., Bidan, C. M., Dunlop, J. W. & Fratzl, P. The physics of tissue patterning and extracellular matrix organisation: how cells join forces. *Soft Matter* **7,** 9549–9560. ISSN: 1744-6848 (2011).

301. Bischofs, I. B., Schmidt, S. S. & Schwarz, U. S. Effect of Adhesion Geometry and Rigidity on Cellular Force Distributions. *Physical Review Letters* **103,** 048101. ISSN: 00319007. eprint: 0907.4114 (2009).

302. Schakenraad, K. *et al.* Mechanical interplay between cell shape and actin cytoskeleton organization. *Soft Matter* **16,** 6328–6343. ISSN: 1744-6848. eprint: 1905.09805 (2020).

303. Guthardt Torres, P., Bischofs, I. B. & Schwarz, U. S. Contractile network models for adherent cells. *Physical Review E - Statistical, Nonlinear, and Soft Matter Physics* **85,** 011913. ISSN: 15393755. eprint: 1201.2786 (2012).

304. Edwards, C. M. & Schwarz, U. S. Force localization in contracting cell layers. *Physical Review Letters* **107,** 128101. ISSN: 00319007. eprint: 1201.2779 (2011).

305. Oakes, P. W., Banerjee, S., Marchetti, M. C. & Gardel, M. L. Geometry Regulates Traction Stresses in Adherent Cells. *Biophysical Journal* **107,** 825–833. ISSN: 0006-3495 (2014).

306. Prost, J., Jülicher, F. & Joanny, J. F. Active gel physics. *Nature Physics* **11,** 111–117. ISSN: 1745-2481 (2015).

307. Bikwemu, R. *et al.* Controlling cell-matrix traction forces by extracellular geometry. *New Journal of Physics* **15,** 35015 (2013).

308. Ziebert, F., Swaminathan, S. & Aranson, I. S. Model for self-polarization and motility of keratocyte fragments. *Journal of the Royal Society Interface* **9,** 1084–1092. ISSN: 17425662 (2012).

309. Karma, A., Kessler, D. A. & Levine, H. Phase-Field Model of Mode III Dynamic Fracture. *Physical Review Letters* **87,** 045501. ISSN: 10797114. eprint: 0105034 (cond-mat) (2001).

310. Moure, A. & Gomez, H. Phase-Field Modeling of Individual and Collective Cell Migration. *Archives of Computational Methods in Engineering* **28,** 311–344. ISSN: 18861784 (2021).

311. Merks, R. M. H. & Glazier, J. A. Dynamic mechanisms of blood vessel growth Related content (2006).

312. Marée, A. F. M., Jilkine, A., Dawes, A., Grieneisen, V. A. & Edelstein-Keshet, L. *Polarization and movement of keratocytes: A multiscale modelling approach* **5,** 1169–1211. ISBN: 1153800691 (2006).

313. Vianay, B. *et al.* Single Cells Spreading on a Protein Lattice Adopt an Energy Minimizing Shape (2009).

314. Marée, A. F. M., Grieneisen, V. A. & Hogeweg, P. *Single cell based models in biology and medicine* (eds Anderson, A. R. A., Chaplain, M. A. J. & Rejniak, K. A.) 107–136. ISBN: 978-3-7643-8101-1 (Birkhäuser, Basel, 2007).

315. Ananthakrishnan, R. *et al.* Quantifying the contribution of actin networks to the elastic strength of fibroblasts. *Journal of Theoretical Biology* **242,** 502–516. ISSN: 0022-5193 (2006).

316. Herant, M. & Dembo, M. Cytopede: A Three-Dimensional Tool for Modeling Cell Motility on a Flat Surface. *Journal of Computational Biology* **17,** 1639. ISSN: 10665277 (2010).

317. Herant, M. & Dembo, M. Form and Function in Cell Motility: From Fibroblasts to Keratocytes. *Biophysical Journal* **98,** 1408. ISSN: 15420086 (2010).

318. Gladilin, E. *et al.* 3D finite element analysis of uniaxial cell stretching: from image to insight. *Physical Biology* **4,** 104. ISSN: 1478-3975 (2007).

319. Hervas-Raluy, S., Gomez-Benito, M. J., Borau-Zamora, C., Cóndor, M. & Garcia-Aznar, J. M. A new 3D finite element-based approach for computing cell surface tractions assuming nonlinear conditions. *PLOS ONE* **16,** e0249018. ISSN: 1932-6203 (2021).

320. Ditlev, J. A., Vacanti, N. M., Novak, I. L. & Loew, L. M. An open model of actin dendritic nucleation. *Biophysical Journal* **96,** 3529–3542. ISSN: 15420086 (2009).

321. Nedelec, F. & Foethke, D. Collective Langevin dynamics of flexible cytoskeletal fibers. *New Journal of Physics* **9,** 427. ISSN: 1367-2630. eprint: 0903.5178 (2007).

322. Allena, R. Cell Migration with Multiple Pseudopodia: Temporal and Spatial Sensing Models. *Bull Math Biol* **75,** 288–316 (2013).

323. Fan, H. & Li, S. Modeling universal dynamics of cell spreading on elastic substrates. *Biomechanics and Modeling in Mechanobiology* **14,** 1265–1280. ISSN: 16177940 (2015).

324. Winkler, B., Aranson, I. S. & Ziebert, F. Confinement and substrate topography control cell migration in a 3D computational model. *Communications Physics* **2,** 1–11. ISSN: 2399-3650 (2019).

325. Fortuna, I. *et al.* CompuCell3D Simulations Reproduce Mesenchymal Cell Migration on Flat Substrates. *Biophysical Journal* **118,** 2801–2815. ISSN: 0006-3495 (2020).

326. Holmes, W. R. & Edelstein-Keshet, L. A Comparison of Computational Models for Eukaryotic Cell Shape and Motility. *PLoS Computational Biology* **8** (ed Glazier, J. A.) e1002793. ISSN: 1553-7358 (2012).

327. Ladoux, B. & Mège, R. M. Mechanobiology of collective cell behaviours. *Nature Reviews Molecular Cell Biology* **18,** 743–757. ISSN: 1471-0080 (2017).

328. Foty, R. A. & Steinberg, M. S. Cadherin-mediated cell-cell adhesion and tissue segregation in relation to malignancy. *International Journal of Developmental Biology* **48,** 397–409. ISSN: 0214-6282 (2004).

329. Graner, F. & Glazier, J. A. Simulation of the differential adhesion driven rearrangement of biological cells. *Physical Review E - Statistical, Nonlinear, and Soft Matter Physics* **47** (1992).

330. Merks, R. M., Brodsky, S. V., Goligorksy, M. S., Newman, S. A. & Glazier, J. A. Cell elongation is key to in silico replication of in vitro vasculogenesis and subsequent remodeling. *Developmental Biology* **289,** 44–54 (2006).

331. Thüroff, F., Goychuk, A., Reiter, M. & Frey, E. Bridging the gap between single-cell migration and collective dynamics. *bioRxiv,* 548677 (2019).

332. Shirinifard, A. *et al.* 3D Multi-Cell Simulation of Tumor Growth and Angiogenesis. *PLoS ONE* **4** (ed Hotchin, N. A.) e7190 (2009).

333. Löber, J., Ziebert, F. & Aranson, I. S. Collisions of deformable cells lead to collective migration. *Scientific Reports 2015 5:1* **5,** 1–7. ISSN: 2045-2322 (2015).

334. Farhadifar, R., Röper, J. C., Aigouy, B., Eaton, S. & Jülicher, F. The Influence of Cell Mechanics, Cell-Cell Interactions, and Proliferation on Epithelial Packing. *Current Biology* **17,** 2095–2104. ISSN: 0960-9822 (2007).

335. Alt, S., Ganguly, P. & Salbreux, G. Vertex models: from cell mechanics to tissue morphogenesis. eng. *Philosophical transactions of the Royal Society of London. Series B, Biological sciences* **372.** ISSN: 1471-2970 (2017).

336. Osterfield, M., Du, X. X., Schüpbach, T., Wieschaus, E. & Shvartsman, S. Y. Three-Dimensional Epithelial Morphogenesis in the Developing Drosophila Egg. *Developmental Cell* **24,** 400–410. ISSN: 15345807 (2013).

337. Czajkowski, M., Bi, D., Manning, M. L. & Marchetti, M. C. Hydrodynamics of shape-driven rigidity transitions in motile tissues. *Soft Matter* **14,** 5628–5642. ISSN: 1744-6848. eprint: 1710.09405 (2018).

338. Nonomura, M. Study on Multicellular Systems Using a Phase Field Model. *PLOS ONE* **7,** e33501. ISSN: 1932-6203. eprint: 1109.5246 (2012).

339. Chojowski, R., Schwarz, U. S. & Ziebert, F. Reversible elastic phase field approach and application to cell monolayers. *The European Physical Journal E* **43,** 1–12. ISSN: 1292-895X (2020).

340. Montes-Olivas, S., Marucci, L. & Homer, M. Mathematical Models of Organoid Cultures. *Frontiers in Genetics* **10,** 873. ISSN: 16648021 (2019).

341. Okuda, S., Inoue, Y., Watanabe, T. & Adachi, T. Coupling intercellular molecular signalling with multicellular deformation for simulating three-dimensional tissue morphogenesis. *Interface Focus* **5.** ISSN: 20428901 (2015).

342. Okuda, S. *et al.* Strain-triggered mechanical feedback in self-organizing optic-cup morphogenesis. *Science Advances* **4.** ISSN: 23752548 (2018).

343. Okuda, S., Miura, T., Inoue, Y., Adachi, T. & Eiraku, M. Combining Turing and 3D vertex models reproduces autonomous multicellular morphogenesis with undulation, tubulation, and branching OPEN. *Scientific Reports* **8,** 2386 (2018).

344. Cerruti, B. *et al.* Polarity, cell division, and out-of-equilibrium dynamics control the growth of epithelial structures. *Journal of Cell Biology* **203,** 359–372. ISSN: 1540-8140 (2013).

345. Pin, C. *et al.* An individual based computational model of intestinal crypt fission and its application to predicting unrestrictive growth of the intestinal epithelium. *Integrative Biology* **7,** 213–228. ISSN: 1757-9708 (2015).

346. Yan, H., Konstorum, A. & Lowengrub, J. S. Three-Dimensional Spatiotemporal Modeling of Colon Cancer Organoids Reveals that Multimodal Control of Stem Cell Self-Renewal is a Critical Determinant of Size and Shape in Early Stages of Tumor Growth. *Bulletin of Mathematical Biology* **80,** 1404–1433. ISSN: 15229602 (2018).

347. Buske, P. *et al.* On the biomechanics of stem cell niche formation in the gut - Modelling growing organoids. *FEBS Journal* **279,** 3475–3487. ISSN: 1742464X (2012).

348. Thalheim, T. *et al.* Linking stem cell function and growth pattern of intestinal organoids. *Developmental Biology* **433,** 254–261. ISSN: 1095564X (2018).

349. Berger, E. *et al.* Millifluidic culture improves human midbrain organoid vitality and differentiation. *Lab on a Chip* **18,** 3172 (2018).

350. Voss-Böhme, A. Multi-Scale Modeling in Morphogenesis: A Critical Analysis of the Cellular Potts Model. *PLoS ONE* **7,** 42852 (2012).

351. Scianna, M. & Preziosi, L. Modelling the Influence of Nucleus Elasticity on Cell Invasion in Fiber Networks and Microchannels. *Journal of theoretical biology* (2013).

352. Marée, A. F. M., Grieneisen, V. A. & Edelstein-Keshet, L. How Cells Integrate Complex Stimuli: The Effect of Feedback from Phosphoinositides and Cell Shape on Cell Polarization and Motility. *PLoS Computational Biology* **8** (ed McCulloch, A. D.) e1002402. ISSN: 1553-7358 (2012).

353. Magno, R., Grieneisen, V. A. & Marée, A. F. M. The biophysical nature of cells: potential cell behaviours revealed by analytical and computational studies of cell surface mechanics. *BMC Biophysics* **8,** 8 (2015).

354. Link, R. & Schwarz, U. S. Simulating 3D Cell Shape with the Cellular Potts Model. *Methods in molecular biology (Clifton, N.J.)* **2600,** 323–339. ISSN: 1940-6029 (2023).

355. Swat, M. H. *et al.* Multi-Scale Modeling of Tissues Using CompuCell3D. *Methods in Cell Biology* **110,** 325–366. ISSN: 0091-679X (2012).

356. Starruß, J., De Back, W., Brusch, L. & Deutsch, A. Morpheus: A user-friendly modeling environment for multiscale and multicellular systems biology. *Bioinformatics* **30,** 1331–1332. ISSN: 14602059 (2014).

357. Wortel, I. M. & Textor, J. Artistoo, a library to build, share, and explore simulations of cells and tissues in the web browser. *eLife* **10.** ISSN: 2050084X (2021).

358. Swat, M., Cickovski, T., Glazier, J., Dementosv, A. & Zaitlen, B. *Developers' Documentation for CompuCell3D Version 3.4.1* 2009.

359. Ouchi, N. B., Glazier, J. A., Rieu, J. P., Upadhyaya, A. & Sawada, Y. Improving the realism of the cellular Potts model in simulations of biological cells. *Physica A: Statistical Mechanics and its Applications* **329,** 451–458. ISSN: 03784371 (2003).

360. Versaevel, M., Grevesse, T. & Gabriele, S. Spatial coordination between cell and nuclear shape within micropatterned endothelial cells. *Nature Communications* **3,** 1–11. ISSN: 2041-1723 (2012).

361. Huang, S., Brangwynne, C. P., Parker, K. K. & Ingber, D. E. Symmetry-breaking in mammalian cell cohort migration during tissue pattern formation: Role of random-walk persistence. *Cell Motility and the Cytoskeleton* **61,** 201–213. ISSN: 08861544 (2005).

362. Albert, P. J. & Schwarz, U. S. Dynamics of Cell Ensembles on Adhesive Micropatterns: Bridging the Gap between Single Cell Spreading and Collective Cell Migration. *PLOS Computational Biology* **12** (ed Mac Gabhann, F.) e1004863. ISSN: 1553-7358 (2016).

363. Link, R., Jaggy, M., Bastmeyer, M. & Schwarz, U. S. Modelling Cell Shape in 3D Structured Environments: A Quantitative Comparison with Experiments. *bioRxiv,* 2023.08.07.552225 (2023).

364. Wiesner, D., Nečasová, T. & Svoboda, D. On generative modeling of cell shape using 3D GANs. *Lecture Notes in Computer Science* **11752 LNCS,** 672–682. ISSN: 16113349 (2019).

365. Johnson, G. R., Buck, T. E., Sullivan, D. P., Rohde, G. K. & Murphy, R. F. Joint modeling of cell and nuclear shape variation. *Molecular Biology of the Cell* **26,** 4046–4056. ISSN: 19394586 (2015).

366. Wegener, M. & Fischer, J. Three-dimensional direct laser writing inspired by stimulated-emission-depletion microscopy [Invited]. *Optical Materials Express* **1,** 614–624. ISSN: 2159-3930 (2011).

367. Khairy, K., Foo, J. & Howard, J. Shapes of Red Blood Cells: Comparison of 3D Confocal Images with the Bilayer-Couple Model. *Cellular and Molecular Bioengineering* **1,** 173–181. ISSN: 1865-5033 (2008).

368. Ducroz, C., Olivo-Marin, J. C. & Dufour, A. Characterization of cell shape and deformation in 3D using Spherical Harmonics. *Proceedings - International Symposium on Biomedical Imaging,* 848–851. ISSN: 19457928 (2012).

369. Dufour, A. *et al.* Signal processing challenges in quantitative 3-D cell morphology: More than meets the eye. *IEEE Signal Processing Magazine* **32,** 30–40. ISSN: 10535888 (2015).

370. Medyukhina, A. *et al.* Dynamic spherical harmonics approach for shape classification of migrating cells. *Scientific Reports 2020 10:1* **10,** 1–12. ISSN: 2045-2322 (2020).

371. Van Bavel, C., Thiels, W. & Jelier, R. Cell shape characterization, alignment and comparison using FlowShape. *bioRxiv,* 2022.12.08.519700 (2022).

372. Driscoll, J. R. & Healy, D. M. Computing fourier transforms and convolutions on the 2-sphere. *Advances in Applied Mathematics* **15,** 202–250. ISSN: 10902074 (1994).

373. Wieczorek, M. A. & Meschede, M. SHTools: Tools for Working with Spherical Harmonics. *Geochemistry, Geophysics, Geosystems* **19,** 2574–2592. ISSN: 1525-2027 (2018).

374. Müller, A., Meyer, J., Paumer, T. & Pompe, T. Cytoskeletal transition in patterned cells correlates with interfacial energy model. *Soft Matter* **10,** 2444–2452 (2014).

375. Kenmotsu, K. *Surfaces with constant mean curvature* **221** (American Mathematical Soc., 2003).

376. Brakke, K. A. The Surface Evolver. *Experimental Mathematics* **1,** 141–165 (1992).

377. *Single cell based models in biology and medicine* eng (ed Anderson, A. R. A.) IX, 349 S. ISBN: 978-3-7643-8101-1 and 3-7643-8101-9 (Birkhäuser, Basel ; Berlin [u.a.], 2007).

378. Casey, M. A., Lusk, S. & Kwan, K. M. Build me up optic cup: Intrinsic and extrinsic mechanisms of vertebrate eye morphogenesis. *Developmental Biology* **476,** 128–136. ISSN: 1095564X (2021).

379. Beccari, L., Marco-Ferreres, R. & Bovolenta, P. The logic of gene regulatory networks in early vertebrate forebrain patterning. *Mechanisms of Development* **130,** 95–111. ISSN: 09254773 (2013).

380. Eiraku, M. *et al.* Self-organizing optic-cup morphogenesis in three-dimensional culture. *Nature* **472,** 51–58. ISSN: 00280836 (2011).

381. Kleinman, H. K. & Martin, G. R. Matrigel: Basement membrane matrix with biological activity. *Seminars in Cancer Biology* **15,** 378–386. ISSN: 1044-579X (2005).

382. Zilova, L. *et al.* Fish primary embryonic pluripotent cells assemble into retinal tissue mirroring in vivo early eye development. *eLife* **10.** ISSN: 2050084X (2021).

383. Ivanovitch, K., Cavodeassi, F. & Wilson, S. W. Precocious Acquisition of Neuroepithelial Character in the Eye Field Underlies the Onset of Eye Morphogenesis. *Developmental Cell* **27,** 293–305. ISSN: 15345807 (2013).

384. Steinberg, M. S. Differential adhesion in morphogenesis: a modern view. *Current Opinion in Genetics & Development* **17,** 281–286. ISSN: 0959-437X (2007).

Danksagung

Meine Doktorarbeit wäre ohne die Unterstützung und Hilfe zahlreicher Personen und Institutionen nicht möglich gewesen wäre. An dieser Stelle möchte ich meine aufrichtige Dankbarkeit zum Ausdruck bringen und all jenen meine Anerkennung aussprechen, die mich auf meinem Weg begleitet und unterstützt haben.

Ein besonderer Dank gebührt meinem Doktorvater Ulrich Schwarz, der mich mit fachlicher Kompetenz durch dieses anspruchsvolle Projekt geführt hat. Ohne seine wegweisenden Beiträge und Anregungen wäre dieses Projekt so nicht möglich gewesen. Darüber hinaus ermöglichte er mir meine Forschungsarbeit auf Tagungen zu präsentieren und dadurch wertvolle Erfahrungen in der wissenschaftliche Kommunikation zu sammeln.

Meinen Dank möchte ich auch meinem Zweitgutachter Fred Hamprecht aussprechen, der sich bereit erklärt hat, meine Arbeit zu prüfen. Ebenso dankbar bin ich den weiteren Mitgliedern meiner Promotionskommission, Peer Fischer und Rüdiger Klingeler.

Die Forschungsarbeit wäre ohne die Unterstützung des Exzellenzclusters 3DMM2O, des Insituts für theoretische Physik und des Bioquants nicht möglich gewesen. Isbesondere möchte ich mich bei meinen Kollaborationspartnern Kai Weissenbruch, Mona Jaggy und Martin Bastmeyer, Venera Weinhardt und Lucie Zilova für wertvollen Ideen und Inputs bedanken. Eure Mitwirkung und Unterstützung haben meine Forschungsarbeit bereichert und zu ihrem Erfolg maßgeblich beigetragen.

Außerdem möchte ich mich bei allen Mitgliedern der AG Schwarz bedanken, mit denen ich Ideen austauschen konnte, Diskussionen führen durfte und wertvolle fachliche Anregungen erhalten habe.

Mein aufrichtiger Dank geht auch an Falko Ziebert, Benedikt Löw, Julia Jäger und Leticia Täubert für das Korrekturelesen meiner Arbeit und viele hilfreiche Verbesserungsvorschläge.

Ein ganz besonderer Dank geht an meine Familie, die mir das Studium ermöglicht und mich immer unterstützt hat, sowie an meine Freunde für vielen schöne Bouldersessions und Spieleabende.